

DISSERTATIONES ASTRONOMIAE UNIVERSITATIS TARTUENSIS

12

**MODELING THE REFLECTION EFFECT
IN PRECATAclysmic BINARY SYSTEMS**

VLADISLAV-VENIAMIN PUSTYNSKI



TARTU UNIVERSITY
PRESS

The study was carried at the Institute of Theoretical Physics, University of Tartu, Estonia.

The dissertation was admitted on June 1, 2007, in partial fulfilment of the requirements for the degree of Doctor of Philosophy in physics (astrophysics), and was allowed for defence by the Council of the Department of Physics, the University of Tartu.

Supervisor: Dr. Izold Pustyl'nik, Tartu Observatory, Estonia

Opponents: Prof. Anatoli Cherepashchuk, GAISH, Moscow, Russia
Dr. Laurits Leedjärv, Tartu Observatory, Estonia

Defence: September 12, 2007, at the University of Tartu, Estonia

ISSN 1406–0647
ISBN 978–9949–11–676–8 (trükis)
ISBN 978–9949–11–677–5 (PDF)

Autoriõigus Vladislav-Veniamin Pustynski, 2007

Tartu Ülikooli Kirjastus
www.tyk.ee
Tellimus nr. 239

TABLE OF CONTENTS

1	Introduction	8
1.1	The objectives and the structure of the Thesis	8
1.2	Cataclysmic and precataclysmic binary systems: overview	9
1.2.1	Cataclysmic binary systems	9
1.2.2	Precataclysmic binaries	16
1.2.3	Extreme Horizontal Branch objects	20
1.3	The reflection effect	20
1.3.1	On modeling of the reflection effect	21
1.4	Conventional treatment of the reflection effect in PCBs	21
1.5	Advanced method of the reflection effect treatment	23
1.5.1	Problem formulation	23
1.5.2	Brief description of the model	23
2	Upper atmosphere model	25
2.1	Dilution coefficient	25
2.2	Net acceleration in binary system	26
2.3	Equilibrium conditions in the atmosphere of the secondary	27
2.4	Ionization conditions in the upper atmosphere	30
2.5	Reprocessed radiation intensity and spectrum	31
2.6	Technical details	32
2.7	Model analysis and results	33
2.7.1	Estimation of the role of collisional transitions and radiative ionizations from the second level	33
2.7.2	Conditions in ionized medium	35
3	Model for the inner layer	41
3.1	Incident flux	41
3.2	Eddington approximation	41
3.3	Emergent radiation intensity and spectrum	43
3.4	Technical details	44
4	The luminosity of the system	45
4.1	Secondary star luminosity	45
4.2	Transitions and occultations	46
4.2.1	Eclipses of the secondary star	46
4.2.2	Eclipses of the primary star	47
4.3	Light curve construction and normalization	48
4.4	Example spectra of a PCB	49
4.5	Technical details	50

5	Algorithm description	51
6	Applying of the model to observed PCB light curves	53
6.1	UU Sge	53
6.2	V477 Lyr	54
6.3	V664 Cas	56
7	Evolution of progenitors of Extreme Giant Branch objects	59
7.1	Analysis of mass loss, mass transfer and angular momentum loss	59
7.2	Mass transfer stability conditions	63
7.3	Numerical solution of the main equations	65
7.4	Results of numerical modeling	66
8	Achieved objectives and conclusions	70
8.1	Achieved objectives	70
8.2	Conclusions	70
A	Absorption coefficients	72
A.1	Cross-sections of hydrogen-like atoms	72
A.1.1	Neutral H cross-section	72
A.1.2	H^- cross-section	73
A.2	Ionization in the atmosphere	74
A.3	Total absorption coefficient	75
A.4	Mean absorption coefficients	75
A.5	Technical details	76
B	Figures	77
B.1	Geometry of the system	77
B.2	Flow block diagram of the program	78
B.3	Models of the upper atmosphere	79
B.4	Examples of continuum spectra of a system	85
B.5	Modeling of light curves of selected PCBs	87
B.5.1	UU Sge	87
B.5.2	V477 Lyr	89
B.5.3	V477 Lyr and UU Sge positions on the HR diagram	91
B.5.4	V664 Cas	92
B.6	Mass transfer stability in EHB progenitors	96
B.7	Evolution of EHB progenitors	99
	Bibliography	104
	Summary in Estonian	108

Curriculum Vitae	111
1. Curriculum Vitae	111
2. Curriculum Vitae in Estonian	113
Acknowledgements	115

Chapter 1

Introduction

1.1 The objectives and the structure of the Thesis

The main subject of this Thesis is investigation of precataclysmic binary systems (PCBs) from the standpoint of radiation transfer processes in the atmosphere of the cool companion, which is irradiated from outwards by the hot primary star. The original two-layer model of the atmosphere is described, and the analysis of the computational results is given. With the aid of this model, theoretical monochromatic light curves of selected PCBs were constructed and compared to observations. Origin of Extreme Horizontal Branch objects (EHBs) is also considered, their evolutionary paths are followed in dependence on the initial parameters.

The purpose of this work is to provide a more detailed and physically founded method of the reflection effect treatment, compared to the conventional models with empirical reflection albedo parameter, and also to shed some light on the origin of the possible precursors of PCBs.

This work has the following structure:

1. In the introductory Chapter 1 an overview of the nature of cataclysmic and precataclysmic binary systems is given, the reflection effect and the methods of its treatment are described.
2. In the Chapters 2 – 5 the two-layer model of the illuminated atmosphere of the companion is described. The Section 2 contains the description and the analysis of the processes in the upper layer, where the Lyman continuum is absorbed, the Section 3 describes processes in the inner layer where the diffusion approximation is applied, in the Section 4 the algorithms for constructing light curves are given (calculation of the luminosities of the components, accounting for eclipses, normalization procedure). The Section 5 contains the description of the algorithm of the computer program which realizes the above-described physical model.
3. The Chapter 6 is devoted to the application of the model to selected PCBs. Theoretical monochromatic light curves are constructed and compared to observational data, new sets of parameters' ranges are proposed.

4. The Chapter 7 contains the analysis of the influence of mass transfer, mass loss and angular momentum loss to the orbital evolution of EHBs. The role of mass-transfer determinant factors are discussed and mass-transfer stability conditions are analyzed, an empirical expression for the mass loss rate is proposed.
5. Some additional and illustrative material is presented in the Appendices. In the Appendix A expressions for absorption coefficients are given, and the Appendix B contains the figures.
6. The concluding chapters "Bibliography", "Kokkuvõte", "Curriculum Vitae", "Acknowledgements" contain correspondingly all the bibliographical references, the summary in Estonian, autobiography of the author, and acknowledgements.

1.2 Cataclysmic and precataclysmic binary systems: overview

1.2.1 Cataclysmic binary systems

From late 1930s a large class of cosmic objects is called *cataclysmic variables* (CVs). This class encompasses novae, dwarf novae, magnetic accreting stars and some other "cosmic zoo" exhibits. Some objects belonging to this class demonstrate pronounced flares, their brightness changing in the range of several stellar magnitudes in short timescale. Sometimes such flares were observed twice or more times in one system, some objects display regular flare activity. Even in absence of flares CVs frequently demonstrate periodical or non-periodical variations of brightness. Observational properties of these systems are reviewed in [74]. Below we give a brief description of the main types of this important class of binaries, as well as of the current theories explaining their properties and behavior. We follow [25] and [74] in our overview.

The *novae*, the earliest known and the most prominent type of CVs, outstand by extreme amplitudes of their flares. In several days or even several hours a star becomes brighter up to $6^m - 16^m$ stellar magnitudes (mean amplitude of the flare is about 12^m). The period of quick rise of brightness is followed by more or less slow luminosity drop, and the star returns to its pre-flare stage. This period may vary from less than 100 days (rapid novae as GK Per) to years (extremely slow novae, like RT Ser). There exists a class of so-called recurrent novae which have been observed to flare more than once. The period between successive flares is usually several tens of years, mean flare amplitudes are generally less than 10^m and depend on the period between flares (about $8^m - 10^m$ for periods of ~ 50 years between the successive flares and about 7^m for periods of ~ 26 years). At the present stage of knowledge it is believed that all the

novae are recurrent, and the reason why only one flare has been observed at the majority of these objects is very long period between the successive flares. Nova-like stars constitute another group of objects, which is difficult to attribute with the above-mentioned groups of novae due to lack of data. These objects are similar to novae in the minimum light, and probably most of them are novae with no flares observed in the historic time. Some of them are likely to be polars, dwarf novae or symbiotic stars.

Pre-nova star is a hot blue object with rapid chaotic change of brightness. During the flare brightness rises steeply, the maximum is usually sharp, then brightness drops smoothly by $3^m - 4^m$. This smooth drop is followed by semi-periodic light variations with the amplitudes of about 1^m and periods of several days. In slow novae, this stage is followed by steep drop to the intermediate minimum, steep second rise and the final drop. Regular novae achieve this stage in damping of semi-periodic oscillations. When brightness falls by about 6^m in respect to the maximum light, slow drop stage begins, and the star returns slowly to the (quasi)stable ex-nova stage which is similar to the stage of pre-nova.

Some hundreds of novae are known at present, but due to rapid sequence of events, relatively small part of them have been observed in the maximum light. Mean absolute magnitude in the maximum is considered to be about -8^m .

Most of novae in the minimum light demonstrate hot continuum spectra with wide and bright emission lines of H , $HeII$ and $CaII$. $NIII$ and $CIII$ lines may also be found near the wavelength of $\lambda = 465$ nm. Some recurrent novae contain emission lines, which are characteristic for G, K or M class star. Spectra of some objects with weak variability (as CV Sge) are similar to the spectra of novae. They may be novae which flared in pre-historic time. During flares, the spectrum of a nova passes through several stages, each one beginning before the previous stage ends. Before the maximum light, the spectrum corresponds to a star of B, A or F spectral class. Absorption lines are wide and UV-shifted. Doppler effect is responsible for this shift of lines formed in rapidly expanding transparent envelope. This type of spectrum remains for short time after the maximum is reached. In maximum light, when the envelope radius reaches $\sim 100 R_{\odot}$, the spectrum becomes similar to B, A or F class giants. Sharp absorption lines appear in violet wings of the pre-maximum spectrum, they correspond to the Doppler shift of ~ -1000 km/s. In the red wings bright and wide emission lines of H , $CaII$ and $FeII$ appear with no shift, they correspond to all parts of the expanding envelope. Since density of the envelope drops quickly, soon forbidden lines of $[OI]$, $[NII]$, $[OIII]$ appear in emission, they may become quite intensive. This stage is followed by onset of the so-called Orion spectrum with highly blue-shifted lines of HI , OII , NII , CII . The shift

frequently oscillates chaotically, reflecting changes in the expansion speed. When the envelope is rarefied to densities characteristic for planetary nebulae, the typical nebular spectrum is set, with bright H , He and forbidden lines. In some novae, the nebula becomes visible, and its expansion may be visually followed. After returning to the normal stage, the spectrum of the object corresponds to the post-nova. Sometimes nebular lines or even the nebula itself is observed.

From spectral observations some important conclusions follow. Gas masses ejected with very high velocity are evidence of energetic explosion process on the star. Ejected gas velocities exceed the escape velocity, so the envelope leaves the star, which loses about 10^{-5} of its mass and radiates $\sim 10^{38}$ J.

The majority of *dwarf novae* are similar to novae, but flare amplitudes are smaller and periods between flares are shorter. U Gem type stars demonstrate flares with amplitudes of $2^m - 8^m$ and periods between flares from 20 to several thousands days. SU UMa stars flare with periods about $10 \div 200$ days, but after a small number of cycles ($\sim 3 \div 10$) they have supermaxima which are more lengthy and of higher amplitudes. During supermaxima periodical light variations are observed (so-called superhumps). Z Cam type objects have so short periods of quiet that light variations are nearly continuous.

Spectra of dwarf novae often demonstrate strong H Balmer lines in emission with weak blue continuum. No forbidden lines are seen. Significant width of lines may be explained by Doppler broadening due to rapid rotation of the disc. Weak HeI lines are present, some objects also have $HeII$ line. Rarely $NIII$ and $CIII$ lines are seen. A fraction of the objects demonstrate absorption spectrum of the main sequence star (of G or K class) superimposed onto the above-mentioned spectrum. So, spectra of dwarf novae are similar to spectra of post-novae in the minimum light, the difference is that the excitation degree of the latter is higher. Like spectra of novae, spectra of dwarf novae show the following types of variability: (1) periodical changes attributed to Doppler shifts due to orbital rotation in the close binary system; (2) complicated behavior during flares. The first type of variability is very similar in novae and dwarf novae, but the second type of variability is different. The phenomena characteristic for novae and related to rapid expansion of the envelope are absent in dwarf novae. During the flare, the continuum of spectra of dwarf novae becomes brighter, but the intensity of the emission lines does not change significantly. Near the maximum light in spectra of most of the dwarf novae very wide absorption lines appear, sometimes with central re-emission. They may emerge in the inner, quickly rotating parts of the disc. These lines disappear with the drop of light, and the spectrum in continuum becomes

weaker again.

Nova-like objects with UX UMa as the prototype are similar by their spectral features to novae in pre-flare or post-flare epochs or to dwarf novae during flares, but flare activity have not been detected in them. These objects demonstrate rapid light fluctuations of low amplitudes sometimes accompanied by eclipses.

Polars are objects with very short (from $\sim 1.5^h$ to $\sim 4^h$) orbital periods, their prototype, AM Her, was discovered in 1923. Long-period variability of polars is characteristic for two different stages: the active stage with high light, and the quiet stage with about 2^m lower magnitude. Short-period variability is induced by orbital rotation. Rapid flickering is also present. Spectra with high excitation is similar to an ex-nova spectrum, containing many emission lines (most intensive are H and $HeII$ emission lines). The name comes from strong polarization proper to these objects. Polars are also prominent by their strong X-ray radiation which is significantly more intensive than the novae and the dwarf novae have. It is the reason why sometimes they are classified as X-ray binaries. There is no transit from polars to X-ray binaries, but do exists a gradual transit to dwarf novae (so-called intermediate polars), and it is reasonable to treat them as CVs.

In spite of large difference between the three types of CVs described above (novae, dwarf novae and polars), they have many common properties and may be described by a single model. Their similarity appears in the following features: (1) irregular variability with amplitudes $\sim 1^m$ and periods of $10^2 \div 10^4$ days; (2) rapid flickering with amplitudes $< 1^m$ and periods from seconds to hours; (3) coherent oscillations with amplitudes of $\sim (10^{-3} \div 10^{-2})^m$ and periods of $\sim 10^2$ sec; (4) variability synchronous with the orbital rotation.

All attempts to explain flares of novae and dwarf novae have not been successful until the binarity was revealed for a significant part of these objects. Since then, a substantial progress have been achieved in understanding of their nature. The following model of a CV is generally accepted at the present time.

Model of the CV as a binary star. CV is a binary star consisting of a white dwarf (WD) being the primary component with minute contribution to the continuum, and a secondary component. The secondary may be a red giant star, as in the recurrent nova T Crb or even another degenerated star as in AM CVn, but in most of the CVs the secondary is a red dwarf of a spectral class later than that of the Sun. The secondary component gives only absorption lines in the spectrum, in some CVs it is not appear directly in the spectrum. Most of such systems have periods from about 1^h to about 15^h . According to the Kepler's third law, the semimajor

axis of the system may be found (in units of R_{\odot}) as

$$A = 0.5P^{2/3}M^{1/3} , \quad (1.1)$$

P being the period of the system in hours and M being the total mass of the system in units of M_{\odot} . The secondary component fills in its critical Roche lobe and loses mass through the inner Lagrangian point. In absence of magnetic field-induced perturbations, this matter forms a rapidly rotating accretion disc around the WD. In the region where the matter falls onto the disc, the so called *hot spot* is formed. The hot spot is the result of the shock front action: due to extreme gravitation of the WD, the speed of the matter is very large, and a significant fraction of its kinetic energy is converted to heat (temperatures may reach $\sim 10^5$ K) and radiation, partially in soft X-rays. The accretion disc and the hot spot are the main source of continuum and emission lines. The matter in the disc is braked by friction and falls onto the surface of the WD, transferring the angular momentum. So the spin of the WD accelerates and may reach the limit of stability. If the primary has a strong magnetic field, it impedes accretion disc formation, and the gas flow from the secondary is directed along the field lines onto the magnetic poles of the primary, forming a so-called accretion column. At the same time, magnetic field binds the WD spin to the orbital rotation, synchronizing both motions (so the term *synchronous rotator* has appeared for the polars). With intermediate magnetic fields the accretion disc is present, its inner boundary is limited by the strength of the magnetic field, and the accretion column exists near the surface of the WD. Every binary with a disc has five main sources of radiation: the primary and the secondary components, the accretion disc, the gas flow and the hot spot. It is expected that accretion discs emit energy that may be characterized with a wide range of temperatures. Depending on the transparency of the radiating gas, the radiation is emitted mostly in the form of continuous spectrum, in the form of emission lines or both. In magnetic accreting systems there are four main emitting regions: the stellar components, the gas flow and the accretion column.

The reason for rapid flickering is still unknown. It may be caused by instabilities in the hot spot or in the inner parts of the disc. In polars, rapid flickering obviously appears in the accretion column near the WD. Rapid coherent oscillations may be induced by various processes. In some objects non-radial pulsations of WD may be the case, in others they may arise due to spin of the WD which has a dipole moment: the magnetic field strength is insufficient to bind spin with orbital rotation, and accretion column forms a ring.

Light variability synchronous with orbital rotation occurs when the cool star eclipses the WD, the disc and the hot spot. Since contributions

of the hot spot and the disc vary from system to system, great diversity in orbital light curves exists.

Estimations of masses of CV components give the following results: (1) masses of primaries in dwarf novae lie in the range $0.2 M_{\odot} \div 1.2 M_{\odot}$, masses of primaries in classical novae are $0,6 M_{\odot} \div 0,9 M_{\odot}$, in recurrent novae masses of primaries are $> 1.2 M_{\odot}$. (2) Masses of secondaries may vary from $0.2 M_{\odot}$ to $3 M_{\odot}$. Shortest periods (below 2^h) correspond to lower masses of the secondary, longest to higher masses. Mean absolute magnitudes of novae are about $+4^m \div +5^m$, magnitudes of dwarf novae are $+8^m \div +9^m$. Novae emission lines correspond to higher excitations, so the mass flow is evidently stronger in them.

Satisfactory theories of flares of novae have been established when it became possible to follow the explosion in a wide range of wavelengths, from radio to UV. It was discovered that steep fall of light occurs only in optics. In IR (as well as in radio), the intensity grows even after in optics it drops. This is explained by formation of a dust envelope with masses about $\sim 10^{-4} M_{\odot}$. Through 10^2 days it becomes transparent, and expanding photosphere with fluctuating luminosity becomes visible.

An important role in processes leading to nova explosion plays mass transfer from the red dwarf onto WD. For novae, numerical estimations give transfer rates of $\sim 10^{-8} M_{\odot}/\text{year}$, for dwarf novae ten times smaller. Not all the matter may fall onto the WD: gas flows, carrying a fraction of the matter out of the system, may be formed.

Since WD gravity is very strong, huge energy is necessary to eject the matter with velocities of $\sim 5 \cdot 10^3$ km/sec. Only thermonuclear reactions may disengage such energies. It became evident in 1950-s that flares of novae are the result of thermonuclear explosions of hydrogen accumulated on the WD surface and proceeding from the secondary component. It was demonstrated that for an effective thermonuclear explosion diffusion of H into C -rich nucleus of the WD is needed. The explosion energy grows with increase of C , N and O fraction in the WD. If the fraction of CNO elements does not exceed that of the Sun, the explosion may occur only in the most massive WDs. Theory gives the following results: (1) the explosion is merely probable in WDs with $M \simeq M_{\odot}$, due to a large radius of such a WD; (2) the more massive and luminous the WD is, the less matter it needs to accumulate for H to ignite.

In the initial phase of the flare, not more than $\sim 10\%$ of the accumulated H is ejected. In the following phase of hydrostatic equilibrium the remains of H continue to burn in layers with the energy outcome of $\sim 10^8 \div 10^9$ erg/sec until burn-out of H . During that period, the nova has nearly constant bolometric luminosity, with the effective temperature of the ex-WD of about $\sim 10^5 K$ and $10^1 \div 10^3$ times increased radius,

i.e. the ex-WD severely overfills its critical Roche lobe. The system loses mass until the primary component shrinks again below its Roche lobe and returns to its WD-stage, and the post-nova stage is established.

Although the existing theories of flares of novae may qualitatively explain the observed phenomena, many important problems need a more detailed investigation.

Several theories were proposed to explain *dwarf novae flares*: (1) semi-periodical dynamic instability in the photosphere of the secondary component leading to increase of mass-transfer rate. The red star ejects its outer layers and flares. However, new spectral observations contradict this theory. (2) Thermonuclear reaction in accumulated H on the surface of a WD, intensity of this reaction is insufficient to eject the matter from the system. The ejected matter is braked by the disc and heats it. (3) Semi-periodical fluctuations of mass accumulation rates inducing disc luminosity fluctuations. (4) Re-emission by the disc of the mechanical and radiation energy of a WD. (5) Semi-periodical instability of the disc.

At the present stage of knowledge, the theories (1), (2) and (4) do not explain behavior of the dwarf novae. According to the theory (5), accepted currently for dwarf novae, flares in dwarf novae occur due cyclically repeating sudden change of viscosity in the outer regions of the disc. This mechanism works only with small accretion rates of $\sim (10^{-10} \div 10^{-9}) M_{\odot}/\text{year}$. At higher accretion rates, this process is continuous. In objects like Z Cam, accretion rates may change from values higher than this limit to values lower than this limit. The theory (3) is accepted to explain superflares in SU UMa-type objects. These superflares may be induced by accumulating instabilities of the secondary star leading to periodical increase in matter outflow rates.

There are strong reasons to support the hypothesis that novae and the dwarf novae represent two phases of a very slow periodical alteration. This hypothesis is supported by the fact that some old novae demonstrate dwarf nova-like flares.

The origin of CVs has been widely discussed in the recent time. The most productive idea have been the hypothesis of transfer of an initially long-period system to a short-period CV. Orbital shrinkage may be caused by frictional forces during the common envelope stage, as well as by tidal braking and by magnetodynamic processes. Systems corresponding to transitional stages to CVs may be some types of planetary nebulae with binary nuclei. The evolution of a pre-CV star may proceed according the following scenario. A main sequence star in a binary system expands in the course of its nuclear evolution and loses matter either due to its expansion or due to energy losses by gravity wave radiation and hydrodynamical braking. So mass loss accelerates, the orbit shrinks and the period becomes

shorter. Finally a WD is left with a low-mass main sequence companion.

1.2.2 Precataclysmic binaries

Precataclysmic binaries is a small group of detached binary systems discriminated in the beginning of 1980-s according to the following criteria: (1) the primary component is a hot WD or a WD precursor; (2) the secondary component is a low-mass unevolved main sequence star with mass of $M < 1 M_{\odot}$; (3) orbital periods are so short, in most cases $P_{\text{orb}} < 2^d.4$, that PCBs may have formed only by passing through the common envelope stage; (4) the system is nucleus of a planetary nebula. In this overview we follow [52] to describe the principle features of these objects.

Binary nuclei of planetary nebulae are discovered by radial velocity curves, by combined spectra with a late type star spectrum dominating in the optics and a hot component spectra found in the UV. Most of the PCBs are characterized by luminosity changes caused by very strong reflection effect (see the Section 1.3). PCBs with observed eclipses are not frequent. Effects of selection play an important role in discovery and attributing of objects of this class: their lifetime is short, being limited by the planetary nebulae lifetime ($\simeq 10^4$ years) and by the WD cooling timescale ($\simeq 10^7$ years), and their absolute magnitudes are low. A review of PCBs is given in [62], it contains most of such systems known by that time. A later comprehensive overview of PCB objects and candidates is presented in [9], together with their principle parameters and bibliographic references to original works. The Table 1.1 is taken from [62] and appended by new objects and fresh data from [9] (few questionable objects were excluded), so this table lists most of the presently known PCBs. The table indicates the type of the system (CPN stands for central star of a planetary nebula, Ecl. for eclipsing binary) and its period (in days), and lists masses of the components M_1 and M_2 (index "1" corresponds to the hot primary), the radius of the secondary component R_2 and the semimajor axis of the system R_{sep} , all in solar units. With their typical separations and periods, PCBs provide an important link between short period CBs and wide pairs.

As it is seen in the Table 1.1, for many PCBs physical parameters are not known or known with low precision. Not only insufficiency of observational material plays the role is the case, but also the fact that many methods applicable to non-relativistic components cannot be directly applied to PCBs. X-ray and UV radiation from hot subdwarfs are poorly known. The nature of cold illuminated companions is not sufficiently studied. Analysis of physical conditions in the upper layers of cold companions indicate presence of temperature inversion, which manifests itself in limb brightening (see for instance [60], [58]), that is contrary to the common limb-darkening law in ordinary main sequence stars. Cold companions' upper atmosphere

evaporation by anisotropic X-ray and UV radiation of hot primaries is very important and is still scarcely studied. Semi-analytical and numerical models support the idea that hot chromospheres are formed if the irradiating bolometric flux exceeds 3–4 times the proper flux of the unevolved star. UV and soft X-ray radiation penetrates the atmosphere by $10^6 \div 10^7$ cm, that is comparable to the thickness of chromospheres of late type dwarfs and thus it should favor chromospheric activity. With these effects, the standard mass-radius relation valid for main sequence stars (and used to estimate timescales of PCBs breaking by magnetic stellar wind) may be violated.

Analysis of evolutionary scenarios of binary systems demonstrates that wide pairs (where nuclear evolution passes nearly like in single stars) with significantly different masses of the components are likely to form a common envelope. A good overview of the common envelope phase is given in [30]. Below we describe the most important features of this evolutionary stage.

Several mechanisms that may lead to the Roche lobe overfilling are known. The most frequently realized one is obviously the nuclear evolution of a more massive component when it reaches the giant or supergiant stage. The giant should have an extensive convective envelope that tends to further expansion when the star loses mass, and the mass transfer timescale should be much shorter than the thermal timescale of the giant and than the relaxation timescale of the accretor. Another mechanism for the orbital shrinkage is angular momentum loss due to the magnetic stellar wind and to gravitation waves. For effective magnetic breaking, a strong stellar wind and magnetic activity are needed in one of the components, as well as sufficient proximity of the components. This mechanism works with orbital periods of $5 \div 10$ days. The gravitation wave mechanism is dominant with component separations of $(1 \div 3) R_{\odot}$, and one of the components should be a WD or a neutron star.

A wide pair evolution to a PCB goes in the following way. The initial pair consists of two main sequence stars of different masses with separation of several astronomical units and a period of $(10^2 \div 10^3)$ days. When the more massive component fills in its critical Roche lobe, unstable accretion onto the low mass companion begins. The latter also fills in its Roche lobe after having accreted about 1% of its mass, and the common envelope is formed. Consequently follows effective breaking and approach of the components, with possible loss of synchronization between the giant spin and orbital rotation. Thereafter the common envelope is ejected carrying away a significant fraction of the primary mass and the angular momentum of the system. The low-mass companion approaches to the revealed nucleus of the giant, the orbital period becomes much shorter. At the end of

the common envelope stage, a planetary nebula remains with a hydrogen (and possibly helium) hot burning subdwarf and a low-mass main sequence companion in the center of the nebula.

Binary systems emerging from the common envelope stage with periods shorter than several days may pass through the second semi-detached system's phase. Since the low-mass companion will be the donor in this case, mass transfer should be smooth and obviously should cause a nova explosion. Theoretical estimations show that for a PCB a typical timescale of breaking by the magnetic stellar wind is $\sim 5 \cdot 10^5$ years, and typical values of radii of cold companions indicate that the unevolved star should fill in its Roche lobe in the course of the PCB evolution. Thereafter the accretion onto the WD begins and cataclysmic activity develops.

It follows through estimation of orbital shrinkage timescale t_{sd} that only about half of the known systems are "genuine" PCBs, *i.e.* will evolve from the detached to the semi-detached state (*i.e.* to CBs) in the timescale of $t_{sd} < 10^{10}$ yr. The reason why only a small fraction of the observed PCB systems possesses short orbital shrinkage timescales is observational selection. The probability to find a PCB with the given t_{sd} is roughly in inverse proportion to this timescale, so the number of PCBs which are born with a short t_{sd} is much larger than that is actually observed, but most of them quickly evolve to CBs.

It depends on orbital parameters of a close binary emerging the common envelope stage whether the low-mass companion fills its Roche lobe within the evolutionary timescale, *i.e.* whether a PCB reaches the cataclysmic stage. This question may be solved by observations and by further theoretical modeling. Results of observations should be interpreted on the basis of the observed effects. In the Chapter 7 we investigate the influence of the parameters of a close binary system on its further evolution in attempt to clarify which evolutionary scenarios may lead to formation of a close binary and why binarity may be a crucial factor in producing Extreme Horizontal Branch objects (EHBs, see also [60]).

Despite the fact that PCBs have been intensively studied for the last two decades, a number of important problems remains open. As it has been already mentioned, PCBs are discovered mostly due to a pronounced reflection effect. Since the early paper [48], the problem of anomalously high reflection effect amplitude remains unsolved (see the discussion in [20]). We see the key to the solution of this problem in reprocessing of the Lyman continuum of hot subdwarfs in the uppermost atmospheric layers of late type unevolved companions.

Table 1.1 Physical parameters of PCBs

Object	Type	P ^d	Spect. type	M ₁ /M _⊙	M ₂ /M _⊙	R ₂ /R _⊙	R _{sep} /R _⊙
V651 Mon	CPN, Ecl.	15.991	WD?+A5 V	0.40±0.05	1.8±0.3	2.2±0.2	35.1–42.5
FF Aqr	Ecl.	9.2076	sdOB+G8III	0.5	2.0	5.7	25.05
Feige 24		4.23160	DA+M1.5 V	0.44–0.50	0.26–0.33	0.30±0.05	11
Be UMa	Ecl.	2.2911667	WD+M1.5 V	0.6±0.1	0.6–0.8	1.18±0.1	8.7±0.7
HD 49798		1.547671	sdO+F4-KO	1.75±0.1	0.8–2.5		
VW Pyx	CPN	0.6707	sdO+?				
EG UMa		0.667651	DA+M4–4.5 V	0.39±0.05	0.36±0.05	0.25±0.05	≥2.55±0.07
UX CVn	Ecl.?	0.573703	B2–3+K–M	0.4±0.1	0.48±0.05	0.52±0.05	2.8±0.1
HZ 9		0.56433	DA2+M4.5eV	0.5±0.1	0.28±0.04	0.22±0.05	≥0.60±0.06
V471 Tau	Ecl.	0.5211831	DA+K2 V	0.72	0.8	0.85	1.5
V477 Lyr	CPN, Ecl.	0.4717291	sdO	0.51±0.07	0.15±0.02	0.42±0.03	2.2–2.5
UU Sge	CPN, Ecl.	0.46506918	sdO+G–K V	0.6–0.9	0.4	0.7	≈3
KV Vel	CPN	0.357113	sdO	0.6±0.2	0.25±0.06	0.38±0.02	2.1±0.1
IN Com	CPN	1.7545	sdO+G5III	0.9–1.9	0.1(?)		
GK Vir	Ecl.	0.344330809	WD+M3–5 V	0.51±0.04	0.1	0.15	2.0±0.2
RR Cae	Ecl.	0.30371	DAwk+Me V				
AA Dor	Ecl.	0.261539712	sdOB	0.2–0.3	0.037–0.048	0.09±0.02	1.06–1.21
NN Ser	Ecl.	0.130080	WD+M4–M6 V	0.57 ± 0.04	0.1–0.14	0.15–0.18	1
HW Vir	Ecl.	0.116719631	sdB+a /ate M	0.25	0.12		0.23
MT Ser	CPN	0.1132269	sdO+M V	0.6(?)	0.1–0.3	0.13–0.34	0.90±0.05
BD+66°1066	CPN	0.0604(?)	O7+WR				
LW Hya	CPN	0.7653	sdO+G8 III				
V6571 Mon	CPN	15.991	WD(?) +A5 V	0.40±0.05	1.8±0.3	2.2±0.2	35.1–42.5
QR Sge	CPN	2.3583	?+WN8				
PG 0308+096		0.28431	DA2+M4.5e V	0.39 ^{+0.13} _{–0.10}	0.18±0.05	0.21±0.02	1.5±0.3
RE 1016–053			DAO+M4(1)	0.57±0.03			
PG 1026+002		0.597257	DA3+M4e V	0.65 ^{+0.26} _{–0.21}	0.22±0.05	0.25±0.03	2.9±0.3
RE 1629+781			DA+M2–5 V				
EUVE 2013+40		0.7059	DAO+M3 V	0.48–0.72	0.3		
SP1	CPN	2.91					
BPM 71214		0.1806					
GD 25		0.17366	DA2+M3–5	0.48±0.02	0.22±0.02	0.27±0.02	1.17±0.01

1.2.3 Extreme Horizontal Branch objects

Underluminous sdB stars are thought to be helium burning stars with very low mass hydrogen envelopes. They can be identified with models for Extreme Horizontal Branch (EHB) stars. Their effective temperatures ($> 25\,000\text{ K}$) are high, as well as surface gravities ($\log g > 5$), which places them on EHB. So, they appear in the same region of $T_{\text{eff}} - \log g$ plane as evolutionary tracks for core *He* burning stars with core masses of about $0.5 M_{\odot}$ and extremely thin ($\leq 0.02 M_{\odot}$) inert hydrogen envelopes (see details in [22], [66]). Quite recently it has been discovered that most of EHB objects are primary components of binary systems with orbital periods P_{orb} ranging between $0^d.12$ and 27^d in pairs with main sequence low mass companions (see [45], [39]). So, these systems may be close relatives of pre-cataclysmic and cataclysmic binaries, being a link between them and wider pairs. A number of evolutionary scenarios have been proposed during the last ten years to explain the origin of EHB stars (see the discussion in [11], [66]). It is currently accepted that EHB stars form due to enhanced mass loss on the Red Giant Branch (RGB) when the degenerate helium core of a star close to the RGB tip loses almost all surrounding hydrogen convective envelope, but the core goes on to ignite helium despite a dramatic mass loss and may appear as sdB star (see the details in [11]). It remains unclear why binarity seems to play a crucial role in formation of sdB stars.

1.3 The reflection effect

Irradiation effect (a commonly accepted term *reflection effect* will be used hereinafter) arises in a binary system when a considerable portion of radiation of each components falls onto the upper layers of another component. The incident flux from outwards causes heating of the illuminated photosphere and atmosphere and alters characteristics of their radiation. At different orbital phase angles the illuminated star is directed to a terrestrial observer with crescents of its surface heated to different extent. As a result, observed luminosity of the system experiences variations. Historically, this effect is known as "reflection effect", since outwardly it is provoked by the similar cause which induces changes in luminosity of planets: incident flux is "reflected" by the surface of an object.

The real situation is much more complicated. Stellar photosphere and atmosphere is not a solid body characterized by and an albedo parameter. Incident radiation experiences complicated transformation processes inside the outer stellar layers. Some portions of this radiation are absorbed by different agents composing the gaseous outer layers, some portions are scattered, flux with short wavelengths may cause additional ionization of gas and is re-emitted in lines, and so on. Many factors are involved in

formation of reflection effect-induced light curves, and hardly is it possible to take them all into account. One may mention convection, horizontal energy transport, shock waves, pulsations etc. Simplifications are inevitable for analytical and numerical models of the subject.

1.3.1 On modeling of the reflection effect

Earlier investigations springing from the classical works by Eddington, Milne, Minsky, Martynov, Pustyl'nik, Ruciński (see for instance [12], [37], [43], [44]), as applied to Algol-type and similar systems, are not discussed in the frame of the present work.

A number of reflection effect modeling methods have been proposed and applied in practice during the last decades. In different models the reflection effect is considered in different ways. In [46] a geometrical model is proposed, with due account of zones near the local horizon illuminated only by a fraction of the disc of the illuminating star (we also follow this approach with several modifications and improvements, see the Chapter 4). Some authors use an artificial albedo coefficient (usually bolometric, *i.e.* wavelength-independent) which encloses a lot of physical effects into a single parameter (see, for instance, [48]). In [42], [51], [65] and [70], grey solutions are proposed for temperature distribution within the heated outer layers of the illuminated star.

Frequently such simplified approximations give quite good results fitting with observations. This is because usually amplitudes of the reflection effect are not large in comparison with other effects participating in formation of light curves of a variable star (such as eclipses, ellipticity of the components and so on). The reason is that in common binary systems semi-major axes are long enough, so heating flux that alters the outer layers of the star is small, and the illuminated atmosphere and photosphere are not altered substantially. Thus, the reflection effect is only of a second order in such systems.

1.4 Conventional treatment of the reflection effect in PCBs

As it was mentioned in the Section 1.2.2, one of the main features of PCBs is proximity of their components. The second important factor is extremely high temperature of the evolved companion (WD or WD precursor), which sometimes may exceed 10^5 K. On the contrary, the secondary, being unevolved main sequence star with moderate effective temperatures of $3000 \div 5000$ K, is of low intrinsic luminosity. This is the reason why very favorable conditions exist in PCBs for the reflection effect to manifest itself in a pure state. In absence of eclipses, this effect is usually the main light curve forming factor in these objects, and thus it is one of the most

characteristic features of PCBs. Due to short semi-major axes and high temperatures of the hot star, the flux falling onto the outmost layers of its companion is very strong, it is able to alter substantially the structure of the photosphere and the upper atmosphere, giving raise to a number of manifold and complicated physical processes. Strong UV and even soft X-ray flux impinging the atmospheric layers alter considerably the structure of the corona and the chromosphere and may be a cause of evaporative wind (for more details see [55]), pulsations or, in broad terms, of instability of various types. Thus, significant departures from the standard mass-radius relation valid for main sequence stars may be expected. All these circumstances frequently turn conventional approaches to treatment of the reflection effect to be inadequate, therefore simplified approaches may be insufficient for satisfactory description of the processes in the atmosphere of the secondary. However, such methods are still of wide use because of their simplicity and obviousness, and they frequently enable one to quickly obtain valuable results providing satisfactory fit of observations in general.

The traditional and common method for approximate modeling of the reflection effect in PCBs is introduction of a reflection albedo coefficient (see, for instance, [48]). It means enclosing of all physical effects into a single characteristic, which sometimes is adopted to be function of local parameters (for instance, in [19] different order power laws of temperature for the reflection albedo coefficients are adopted, the albedo coefficient is defined individually for each surface element of the secondary). Since simplified qualitative models of the reflection effect are frequently insufficient in the case of PCBs, more detailed analysis of primary star flux transformation in the atmosphere of the cool companion is needed. During the recent years a number of works treating the reflection effect in some specific cases has appeared. For instance, a possible bifurcation in solutions for a strongly irradiated atmosphere with LTE is pointed out by [27]. In [2] is treated the problem of gravitational brightening in convective and radiative atmospheres affected by outer flux. In [10] a good overview of the problem is presented, including geometrical and radiative transfer foundations, effects of multiple atmospheric reflections are investigated and numerical results for light curves and polarization curves are demonstrated. A comprehensive study of the precataclysmic binary BE UMa has been made by [15] where a grid of model atmospheres CLOUDY have been applied for a detailed investigation of the reflection effect in this object. However, many problems related to the reflection effect still remain unresolved, and PCBs present specifically interesting objects for investigations in this field, since many phenomena induced by the reflection effect (*i.e.* strong departures of LTE, instabilities of the atmosphere, etc.) are combined in them.

1.5 Advanced method of the reflection effect treatment

1.5.1 Problem formulation

In the last several years we have systematically reevaluated the analysis of observations of PCBs (see [53], [54], [56], [57]; [58], [59]). Our current activity in this field has been motivated by the following considerations:

i) Although PCBs are detached binaries, conventional treatment of the reflection effect may not be adequate for those with very hot subdwarf primary components, $T \sim 10^5 K$, where the predominant portion of the incident flux is concentrated in the Lyman continuum (L_c). Soft X-ray and UV radiation should considerably alter the structure of the outer layers of the cool companion, causing significant departures from the standard main sequence mass-radius relation. In addition, reprocessing of L_c radiation should seriously affect the boundary conditions of the irradiated photospheres in comparison with the conventional models (*e.g.* [48]).

ii) Detailed data on X-ray radiation from hot primaries impinging on the atmospheres of low mass cool companions are still scanty. Modeling the physical conditions in the uppermost layers of such irradiated atmospheres and studying the reflection effect can shed some light on the energy distribution of the subdwarf primaries.

iii) Pulsations have been discovered in EC14026 type stars (rapidly oscillating sdB stars named by the first member of the class discovered in 1997 by Kilkenny *et al.* (see [32])); it is still unknown whether binarity is essential in explaining multiperiodicity observed in them. Roughly 30% of EC14026 type stars forming a subclass of PCBs are found in obvious binaries (see [61]). The question of influence of binarity on characteristics of the pulsation spectra is one of the important topics in studies of these objects.

1.5.2 Brief description of the model

In the course of our studies, we have compiled an original two-layer model of the secondary atmosphere and realized it in a computer code.

For due account of the impinging flux, the surface of the secondary component is divided into circular zones with the common center in the substellar point.

A two-layer model atmosphere is created for each zone. In the upper layer a set of equations of hydrostatic, ionization and thermal equilibrium is solved explicitly to calculate recombinational spectra of the reprocessed emergent radiation for an optically thin plasma. Contributions from free-free and bound-free transitions are considered, diffuse radiation is taken into account, but effects of self-absorption of the re-emitted radiation are neglected (see the Chapter 2). In the course of our studies it was found

that down to optical depths of $5 \div 10$ in the Lyman continuum, only several tens percent of the impinging flux may be spent on hydrogen ionization, the rest of energy is spent on heating of electronic gas or in other ways; possible energy drains are for instance shock waves or pulsations. It means that due to severe overheating of the uppermost layers thermal stability is non-existent. Due to this instability we had to introduce a parameter which would take into account imbalance effects. In this role we use a coefficient which equalizes the impinging flux in the Lyman continuum and emitted recombinational radiation. From calculations it follows that this coefficient varies from about unity (near the limb) up to several units in the substellar point. At the same time making this coefficient free parameter we may evaluate instability influence on the escaping radiation. In the optical band, the escaping flux is much higher than the impinging flux. This fact proves that every L_c quantum produces several optical quanta.

In the lower atmosphere the Eddington approximation is adopted (see the Chapter 3) with due account of various absorption agents (H , He , H^+ , one metal). Both layers are "sewed" together with the help of boundary values (temperature and density).

Compiled a model atmosphere for a certain zone, it becomes possible to compute escaping radiation intensity and angular distribution and to construct monochromatic light curves. It also becomes possible to investigate processes in the atmosphere and their characteristic features, to study influence of these processes on the escaping radiation and on reflection effect-induced light curves. Light curves are constructed taking into account both eclipses and transitions, a modification of the Napier's method [46] is used (see the Chapter 4). So, presetting different initial parameters (masses, radii and effective temperatures of the components, chemical composition of the atmosphere of the secondary, limb darkening coefficient of the primary, orbital separation and inclination angle, imbalance parameter and so on), we are able to compile model atmospheres for different surface elements of the secondary component and to compute theoretical light curves, that serve as basis for comparison with observational data. For detailed description of the algorithm, see the Chapter 5.

We have applied the computer code based on our model to several PCBs, the results are presented in the Chapter 6.

Chapter 2

Upper atmosphere model

2.1 Dilution coefficient

The flux impinging upon any point on the surface of the secondary component is diluted, the extent of this dilution depends on geometry of the system and on the position of the considered point on the surface of the star. This position is defined by its angular distance from the substellar point δ (see the Figure (1) taken from Napier [46]). We compute the dilution coefficient W_δ using the Napier's method with several improvements. In general, the dilution coefficient may be represented as

$$W_\delta = W_1 [(1 - u_1)X + u_1Y], \quad (2.1)$$

u_1 being the limb-darkening coefficient of the illuminating component. For the sake of simplicity we consider u_1 to be constant. Such approach is generally accepted, see for instance [16]. The value $u_1 = 2/3$ is adopted everywhere. Usually this value of the limb-darkening coefficient is used in the bolometric case, but since data is scarce for monochromatic values, we apply it also for the monochromatic case.

To find W_1 , X and Y in (2.1), we calculate the following values, which are based on geometry of a binary system:

$$\begin{aligned} \rho &= \sqrt{1 + a_2^2 - 2a_2 \cos \delta} \\ \alpha &= \begin{cases} \arcsin(\sin \delta / \rho), & \text{if } \cos \delta \geq a_2 \\ \pi - \arcsin(\sin \delta / \rho), & \text{otherwise} \end{cases} \\ \beta_1 &= \arcsin(a_1 / \rho). \end{aligned} \quad (2.2)$$

Here a_1 is the radius of the primary in the units of the separation R_{sep} , a_2 is the radius of the secondary in the same units, ρ is the distance of the considered point on the surface of the secondary from the center of the primary (in the same units), β_1 is the angular radius of the primary as it is seen from the considered point, and α is the angle of the incident flux with the local normal.

The following three cases are considered separately:

- (i) $\alpha - \beta_1 > \pi/2$.

This corresponds to the whole disc of the primary to be below the local horizon of the considered point on the surface of the secondary.

The value $W_1 \equiv 0$ is applied for this case, signifying lack of incident flux.

(ii) $\beta_1 \geq 4^\circ$.

Napier's tables may be used, with X and Y given as functions of α and β_1 . We find X and Y by interpolation of these tables and set $W_1 \equiv 1$ in (2.1).

(iii) $\beta_1 < 4^\circ$.

Interpolation of Napier's tables is impossible, because their step exceeds values of β_1 . To overcome this difficulty, we compute X and Y directly as

$$\begin{aligned} X &= \pi \sin^2 \beta_1 \cos \alpha \\ Y &= \frac{2}{3} X \end{aligned} \quad (2.3)$$

and check whether the disc of the primary is fully above the local horizon (*i.e.* whether the condition $\alpha + \beta_1 \leq \pi/2$ is fulfilled). If this condition is fulfilled, the unit value for W_1 is adopted. Otherwise, if the disc of the primary is only partially above the local horizon, W_1 is adopted to be equal to the relative projection area of the portion of the disc, situated above the horizon, to the whole area of the projection of the primary's disc onto the celestial sphere for the considered point:

$$W_1 = \frac{1}{2} + \frac{\frac{\pi}{2} - \alpha}{\pi \beta_1} \sqrt{1 - \left(\frac{\frac{\pi}{2} - \alpha}{\beta_1}\right)^2} + \frac{1}{\pi} \arcsin\left(\frac{\frac{\pi}{2} - \alpha}{\beta_1}\right). \quad (2.4)$$

2.2 Net acceleration in binary system

To compute the net acceleration in a binary system, we consider both stars to be spherical and with spherically symmetric mass distribution (*i.e.* we neglected mutual distortions), synchronization of the orbital and the spin rotations is supposed to have been established in the system, and we also neglect thickness of the atmosphere relative to the radius of the secondary R_2 . In this approximation, a unit mass at the selected point of the secondary's surface is subject to the vector sum of the following accelerations:

(i) gravitational acceleration by the primary star,

$$A_1 = \frac{GM_1}{t^2}, \quad (2.5)$$

where $t = \sqrt{R_{\text{sep}}^2 + R_2^2 - 2R_2R_{\text{sep}} \cos \delta}$, R_{sep} being the distance between the centers of the stars, δ being the angular distance of the selected point from the substellar point, and G being the gravitational constant;

(ii) gravitational acceleration by the secondary star,

$$A_2 = \frac{GM_2}{R_2^2}; \quad (2.6)$$

(iii) and centrifugal acceleration

$$A_{\text{cf}} = \frac{GM_1}{R_{\text{sep}}^2} \left(1 - \frac{M_1 + M_2}{M_1} \frac{R_2}{R_{\text{sep}}} \cos \delta \right), \quad (2.7)$$

M_1 and M_2 being respectively the masses of the primary and the secondary components.

Found all accelerations, we compute their projection A_x onto the axis connecting the centers of masses, the projection to the rotational axis A_y and, finally, the net acceleration G_δ :

$$\begin{aligned} A_x &= -A_1 \cos \alpha + A_2 \cos \delta + A_{\text{cf}}, \\ A_y &= A_1 \sin \alpha + A_2 \sin \delta; \\ G_\delta &= \sqrt{A_x^2 + A_y^2}. \end{aligned} \quad (2.8)$$

(here $\sin \alpha = \frac{R_2}{t} \sin \delta$, according to the law of sines).

2.3 Equilibrium conditions in the atmosphere of the secondary

Here we describe our model of the uppermost atmosphere where the incident L_c flux is fully reprocessed, and introduce several simplifying assumptions. We consider the primary star to irradiate as absolutely black body with an effective temperature of T_{1eff} , both stars are spherical. Since the effective temperature of the primary corresponds to blackbody temperature between 30 000 K and 150 000 K, a significant portion of incoming energy is concentrated in the UV portion of the spectrum, namely $\lambda < \lambda_{L_c}$, with $\lambda_{L_c} \simeq 912 \text{ \AA}$. This irradiating far UV flux falls onto the rarefied layers of the chromosphere and the upper atmosphere of the secondary, and processes in these layers can be treated, in qualitative terms, similarly to the processes taking place in planetary nebulae. It is intuitively clear that there should be pronounced deviations from LTE in such overheated medium. To escape sophisticated non-LTE calculations that would make

our model of the reflection effect extremely complicated, we adopted the "on-the-spot" approximation for model atmospheres (see [47] for details), *i.e.* we assumed that the free path of a photon is negligibly small compared to the dimension of the layer where the incident L_c flux is absorbed and re-processed. We assume that in the upper non-LTE layers H is predominant opacity agent, and solve the system of three balance equations:

(*) the equation of ionization balance

$$N_0 W_\delta \int_{\nu_0}^{\infty} \frac{B_\nu(T_{\text{1eff}}) k_\nu(T) \exp(-\tau_\nu)}{h\nu} d\nu = N_e N^+ \alpha_{\text{rec}}(T), \quad (2.9)$$

α_{rec} being the recombination coefficient to all levels except for the ground level,

$$\alpha_{\text{rec}} \simeq \frac{1.627 \cdot 10^{-11}}{\sqrt{T}} \left(1 - 0.720 \ln \frac{T}{10\,000} + 0.0271 \sqrt[3]{T} \right); \quad (2.10)$$

(*) the equation of thermal equilibrium

$$N_0 W_\delta \int_{\nu_0}^{\infty} \frac{B_\nu(T_{\text{1eff}}) k_\nu(T) \exp(-\tau_\nu)}{h\nu(h\nu - h\nu_0)^{-1}} d\nu = 4\pi \int_0^{\nu_0} q_\nu(T) d\nu, \quad (2.11)$$

q_ν being the cooling function,

$$q_\nu = \epsilon_\nu (1 + C\tau_\nu). \quad (2.12)$$

The emission coefficient for recombinations ϵ_ν (both bremsstrahlung and bound-free transitions) is taken by [36],

$$\epsilon_\nu = \frac{N_e^2}{T^2} \Phi_\nu(T, N_e) \exp\left(-\frac{h\nu}{kT}\right); \quad (2.13)$$

Φ_ν is defined as

$$\Phi_\nu = F_\nu(T) + G_\nu(T, N_e). \quad (2.14)$$

F_ν and G_ν are the Gaunt factors for free-free and bound-free transitions respectively:

$$F_\nu = 2\theta \left[\sum_{n=n_0}^5 \frac{g'_n}{n^3} e^{\theta/n^2} + g'_\infty \sum_{n=6}^{\infty} \frac{1}{n^3} e^{\theta/n^2} + 25(g'_5 - g'_\infty) \sum_{n=6}^{\infty} \frac{1}{n^3} e^{\theta/n^2} \right], \quad (2.15)$$

$$G_\nu = \begin{cases} 0.54 \ln \left(5.0 \cdot 10^7 \frac{T^{\frac{3}{2}}}{\nu} \right), & \text{if } \nu \gg \nu_p \\ 0.54 \ln \left(3.1 \cdot 10^3 \frac{T^{\frac{3}{2}}}{\sqrt{N_e}} \right), & \text{otherwise.} \end{cases} \quad (2.16)$$

g'_n is taken by (A.3), $\theta = \frac{I}{kT}$, n_0 and I defined in comments to (A.3), plasma frequency $\nu_p \simeq 9.0 \cdot 10^5 \sqrt{N_e}$;

(*) the equation of hydrostatic equilibrium,

$$N(r) = \frac{P_{r=0}}{(1+X)kT} \exp \left(\frac{m_p G_\delta r}{(1+X)kT} \right), \quad (2.17)$$

where

$$X = \frac{N_e}{N_0 + N_e} \quad (2.18)$$

stands for ionization degree ($X = 1$ when H is completely ionized).

In this set of equations, N_0 , N_e , N^+ are respectively the number density of neutral H atoms, of free electrons and of protons, κ_ν is the absorption coefficient for neutral hydrogen, B_ν is the Planck function, T_{1eff} is the effective temperature of the illuminating star, W_δ is the local value of dilution factor (corresponding to the angular distance δ from the substellar point of the irradiated component, see the Section 2.1), G_δ is the effective gravity acceleration (*i.e.* the net acceleration at the respective point, see the Section 2.2), τ_ν is the monochromatic radial optical depth counted from the surface of the star, P is the gas pressure, ν_0 is the frequency corresponding to the Lyman limit. The optical depth-dependent term is added to the cooling function (2.12) to approximately take into account contribution from diffuse radiation; C is an empirical constant of order of unity (the value of $C \equiv 1.5$ is adopted). The meaning of other notations is self-explanatory.

We neglect ionizations from upper levels in the equation of ionization balance (2.9) and the role of collisions (see the corresponding estimation in the Section 2.7.1, where these factors are proved to be negligible in the first approximation). The applicability of our simplified description have been checked by numerical estimations, which have showed that the upper layer of the irradiated atmosphere is opaque to Lyman continuum photons,

whereas quanta with lower energy penetrate freely through the same layer with little absorption. The non-LTE layer in the first approximation may be considered transparent to radiation in the optical waveband.

The system of the equilibrium equations (2.9), (2.11) and (2.17) is solved numerically step by step beginning from the outward layers downwards the atmosphere till a limiting depth R_{lim} where the ionization degree of medium drops to diminutive values (see technical details in the Section 2.6). In the course of the solution process, the parameter $T_{\text{eq}}(r)$ (having the dimension of temperature) is obtained as a geometrical depth r function, together with the ionization degree $X(r)$, the electron concentration $N_e(r)$ and other physical quantities. Since LTE does not exist in the upper atmospheric layer, T_{eq} cannot be treated as any physical temperature but rather a parameter characterizing the state of matter.

2.4 Ionization conditions in the upper atmosphere

In addition, at each integration step we calculate the value of the ionization temperature $T_{\text{ion}}(r)$ (found numerically from the Saha equation for the given ionization degree X):

$$\frac{N_e^2}{N_0} = 2 \left(\frac{2\pi m_e kT}{h^2} \right)^{\frac{3}{2}} \exp \left(-\frac{h\nu_0}{kT} \right), \quad (2.19)$$

m_e being electron mass.

We also estimate the temperature of electronic gas $T_e(r)$, assuming that the surplus of photon energy over the threshold of ionization energy of $h\nu_0 = 13.5 \text{ eV}$ is used for heating of free electrons, *i.e.* using the relation

$$N_0 W_\delta \int_{\nu_0}^{\infty} B_\nu(T_{\text{1eff}}) k_\nu \exp(-\tau_\nu) \left(1 - \frac{h\nu_0}{h\nu} \right) d\nu = kT_e N_e N^+ \beta(T_e). \quad (2.20)$$

Here $\beta(T)$ is the collisional cooling function taken from [29] where its empirical expression is given in the following form:

$$\beta(T) = (1.09 + 0.158 \cdot 10^{-4} T) \cdot \alpha(T), \quad (2.21)$$

the recombination coefficient α to be found according to (2.10).

Values of T_e can be regarded as an order of magnitude estimate only, since they depend on running values of physical parameters of the model, mainly on $T_{\text{eq}}(r)$ and $X(r)$. As one can see from the equation (2.20), to find $T_e(r)$ we need to know the ionization degree $X(r)$. Our attempts to incorporate the equation (2.20) directly into the set of equilibrium equations (2.9), (2.11), (2.17) in order to find self-consistent values of $T_e(r)$

along with other physical parameters of the model, have failed. In other words, in the framework of our model it is impossible to find an equilibrium solution both for neutral H and electronic gas.

2.5 Reprocessed radiation intensity and spectrum

From our models we may conclude that the largest portion of flux in the Lyman continuum is absorbed in the rarefied upper layer. Energy of Lyman continuum photons is reprocessed into energy of less energetic quanta – as a result of hydrogen ionization from the ground level and subsequent recombinations onto upper levels – and in addition it is expended on heating the electron gas. Thus, the reprocessed radiation has a typical recombination spectrum, and its intensity may be obtained from the equation

$$J_{\text{rec}}(\nu) = 2\pi K \int_0^{R_{\text{lim}}} q_\nu(T) dr, \quad (2.22)$$

where K is a normalization coefficient (the angular distribution of the outgoing radiation is considered uniform, so the factor 2π emerges from integration over solid angles). We calculate the intensity of the emergent radiation by integrating the cooling function q_ν from (2.12) over the full depth of the layer where L_c flux is reprocessed, taking into account variations of the particle density and temperature within the atmosphere. In the upper layers, where τ_ν is negligible, (2.12) asymptotically approaches to the total emission coefficient ϵ_ν from (2.13), in deeper layers self-absorption becomes important correspondingly to the value of the constant C .

The equation (2.22) is valid for optically thin plasma. This is a good approximation for near-UV and optical regions, but fails at longer wavelengths, *i.e.* in far infrared regions where effects of self-absorption become important. It is evident that for an accurate calculation of the recombination spectrum one should first calculate the populations of different levels of H . Since our rough model does not take into account ionizations from excited levels and neglects effects of self-absorption, we circumvent this problem by introducing the normalization coefficient K in the equation (2.22). We take into account that for frequencies lower than the critical value $\nu_{\text{cr}} \simeq 5.3 \cdot 10^8 \sqrt{T_e^{-1.35} N_e^2 \Delta R}$ (ΔR being path in plasma, in cm), the optical depth of medium is larger than one and we are dealing with a thermal spectrum whose intensity declines with ν^2 (see [36] for details).

Thus, we find the value of K from considerations of energy conservation, *i.e.* we presume the frequency integrated flux (2.22) to be equal to the incident flux from the illuminating star (taking into account that for $\nu \geq \nu_{\text{cr}}$, the intensity of recombination radiation falls off exponentially

with frequency, for $\nu \leq \nu_{\text{cr}}$ the fall is proportional to ν^2).

We have found from computations that K is of order $1.5 \div 3$, which points to credibility of our approximate method. Besides, values of K influence only the value of J_{rec} , it obviously does not effect solutions to the equilibrium equations (2.9), (2.11), (2.17). The value of K serves as internal check of consistency of our solutions.

2.6 Technical details

- (i) The set of equilibrium equations (2.9), (2.11), (2.17) is solved numerically. We start from the top of the atmosphere, where $\tau \equiv 0$, and found at this point the boundary value of the equilibrium temperature $T_{\text{eq}}(r = 0)$ and ionization degree. Introducing a small geometric depth increment Δr and calculating the corresponding increment of optical depth as $\Delta\tau = \int_0^{\Delta r} N_0 \kappa_\nu dr$, we find new sets of $T(r + \Delta r)$ and $X(r + \Delta r)$ as well as $N_e(r + \Delta r)$, $N_0(r + \Delta r)$ and $P(r + \Delta r)$ by numerical integration of the equilibrium equations. This procedure is followed until ionization degree falls below a critical value of $X < 0.02$. We take this depth as limiting value of the upper atmosphere extension R_{lim} , neglecting minor residual L_c flux and ionization.
- (ii) Since parameters of the upper atmosphere demonstrate very non-linear dependence of the geometric depth r , we were obliged to adjust automatically the step Δr in order to accomplish computations more effectively. In general, Δr grows gradually with depth; however, a mechanism of automatic Δr reduction is also provided in case of necessity with the aim retain precision if, due to excessively long step, the equilibrium temperature $T_{\text{eq}}(r)$ experiences excessive growth.
- (iii) In the equations (2.9), (2.11) and (2.20) the upper integration limit of infinity is substituted by a finite numerical value that is chosen, in order to provide better accuracy, in dependence on the hot star effective temperature $T_{1\text{eff}}$. The corresponding wavelength $\lambda_0 \equiv c/\nu_0$ (c is the speed of light) is

$$\lambda_0 = \begin{cases} 200 \text{ \AA}, & \text{if } T_{1\text{eff}} < 50\,000 \text{ K} \\ 10^7 / T_{1\text{eff}} \text{ \AA}, & \text{otherwise.} \end{cases}$$

- (iv) In the expression of the Gaunt factor for bound-free transitions (2.15) we set the upper limit of the second two sums as $n_{\text{up}} \equiv 15$ instead of infinity, and used g'_{100} value instead of g'_{∞} . We use value of $\nu_{\text{crit}} =$

$62.7 \cdot \nu_p$ in the expression (2.16) as criterium for transition from the upper frequency range to the lower range.

2.7 Model analysis and results

2.7.1 Estimation of the role of collisional transitions and radiative ionizations from the second level

To estimate a possible contribution from collisions, the results of model calculations for irradiated B type stellar atmospheres from [33] and [34] were used, which include detailed calculations for populations of atomic levels for 10-level H atom with both free-free and bound-free transitions, with radiative and collisional excitations and de-excitations, in the temperature range of $(10\,000 \div 20\,000)$ K. Numerical data from these models indicate that for column mass of order $dm \sim 10^{-2}$ g/cm⁻² and higher, the role of collisional transitions is comparable to that of radiative transitions. For $dm \sim (10^{-4} \div 10^{-3})$ g/cm⁻², calculations indicate that the total contribution from radiative transitions exceeds that of all collisional transitions by a factor of $4 \div 10$. This result is illustrated by the Table 2.1.

Table 2.1 Ratio R_{cr} of total collisional to radiative rates, $T_{eff} = 10\,350$ K, $\log g = 4.12$

$\log dm$	$N_e, 10^{13}$ cm	R_{cr}
-6.00	0.012	0.048
-5.55	0.033	0.044
-5.10	0.095	0.033
-4.66	0.267	0.026
-4.21	0.747	0.027
-3.76	2.09	0.064
-3.31	6.04	0.220
-3.09	10.2	0.447
-2.87	16.4	1.01
-2.42	45.9	4.08
-1.97	128	10.6

In the Table (2.1), the tabulated values of N_e are the average number densities of electrons normalized to a column $\Delta R = 10^7$ cm height (for different values of ΔR , the values of N_e must be scaled respectively; the value $\Delta R = 10^7$ cm corresponds to a characteristic scale height in the atmosphere with $T = 5000$ K and $\log g = 4$). The results in the Table (2.1) are also in good qualitative agreement with the estimates in [41] (see there

the Table 5.1).

In our model, the incoming L_c flux is absorbed inside a range of column mass of $dm \simeq (10^{-5} \div 10^{-3}) \text{ g/cm}^{-2}$. One can see from the data of the Table (2.1) that for $dm \simeq 10^{-4} \text{ g/cm}^{-2}$, or $N_e \simeq 10^{13} \text{ cm}^{-3}$, the contribution from collisions is small compared with the role of radiative transitions.

We also realized independent evaluations of radiative to collisional transitions ratio basing on the numerical results of our model and using estimating formulae from [41]. The radiative transitions rate may be found as

$$R_0 \simeq 1.3 \cdot 10^{66} W_\delta \int_{\nu_0}^{\infty} \frac{B_\nu(T)}{\nu^4} d\nu \quad (2.23)$$

and the collisional transitions rate as

$$C \simeq 8.5 \cdot 10^{-5} \frac{N_e}{T_e^{1/2}} E_2(157\,000/T_e), \quad (2.24)$$

E_2 being the second exponential integral. Values of R_0/C ratio are presented in the Table (2.2) where they are calculated as function of geometric depth for a model with the following parameters: $R_1 = 0.224 R_\odot$, $R_2 = 0.569 R_\odot$, $A = 2.723 R_\odot$, $M_1 = 0.50 M_\odot$, $M_2 = 0.15 M_\odot$, $T_{1\text{eff}} = 60\,000 \text{ K}$ (the substellar point is considered). It is clearly seen from the Table (2.2) that the ratio R_0/C , being extremely high in the uppermost layers, drops inwards, but significantly exceeds unity through the whole upper atmosphere. In the deepest layers it even grows again, due to dramatic decrease in free electrons concentration.

To compare radiative ionizations rate from the ground level with the same rate from the second level, we used the expression (2.23); to find second-level ionization rate, we took the value of $\nu_1 = \nu_0/4 \simeq 8.2 \cdot 10^{15} \text{ Hz}$ (Balmer jump) for the lower integration limit. Saha ionization equation (2.19) was used to estimate N_1/N_0 ratio, with two alternative temperatures: our ionization temperature estimate T_{ion} and $T_{\text{lim}} = 80\,000 \text{ K}$ as the upper limit for a possible atomic temperature. The respective estimations of R_0/R_1 are given in the last column of the Table (2.2) (in the form X/Y , where X corresponds to R_0/R_1 estimation made with use of the ionization temperature T_{ion} and Y refers to the limiting temperature T_{lim}).

Basing on the Table (2.2) results, one may conclude that radiative ionizations largely predominate collisions through the whole extent of the upper atmosphere layer. The same is true also in respect of ground level radiative ionizations to the second level radiative ionizations ratio; although in the deepest very thin portion of this layer radiative transitions from the second level prevail, in the predominant part of the upper atmosphere

Table 2.2 Ground-level radiative ionizations to collisional transitions rate R_0/C and ground-level radiative ionizations to second-level radiative ionizations rate R_0/R_1 as functions of geometric depth in the atmosphere.

r , 10^6 cm	N_e , 10^{12} cm $^{-3}$	τ	T_{eq} , 10^3 K	T_{el} , 10^5 K	T_{ion} , 10^3 K	R_0/C	R_0/R_1
0.0	5.0	0.0	35,4	0.2	17	$2.1 \cdot 10^9$	230 / 370
2.0	6.4	0.0	27,8	0.4	17	$6.1 \cdot 10^6$	120 / 200
5.0	7.6	0.0	23,6	0.6	16	$4.0 \cdot 10^5$	71 / 110
11.0	9.1	0.0	20,2	0.8	16	$4.8 \cdot 10^4$	37 / 58
39.0	12.9	0.0	16,2	1.2	16	$2.0 \cdot 10^3$	12 / 19
103	20.0	0.0	14,3	1.5	16	$2.4 \cdot 10^2$	7.3 / 11
251	43.7	2.0	13,8	7.0	11	$3.9 \cdot 10^1$	20 / 18
254	51.0	5.5	13,1	10.2	10	$1.8 \cdot 10^1$	19 / 14
255	43.7	19.9	12,0	14.8	8.0	$6.7 \cdot 10^0$	13 / 5
255	15.5	38.3	11,0	17.4	7.0	$5.4 \cdot 10^0$	3.2 / 0.7
255	9.9	47.0	10,7	18.1	7.0	$5.5 \cdot 10^0$	1.5 / 0.3

ionizations from the ground level greatly exceed those from the second level. So, the approach developed in the Section 2.3 is proved to be well-founded.

2.7.2 Conditions in ionized medium

Solution of the set of equations (2.9), (2.11), (2.17) proves to be rather sensitive to a specific form of the function describing the contribution from diffuse radiation. To give graphic illustration to the results given in this Section, the model calculations with the following parameters are used:

$$\begin{aligned} R_1 &= 0.224 R_\odot, \quad R_2 = 0.569 R_\odot, \quad R_{\text{sep}} = 2.723 R_\odot, \\ M_1 &= 0.5 M_\odot, \quad M_2 = 0.15 M_\odot. \end{aligned} \quad (2.25)$$

The effective temperature of the secondary was set to $T_{2\text{eff}} = 4 \cdot 10^3$ K. These parameters are pretty close to the orbital and physical parameters of the well-known PCB V477 Lyr (see the Section 6.2). The total particle density at the top of the atmosphere was allowed to vary in the range between $N_0 = (5 \cdot 10^{11} \div 5 \cdot 10^{13})$ cm $^{-3}$. Solutions for the equations could be also found beyond this range, but for $N_0 \leq 10^{11}$ cm $^{-3}$ the Lyman continuum cannot be absorbed for any reasonable value of thickness of the irradiated atmosphere. For very high electronic densities, the role of the collisions cannot be ignored.

In qualitative terms, one of the basic computational results is that UV radiation penetrates into the upper atmosphere until a certain depth, while the ionization degree remains close to unity and T_{eq} is declining

(that means existence of temperature inversion; see also the Table (2.3) where the variations of the physical parameters T_{eq} , N_e , X , T_{ion} , T_e are represented as functions of the geometrical and the mean optical depths for $T_{1\text{eff}} = 60\,000$ K, the substellar point being considered). Thereafter almost all of the flux is absorbed in a very thin layer of practically neutral hydrogen. This is illustrated by the Figure (3) where the equilibrium temperature $T_{\text{eq}}(r)$ is represented for different angular distances from the substellar point. The figure demonstrates that T_{eq} distribution experiences a steep decline at the top of the atmosphere, where self-absorption at the left-hand-side of the equations (2.9) and (2.11) in UV becomes important. Thereupon temperature gradient remains rather low until one reaches the regions where the ionization changes dramatically. The relatively slow change of the equilibrium temperature in the intermediate layers can be interpreted as effective cooling of the atmosphere by radiation in recombinations and by effectiveness of loss of far UV quanta on ionization of H . As it may be expected, the penetration depth depends on δ , closely to the substellar point radiation penetrates into the layer deeper than near the limb.

The noticeable fact that may be drawn from the Figure (3) is that T_{eq} values at the boundary of the atmosphere are essentially independent of the angular distance from the substellar point, thus T_{eq} is mainly defined by the energy distribution of the irradiating flux rather than by its intensity. For the same reason, the equilibrium temperature distribution is insensitive to the size of the orbit; this fact is illustrated by the Figure (4); notice that the profile of T_{eq} remains the same but the emission measure rapidly diminishes with increasing of the separation.

In the Figure (5) the dependence of equilibrium temperature $T_{\text{eq}}(r)$ behavior on the primary effective temperature $T_{1\text{eff}}$ is represented. The Figure (6) illustrates ionization degree $X(r)$ behavior in the upper layer. It is seen that the ionization remains very high ($X > 1 - 10^{-2}$) until the same depths where $T_{\text{eq}}(r)$ fall accelerates, and thereafter it drops abruptly. Notice that the column depth, where the Lyman continuum radiation is completely absorbed, rapidly decreases from the substellar point to the limb.

Both the number density of electrons N_e (see the Figure (7)) and the mean optical depth $\bar{\tau}$ (see the Figure (8)) in the Lyman continuum gradually increase with growing depth in the irradiated atmosphere. When $\bar{\tau}$ exceeds a value of $(1 \div 3)$, N_e experiences steep rise while the ionization degree rapidly declines. As it may be expected, monochromatic optical depths τ_λ in the Lyman continuum depend strongly on wavelength; this is illustrated by the Figure (9). When the ionization degree $X \simeq 0.5$ is reached, the electron density declines rapidly. It is clear from the Fig-

ures (6), (7) and (8) that the thickness of the boundary layer between the *HII* zone and the photosphere is small, similar to the case of classical Strömgen spheres. Obviously, in the layer of the irradiated atmosphere where N_e is relatively high (the area corresponding to the plateau of the T_{eq} run in the Figure (5)), cooling is the most efficient and the contribution from the recombined radiation is maximal. Values of T_{eq} here are within the range of $\simeq (12\,000 \div 15\,000)$ K and they are insensitive to the effective temperature of the irradiating star.

The uppermost layers of the irradiated atmosphere are severely overheated. This is illustrated well by the Figure (10), where the run of equilibrium temperature T_{eq} for parameters typical for PCBs is compared with that of the ionization temperature T_{ion} , based on the Saha relation for our model electron and neutral *H* number densities and the bolometric temperature T_{bol} of the impinging flux (corresponding to the given primary effective temperature T_{leff} and the dilution factor W_δ). Notice that only for deep layers, $r > 2.5 \cdot 10^8$ cm, one has $T_{\text{eq}} \simeq T_{\text{ion}} \simeq T_{\text{bol}}$. The temperature inversion in the uppermost regions of the irradiated atmosphere is caused by a specific dependence of the adopted cooling function (see the equations (2.12) – (2.16) and the Figure (11)) on temperature and density in these atmospheric layers (for a detailed discussion see [4]). This is illustrated by the Figure (12), where the cooling coefficient maximum temperature profile T_{unst} is displayed over the extent of the atmosphere. T_{unst} is found numerically from the condition $\frac{d}{dT}q(T) = 0$. It is seen from the Figure (12) that up to $r \sim 2.8 \cdot 10^8$ cm, T_{eq} remains higher than T_{unst} , pointing to the presence of thermal instability conditions in this region. This is due to the fact that with increasing temperature and decreasing density in the uppermost regions of irradiated atmosphere, the recombination rate rapidly declines as $N_e^2 T^{-1/2}$, whereas the rate of photoionizations is superimposed by strength of the incident flux and the number of *H* atoms at the ground level. Below the point $T_{\text{eq}} = T_{\text{unst}}$, medium becomes stable, ionization drops quickly and thermalization is installed. Temperature inversion is a well-known effect in irradiated atmospheres, and its presence is pointed out in many works (see for instance [10], [27], [35]).

A quantitative comparison between the incoming flux from the hot primary at the upper boundary of the irradiated atmosphere and the recombinational radiation in bound-free and free-free transitions, integrated over wavelength and the column of gas where the Lyman continuum is effectively absorbed, indicates that in deep layers where the mean optical depth in L_c is $\bar{\tau} \sim 5 \div 10$, roughly only $25 \div 50$ per cent of the incoming flux is used for ionization of *H* with subsequent recombinations. The remaining portion is expended on heating of the electron gas and in other forms (see the last column of the Table (2.3) where the ratio of energy $\Delta E(r)$

of the irradiating source spent on ionization of H to that lost on heating of electron gas is tabulated). Value of $\Delta E(r)$ are sensitive to the electron density, and $T_e(r)$ rises steeply with increasing the depth r . This is explained by the interplay of two factors: by the rapid increase of the number of neutral H atoms with r on one hand and on the other hand, by a specific dependence of the absorption coefficient on frequency, resulting in penetration of photons of higher energy into progressively deeper layers. The effect is amplified by the fact that the collisional cooling rate decreases with increasing r at a rate that is roughly proportional to $T_e(r)^{-1/2}$. Since collisional excitations are not taken into account in our model, and in view of uncertainties in the source function at large optical depths, we regard the values of $T_e(r)$ as reliable estimates only for $\bar{\tau} \leq (0.1 \div 0.2)$ in the Lyman continuum.

The thermal timescale for the layer where the Lyman flux is effectively absorbed is comparable to the orbital period of a typical PCB (for $dm \sim 10^{-3}$ g/cm $^{-2}$ and the effective thickness of the layer 10^7 cm). A similar value is obtained assuming that T_{eq} is the equilibrium temperature of neutral H , T_e is the electron gas temperature and estimating the cooling timescale as

$$t_{th} \simeq 1.8 \cdot 10^{11} N_e^{-1} T_e^{-1/2} \text{ sec} \quad (2.26)$$

from the Spitzer equation for the exchange of energy between neutral H atoms and free electrons (see the formulae 3.267, 3.268 in [36]). For typical values of $T_e \sim 10^5$ K and $N_e \sim 10^{12}$ cm $^{-3}$ we find $t_{th} \sim 10^4$ s. A possible relation between onset of thermal instability and pulsations may be a topic of a separate study. It is worth mentioning that Maxted *et al.* found in the binary system WD 0710+741 (hot sdw and M-type dwarf) evidence of H_α phase-dependent emission with an intensity hundreds of times higher than predicted by photoionisation by a normal sWD (see [38]). To explain this discrepancy, they suggest accretion of material from the wind of the M-type companion. As we see, the results of our model calculations suggest that transient effects on a timescale comparable to orbital periods of typical PCBs are anticipated.

Although thermal instability was found to arise in the outer atmosphere layer, our model does not take it directly into account. However, this approach is well-founded in the first approximation due to the following reasons. a) Observations of eclipsing PCBs do not show any noticeable fluctuations of the radius of the secondary component, and this fact puts limit on the amplitude of effects that thermal instability may induce. b) According to the estimation by the equation (2.26), the timescale of thermal instability is long enough not to cause rapid oscillations in the atmosphere, so the process of radiation transfer may be considered as nearly stationary.

c) Values of the coefficient K in (2.22) confirm that recombinational cooling mechanism provides reprocessing of significant amount of impinging flux energy, thus the energy portion expended on non-stationary processes is of secondary importance. However, a possible influence of thermal instability on physical conditions in the atmosphere may be a subject of an independent study. The above-mentioned phase-dependent features in spectra may be an indicator of such instability.

The Figure (13) represents the recombination spectrum of emerging radiation calculated by the expression (2.22). Lyman, Balmer and Paschen jumps are distinctive.

Table 2.3 Upper atmosphere model for $T_{\text{eff}} = 60\,000$ K, sub-stellar point. Designations are explained in the Section 2.7.2.

r , 10^6 cm	T_{eq} , 10^3 K	N_e , 10^{12} cm $^{-3}$	$\bar{\tau}$	X	T_{el} , 10^5 K	T_{ion} , 10^3 K	ΔE
0.0	35.4	5.0	0.0	1.000	0.2	1.70	0.32
0.5	32.7	5.4	0.0	1.000	0.3	1.70	0.32
1.0	30.7	5.8	0.0	1.000	0.3	1.70	0.32
1.5	29.1	6.1	0.0	1.000	0.4	1.70	0.32
2.0	27.8	6.4	0.0	1.000	0.4	1.70	0.32
2.5	26.7	6.7	0.0	1.000	0.5	1.70	0.32
3.0	25.9	6.9	0.0	1.000	0.5	1.70	0.32
3.5	24.9	7.2	0.0	1.000	0.5	1.60	0.32
4.0	24.5	7.3	0.0	1.000	0.6	1.60	0.32
5.0	23.6	7.6	0.0	1.000	0.6	1.60	0.32
6.0	22.3	8.1	0.0	1.000	0.7	1.60	0.32
7.0	21.8	8.3	0.0	1.000	0.7	1.60	0.32
9.0	20.7	8.8	0.0	1.000	0.8	1.60	0.32
11.0	20.2	9.1	0.0	1.000	0.8	1.60	0.32
15.0	18.8	9.9	0.0	1.000	0.9	1.60	0.32
19.0	18.1	10.5	0.0	1.000	1.0	1.60	0.32
23.0	17.7	10.9	0.0	1.000	1.0	1.60	0.32
31.0	16.7	12.0	0.0	1.000	1.1	1.60	0.32
39.0	16.2	12.9	0.0	1.000	1.2	1.60	0.32
55.0	15.3	14.7	0.0	1.000	1.3	1.60	0.32
71.0	14.9	16.4	0.0	1.000	1.4	1.60	0.33
103	14.3	20.0	0.0	1.000	1.5	1.60	0.34
135	14.4	23.2	0.1	1.000	1.7	1.50	0.37
167	14.5	26.6	0.1	1.000	2.0	1.50	0.41
183	14.5	28.6	0.2	1.000	2.2	1.50	0.44
199	14.6	30.4	0.3	1.000	2.6	1.40	0.49
215	14.6	32.6	0.4	1.000	3.1	1.40	0.57
223	14.6	33.9	0.5	1.000	3.4	1.40	0.63
231	14.5	35.5	0.6	0.999	3.9	1.30	0.71
239	14.4	37.4	0.8	0.999	4.6	1.30	0.84
243	14.3	38.9	1.0	0.998	5.2	1.30	0.93
245	14.2	39.8	1.1	0.998	5.5	1.20	0.99
249	14.0	42.0	1.5	0.996	6.4	1.20	1.16
251	13.8	43.7	2.0	0.992	7.0	1.10	1.29
253	13.5	46.4	3.0	0.979	8.3	1.10	1.56
253	13.4	47.1	3.3	0.974	8.5	1.10	1.60
254	13.3	48.5	3.9	0.958	9.1	1.00	1.73
254	13.1	51.0	5.5	0.900	10.2	1.00	1.96
254	12.8	54.5	7.9	0.749	11.4	0.90	2.24
255	12.6	57.2	10.0	0.570	12.2	0.90	2.43
255	12.3	54.7	14.7	0.277	13.6	0.80	2.76
255	12.2	50.7	16.8	0.200	14.1	0.80	2.88
255	12.0	43.7	19.9	0.134	14.8	0.80	3.02
255	11.7	34.5	24.0	0.083	15.6	0.80	3.19
255	11.4	23.0	31.1	0.042	16.6	0.70	3.39
255	11.2	19.0	34.5	0.032	17.0	0.70	3.47
255	11.0	15.5	38.3	0.024	17.4	0.70	3.54
255	10.9	12.5	42.4	0.018	17.8	0.70	3.60
255	10.7	9.9	47.0	0.013	18.1	0.70	3.65

Chapter 3

Model for the inner layer

3.1 Incident flux

It was demonstrated (see the Section 2.7.2) that a predominant part of the incident flux in the Lyman continuum is absorbed in the upper layer, which simultaneously turns to be transparent for less energetic photons. The L_c flux absorbed in the upper layer is reprocessed, so that high energy L_c quanta are re-emitted as UV and optical quanta; a certain portion of them leaves the atmosphere, the rest is emitted inwards.

Consequently, there are two sources of radiation that falls onto the boundary of the inner layer: (a) photons from the hot primary with $\lambda > 912 \text{ \AA}$; and (b) reprocessed radiation from the outer layer, *i.e.* the product photons from the reprocessed Lyman continuum. Since the primary is considered to be an absolutely black body radiator, the input of the first source is expressed through the Planck function with due account of dilution. The input of the second source is expressed through the equation for intensity of the reprocessed radiation (2.22).

At the same time we should take into account limb-darkening of the hot star u_1 . Thus the net monochromatic flux incident upon the inner layers is expressed as follows:

$$J_{\text{inc}}(\nu) = \frac{1}{1 - u_1/3} [\pi W_\delta B_\nu(T_{\text{1eff}}) + J_{\text{rec}}(\nu)], \quad (3.1)$$

W_δ being the dilution coefficient (2.1), $B_\nu(T_{\text{1eff}})$ being the Planck function (A.19) and T_{1eff} being the effective temperature of the primary star.

The bolometric flux incident upon the inner layers is obtained by integration of the sum (3.1):

$$F_{\text{inc}} = \int_0^\infty J_{\text{inc}}(\nu) d\nu. \quad (3.2)$$

3.2 Eddington approximation

For the inner layer (with the mean optical depth $\bar{\tau} \geq 2/3$), the Eddington approximation may be used as it stands for a plane-parallel atmosphere:

$$F_0 + F_{\text{inc}}(r) = -\frac{16}{3} \frac{\sigma T^3(r)}{\bar{\kappa}} \frac{dT}{dr}. \quad (3.3)$$

Here $F_0 = \sigma T_{2\text{eff}}^4$ is the proper bolometric flux of the secondary component, $\bar{\kappa}$ is the mean absorption coefficient (see the Section A.4 for details). This equation enables one to find the temperature distribution as a geometric depth function $T = T(r)$ within the deeper layers.

We use the Eddington approximation to build the model of this layer. The upper boundary of is explicitly set $\bar{\tau} = 2/3$. The upper and the inner atmosphere models are laced by the boundary conditions of the temperature $T_{\text{bound}}^4 = W_\delta T_{1\text{eff}}^4 + \frac{F_{\text{inc}}(0)}{\sigma}$ and the pressure $P_{\text{bound}} = N_{\text{bound}} k T_{\text{bound}}$, N_{bound} being the net particle concentration at the bottom of the upper layer.

To solve the equation (3.3), we follow the method proposed by Basko and Sunyaev, see [4]. We introduce a new variable y defined as follows:

$$y(r) = \frac{x_H}{m_p} \int_0^r \rho(r) dr, \quad (3.4)$$

where m_p is the mass of the proton, $x_H = A_H / \sum_j A_j$ is the number of hydrogen nuclei per nucleon (see (A.11) for A_j) and $\rho(r) = \sum_j N_j m_j$ is the local density, m_j being the mass of the nucleon for an element j .

In terms of y , (3.3) becomes

$$F_0 + F_{\text{inc}}(y) = \frac{16}{3} \frac{\sigma T^3(r)}{\bar{\kappa}} \frac{dT}{dy}. \quad (3.5)$$

We will need values of the pressure and of the incident flux in the layer as functions of y . The expression for the pressure may be obtained from the equation of hydrostatic equilibrium

$$\frac{d}{dr} P(r) = G_\delta \rho(r). \quad (3.6)$$

(for the net gravitational acceleration G_δ , see the Section 2.2).

In the terms of y , this equation may be given a form

$$P(y) = G_\delta \frac{m_p}{x_H} y + P_0, \quad (3.7)$$

P_0 being the gas pressure at the boundary (*i.e.* at $\tau = 2/3$).

The incident flux dependence on y is given by the following integral:

$$F_{\text{inc}}(y) = \exp\left(-\frac{2}{3\mu}\right) \int_0^\infty J_{\text{inc}}(\nu) e^{-N\kappa_\nu y} d\nu, \quad (3.8)$$

$\mu = \cos \alpha$ being the cosine of the angle α between the local normal and the incident flux direction (see (2.2), the second equation), κ_ν being the

monochromatic absorption coefficient (see the Section A.3 for details), $N = kT/P$ being the net particle concentration. The term $\exp(-2/3\mu)$ takes into account the fall of the incident flux in the upper layer.

The equation (3.5) is integrated numerically step by step (see technical details in the Section 3.4). The geometrical depth scale

$$r(y) = \frac{m_p}{x_H} \int_0^y \frac{dy}{\sum_j N_j m_j} \quad (3.9)$$

and the mean optical depth scale

$$\bar{\tau}(r) = \frac{2}{3} + \int_0^r \bar{\kappa}(r) dr \quad (3.10)$$

are also introduced (we use the fact that differentiating of (3.4) gives $dr = \frac{m_p}{x_H} \frac{dy}{\rho}$).

3.3 Emergent radiation intensity and spectrum

Monochromatic radiation intensities of the radiation emergent from the layer may be found as

$$I_\nu(\mu) = \int_0^\infty \frac{1}{\mu} B_\nu(T) \exp\left(-\frac{\tau_\nu}{\mu}\right) d\tau_\nu, \quad (3.11)$$

$B_\nu(T)$ being the Planck function, $\mu_0 = \cos \alpha$ being the cosine of the angle α between the local normal and the incident flux direction and τ_ν being the monochromatic optical depth,

$$\tau_\nu(r) = \int_r^\infty \kappa_\nu d\nu. \quad (3.12)$$

However, since monochromatic depth scales are unknown, we should use the mean optical depth scale (supposing validity of LTE over the layer):

$$I_\nu(\mu) = \int_0^\infty \frac{\kappa_{2/3}(\nu)}{\bar{\kappa}_{2/3}} \frac{1}{\mu} B_\nu(T) \exp\left(-\frac{\kappa_{2/3}(\nu)}{\bar{\kappa}_{2/3}} \frac{\tau}{\mu}\right) d\tau, \quad (3.13)$$

where $\kappa_{2/3}(\nu)$ and $\bar{\kappa}_{2/3}$ are respectively the monochromatic and the mean absorption coefficients at the mean optical depth $\tau = 2/3$.

Obtained intensities of the radiation emergent from the deeper atmospheric layer, together with intensities emerging from the upper layer by (2.22), are used in calculations of the luminosity of the secondary's disc.

3.4 Technical details

- (i) The mean absorption coefficients $\bar{\kappa}$ were tabulated with due precision as functions of temperature in order to avoid their calculation in every step and to save computational time. Two specific methods of averaging were used: the Planckian mean and the Rosseland mean (see the Section A.4 for details). One may choose either of them in order to build a model atmosphere.
- (ii) Integration limits in (3.5) and (3.8) are chosen to correspond the range of wavelengths $\lambda = (200 \div 750\,000) \text{ \AA}$.
- (iii) The process of integration begins at the upper boundary $y = 0$, $\bar{\tau} = 2/3$. At each step, a small increment ΔT is assigned and the corresponding Δy increment is found numerically from (3.5) together with the geometrical depth increment $\Delta r = \frac{m_p \Delta y}{x_H \rho}$ and the mean optical depth increment $\Delta \bar{\tau} = \bar{\kappa} \Delta r$, as well as the pressure increment $\Delta P = G_\delta \frac{m_p}{x_H} \Delta y$. Thereafter the model is extended further into the atmosphere: $T_{i+1} = T_i + \Delta T$, $y_{i+1} = y_i + \Delta y$, $r_{i+1} = r_i + \Delta r$, $\bar{\tau}_{i+1} = \bar{\tau}_i + \Delta \bar{\tau}$, $P_{i+1} = P_i + \Delta P$. Thus a model of the whole inner atmosphere is obtained, *i.e.* parameters of the atmosphere (temperature, pressure, concentration, absorption factor) are found as functions of r and $\bar{\tau}$. The process of numerical solution is stopped when the mean optical depth exceeds the value of $\bar{\tau} = 14$, since radiation proceeding from deeper layers is negligible.
- (iv) In order to provide higher precision, values of ΔT increment vary linearly with the angular distance from the substellar point δ : at $\delta = 0^\circ$ we set $\Delta T = 70 \text{ K}$, near the limb $\delta = 90^\circ$ it is decreased to $\Delta T = 30 \text{ K}$.
- (v) The integration upper limit in (3.13) is taken such that the argument of the exponent function were $-\frac{\kappa_{2/3}(\nu)}{\bar{\kappa}_{2/3}} \frac{\tau}{\mu} = -14$. If the corresponding τ is larger than the limiting mean optical depth obtained in the solution of (3.5), we apply extrapolation to get the value of temperature at the corresponding point in the layer.
- (vi) Since computations of intensities by (3.13) are time-consuming, we tabulate these intensities as functions of distance from the substellar point δ and of angle with the local normal $\alpha = (0^\circ \div 89^\circ)$; in the process of tabulation, values of recombinational radiation intensities (2.22) are simultaneously added. The tabulation step over δ depends on the number of zones into which the illuminated hemisphere is divided (see the Section 4.1 for details), the step of α is 1° .

Chapter 4

The luminosity of the system

4.1 Secondary star luminosity

To calculate the luminosity of the secondary's disc measured by a terrestrial observer, we must integrate intensity of the emergent radiation over the visible portion of the star. Following Napier [46], we divide the stellar surface into circular zones with the common center in the substellar point (see the Figure (1) taken from [46]). The distance of a zone from the substellar point is δ , its width is $\Delta\delta$. The running angle along the zone is χ . In this case, the luminosity of the disc at a chosen wavelength ν is

$$L_2(\nu, i, \theta) = 2R_2^2 \int_{\delta_{\min}}^{\delta_{\max}} \left\{ \int_0^{\chi_{\max}} [J_\nu(\delta, \Psi) + I_\nu(\delta, \Psi)] \cos \Psi d\chi \right\} \sin \delta d\delta. \quad (4.1)$$

i is the orbit inclination angle, θ is the phase angle that defines a position of the star on its orbit ($\theta = 0$ at the minimum light). J_ν and I_ν are respective intensities of the emergent radiation from the upper layer of the atmosphere (recombinational radiation intensity) and from the inner layer. Ψ is the angle between the direction towards the observer and the local normal to the stellar surface,

$$\cos \Psi = \sin \epsilon \sin \delta \cos \chi + \cos \delta \cos \epsilon. \quad (4.2)$$

The angle χ is the running angle along the chosen circular zone. ϵ defines the angular distance from the substellar point to the center of the star,

$$\cos \epsilon = -\cos \theta \sin i. \quad (4.3)$$

The limiting values ($\delta_{\min}, \delta_{\max}, \chi_{\min} \equiv 0, \chi_{\max}$ defines the observable portion of the star. From spherical geometry it may be found that

$$\chi_{\max} = \begin{cases} \pi, & \text{if } \epsilon = \pi \text{ or } |\cot \delta \cot \epsilon| > 1; \\ \arccos(-\cot \delta \cot \epsilon), & \text{otherwise.} \end{cases} \quad (4.4)$$

The condition of visibility of the zone assumes

$$|\epsilon - \delta| < \frac{\pi}{2}. \quad (4.5)$$

If it is not satisfied, the respective zone is invisible. Since the range for the angle δ is $[0 \div \pi]$, the limits δ_{\min} and δ_{\max} for integration over the zones in (4.1) are

$$\begin{cases} \delta_{\min} = 0, & \delta_{\max} = \epsilon + \frac{\pi}{2}, & \text{if } \epsilon \leq \frac{\pi}{2}; \\ \delta_{\min} = \epsilon - \frac{\pi}{2}, & \delta_{\max} = \pi, & \text{otherwise.} \end{cases} \quad (4.6)$$

4.2 Transitions and occultations

4.2.1 Eclipses of the secondary star

When the angle between the orbital plane and the direction to the observer is small enough (*i.e.* the orbital inclination angle i is close to 90°), the hot primary star on its way along the orbit may eclipse partially the disc of the secondary component (or even totally, if the radius of the primary is larger than the radius of the secondary). So, calculating the net luminosity of the system, we should subtract from the total luminosity of the secondary (4.1) luminosities of the eclipsed zones. The condition to be fulfilled so that transitions could take place is

$$\frac{\pi}{2} < \theta < \frac{3\pi}{2}. \quad (4.7)$$

It means that the orbital position of the primary is in front of the secondary. Further we shall concentrate on calculations of L_{eclipse} , that is the luminosity of the eclipsed portion of the secondary's disc.

Let us introduce an angular distance between the centers of the stars at their current orbital position (defined by angles i and θ) as

$$\varrho = \sqrt{1 - \cos^2 \theta \sin^2 i}. \quad (4.8)$$

A transition is possible if

$$\varrho < a_2 + a_1, \quad (4.9)$$

a_1 and a_2 being the radii of the components in units of their separation R_{sep} ; otherwise $L_{\text{eclipse}} = 0$.

If the condition (4.9) is fulfilled, we find L_{eclipse} by integration of the secondary's intensity over the portion of its disc eclipsed by the primary star. For this, we divide the eclipsed portion onto circular zones (closed or open-ended) around the center of the transiting star and realize integration over the zones. First of all, the integration limits are found for integration over the zones. ξ is the zone angle, it depends on relative positions of the stars on their orbits:

$$\xi_{\min} = \begin{cases} 0, & \text{if } \frac{\varrho - a_1}{a_2} \leq 0; \\ \arcsin \frac{\varrho - a_1}{a_2}, & \text{otherwise} \end{cases} \quad (4.10)$$

and

$$\xi_{\max} = \begin{cases} \frac{\pi}{2}, & \text{if } \frac{\varrho + a_1}{a_2} \geq 1; \\ \arcsin \frac{\varrho + a_1}{a_2}, & \text{otherwise.} \end{cases} \quad (4.11)$$

Thereafter the limit Ξ_{\max} for integration along the specific zone ξ is the found (Ξ being the running angle along the zone), it depends on positions of the stars and on the position of the zone:

$$\Xi_{\max} = \begin{cases} \pi, & \text{if } \frac{\varrho^2 + a_2^2 \sin^2 \xi - a_1^2}{2\varrho a_2 \sin \xi} \leq -1; \\ \arccos \frac{\varrho^2 + a_2^2 \sin^2 \xi - a_1^2}{2\varrho a_2 \sin \xi}, & \text{otherwise.} \end{cases} \quad (4.12)$$

The expression for L_{eclipse} is as follows:

$$L_{\text{eclipse}} = \int_{\xi_{\min}}^{\xi_{\max}} \left\{ \int_0^{\Xi_{\max}} [J_{\nu}(\delta, \xi) + I_{\nu}(\delta, \xi)] d\Xi \right\} \sin \xi \cos \xi d\xi. \quad (4.13)$$

J_{ν} and I_{ν} are respective intensities of emerging radiation from the upper layer of the atmosphere (recombinational radiation intensity) and from the inner layer (compare with (4.1)). The first argument δ is the angular distance from the substellar point. It is found as

$$\cos \delta = \cos \epsilon \cos \xi + \sin \epsilon \sin \xi \cos \Xi. \quad (4.14)$$

(see (4.3) for ϵ). The second argument of J_{ν} and I_{ν} in (4.13) is the angle between the direction towards the observer and the local normal; in the present case it is equal to ξ .

When the luminosity of the eclipsed portion of the secondary's disc L_{eclipse} is found, we subtract it from the net luminosity of the disc L_2 and thus obtain the observed luminosity of the secondary L'_2 :

$$L'_2 = L_2 - L_{\text{eclipse}}. \quad (4.15)$$

4.2.2 Eclipses of the primary star

Depending on relative positions of the stars on their orbits, the disc of the hot primary may be fully or partially occulted by the secondary star. Thus we should take into account these possible occultations when computing the total luminosity of the system. The condition to be fulfilled so that occultations could take place is

$$\frac{\pi}{2} > \theta > \frac{3\pi}{2}. \quad (4.16)$$

It means that the orbital position of the primary is behind the secondary (compare with (4.7)).

The angle ϱ is introduced analogously to (4.8). The following situations are possible depending on the relation between the radii of the components a_1 and a_2 (in units of their separation R_{sep}):

$$\left\{ \begin{array}{ll} a_2 - a_1 \geq \varrho & : \text{ total occultation;} \\ a_2 - a_1 < \varrho < a_2 + a_1 & : \text{ partial occultation;} \\ \varrho \geq a_2 + a_1 & : \text{ no occultation.} \end{array} \right. \quad (4.17)$$

(Of course, the condition (4.16) should also be fulfilled in the first two cases). In the first case, the luminosity of the hot star $L_1(\nu)$ at a chosen wavelength ν measured by the observer is zero. In the second and the third cases, the visible hemisphere of the hot star is divided into circular zones (closed or open-ended) around its center, and the luminosity $L_1(\nu)$ is obtained by integration over the zones:

$$L_1(\nu) = 2R_1^2 B_\nu(T_{\text{1eff}}) \int_0^{\frac{\pi}{2}} (1 - u_1 + u_1 \cos \zeta) \Omega(\zeta) \sin \zeta \cos \zeta d\zeta. \quad (4.18)$$

B_ν is the Planck function, ζ is the running angle over zones, u_1 is the limb-darkening coefficient of the primary. $\Omega(\zeta)$ is the angle over the zone opened for the observer. It is found as function of the zone angle ζ and relative positions of the stars:

$$\Omega(\zeta) = \left\{ \begin{array}{ll} \pi, & \text{if } \varrho \geq a_2 + a_1 \\ & \text{or } a_1 \sin \zeta \leq \varrho - a_2 \\ & \text{or } a_1 \sin \zeta \geq \varrho + a_2; \\ 0, & \text{if } a_1 \sin \zeta \leq a_2 - \varrho; \\ \pi - \arccos \left(\frac{\varrho^2 + a_1^2 \sin^2 \zeta - a_2^2}{2\varrho a_1 \sin \zeta} \right) & \text{otherwise.} \end{array} \right. \quad (4.19)$$

The first option corresponds to a fully visible zone, the second option corresponds to a fully invisible zone and the option corresponds to a partially visible zone.

4.3 Light curve construction and normalization

To construct a light curve for a system with given parameters, we should represent its net luminosity as function of the phase angle θ . For

each phase angle, the luminosities of both components should be computed (with due account of possible eclipses) and summed up:

$$L(\nu, \theta) = L_1(\nu, \theta) + L'_2(\nu, \theta). \quad (4.20)$$

The luminosity of the primary component L_1 is a function of θ during occultations (see the Section 4.2.1). L'_2 is the secondary's luminosity with due account of possible transitions (see the Section 4.2.2).

It is usually convenient to normalize the computed light curve, *i.e.* to represent the luminosity in units of some fixed luminosity value (normalization basis). We use for such basis the system's net luminosity at the phase $\theta = 0$, *i.e.* at the minimum light. If occultations should occur in the system, we do not take them account them calculating the normalization basis (by taking for L_1 its value at the phase $\theta = \pi$, where the hot primary is in front of the secondary). So the unit value on the light curve corresponds to purely reflection effect minimum light, and the occultation-induced (primary) minimum lies below the unit value. Thus, the normalized luminosity value L_{normal} at a phase θ is computed as

$$L_{\text{normal}}(\theta) = \frac{L_1(\theta) + L'_2(\theta)}{L_1(\pi) + L_2(0)}. \quad (4.21)$$

4.4 Example spectra of a PCB

Example light curves may be found in the Chapter 6, where models of three specific systems are given, for two systems (UU Sge and V477 Lyr) in V and for the last system (V664 Cas) in UBV .

The Figure (14) represents reflection effect spectra in the maximum light for a system with parameters close to that of V477 Lyr (see the Section 6.2). Luminosities are normalized to the corresponding values in the minimum light according to the equation (4.21). Different effective temperatures of the primary component are taken. In the spectra, Lyman, Balmer, Paschen and Bracket jumps are clearly visible. Heights of the jumps and magnitudes of the reflection effect in general are in strong dependence on the effective temperature of the primary. However, it is seen that growth of the primary effective temperature does not necessarily amplify reflection effect magnitudes at all wavelengths: at some wavelength ranges in optics and UV spectra, which correspond to higher $T_{1\text{eff}}$, lie lower than spectra corresponding to higher $T_{1\text{eff}}$. The reason for that is following. An observer sees not only the irradiated hemisphere of the secondary component (which is lighter for higher effective temperatures of the irradiating star), but both components. So amplitudes of the reflection effect do not directly depend on brightness of the irradiated hemisphere but on relative brightness of

both components, in accordance with the equation (4.21). Thus, for certain wavelengths, T_{1eff} growth may cause more intense growth of brightness of the primary star than that of the radiation reflected by the illuminated hemisphere of the secondary component. In this case amplitudes of the reflection effect will drop at the corresponding wavelengths.

The Figure (15) represents reflection effect spectra of the same system at different orbital phases. Difference between the spectra is prominent. Since in the minimum light the primary is in eclipse, the respective spectrum is nearly pure spectrum of the secondary component with insignificant additive of light reflected from zones close to the limb.

4.5 Technical details

- (i) In numerical integration of (4.1) and (4.13), values for sums of monochromatic intensities $J_\nu + I_\nu$ are interpolated from the corresponding table (see the Section 3.4, last item).

Chapter 5

Algorithm description

The physical model described in the Chapters 2 – 4 was realized numerically as a set of programs written in *Turbo Pascal 7.0*.

The flow block of the program is represented on the Figure (2). The program consists of several units:

- the unit of constants. Contains physical constants and parameters of the modeled system;
- the unit of basic procedures. Contains functions and procedures for mathematical operations (integration, interpolation, solving equations etc.), for memory management, for file and graphical output;
- the unit for computations of absorption coefficients. Contains functions and data necessary to calculate monochromatic absorption coefficients according to the Section A.1;
- the unit to calculate ionization state of matter according to the Section A.2, as well total and mean absorption coefficients according to the Sections A.3 and A.4;
- the unit for computations of the incident flux. Calculates the dilution coefficient (see the Section 2.1) and the impinging outward flux;
- the unit for upper atmosphere model computations. Contains functions and procedures to solve equilibrium equations in the upper atmosphere and to build up the model atmosphere according to the Chapter 2;
- the unit for computations of models of the inner layers. Contains functions and procedures to build up the model atmosphere in the diffuse approximation according to the Chapter 3, as well as to compute and tabulate values of emerging radiation intensity;
- the unit for computations of luminosities and light curves. Contains functions and procedures to compute luminosities of the stars with due account of occultations and transitions, following the Chapter 4, to build up and to normalize light curves of a system;

- input-output unit. Contains calls to start model calculations and to return results.

Input of basic parameters is realized through direct editing of the constants in the program code (*i.e.* the program lacks input interface). Computational results are routed to text files as tables that may be read by many data managing programs, like *Microsoft Excel*, *Gnuplot* etc. The program also contains a simple built-in graphical output interface.

Chapter 6

Applying of the model to observed PCB light curves

6.1 UU Sge

UU Sge is the central eclipsing star of the planetary nebula Abell 43. Hereinafter we follow [49] in description of the history of UU Sge studies.

The variability of the system was discovered by Hoffleit [26]. A relation between UU Sge and Abell 43 was established by Bond [7], and the period of 0.495^d was found in [8], approximate parameters were proposed as $T_1 \sim 35\,000$ K, $M_1 \sim 0.9 M_\odot$, $R_1 \sim 0.4 R_\odot$, (sdO star) and $M_2 \sim 0.7 M_\odot$, $R_2 \sim 0.7 R_\odot$ (dK star), $R_{\text{sep}} \sim 3 R_\odot$. But in absence of radial velocity data, this is only one of a family of possible light curve solutions. Additionally, the light curve of [8] is obviously contaminated by a nearby field star. Spectrophotometry obtained in [73] indicated that the spectrum of the secondary is consistent with a *G7* dwarf, and the primary has a spectral type *O*, the primary temperature $T_1 \sim 45\,000$ K was found from blackbody and model atmosphere fitting in the UV continuum and from Balmer lines.

Pollacco & Bell [49] observed UU Sge with a double-beamed spectrograph (ISIS) on the William Herschel Telescope (WHT) on August 1991. 10 blue-arm and 29 red-arm spectra were obtained. Light curve were also obtained by CCD-photometry on the 1.0-m Jacobus Kapteyn Telescope and GEC CCD in August 1990 with a Johnson *V*-band filter and in April and May 1991 with an *I* filter. The time of the minimum found from *V*-photometry data with the period derived from the least-square analysis are as follows:

$$\begin{aligned} \text{HJD}(\text{Min.I}) = & 2\,448\,133.407\,47 (\pm 0.000\,08) \\ & + 0.465\,069\,102 (\pm 0.000\,000\,016) \text{ E}, \end{aligned} \quad (6.1)$$

which is slightly shorter than quoted by [8] ($0^{\text{d}}.465\,069\,18 \pm 0.000\,000\,06$).

The reflection effect of ~ 0.5 mag was reported in [49]. With the use of *LIGHT2*, an enhanced version of *LIGHT* synthesis code (see [21]), several model light curves were obtained, with the temperature of the primary lying in the range of $35\,000 \text{ K} < T_1 < 145\,000 \text{ K}$. Through non-Keplerian corrections of radial velocities, the mass ratio was estimated as $M_2/M_1 = 0.46$. With the help of *I*-band data in the minimum light, the temperatures of the components were estimated as $T_1 = 117\,000 \pm 12\,000$ K and $T_2 =$

7300 \pm 250 K. Basing on these grounds, the following set of model parameters was discriminated: $M_2/M_1 = 0.29$ (fixed), $R_1 = 0.136 \pm 0.001 R_\odot$, $R_2 = 0.214 \pm 0.001 R_\odot$, $T_{1\text{eff}} = 117500$ K (fixed), $T_{2\text{eff}} = 7315 \pm 30$ K (or $T_{2\text{eff}} = 7336 \pm 87$ K basing on I -band data), $i = 87^\circ.7 \pm 0.1$. From radial velocity curves the masses of the components $M_1 = 0.63 \pm 0.06 M_\odot$ and $M_2 = 0.29 \pm 0.04 M_\odot$ were obtained, with a correction for the reflection effect.

We applied our set of programs to model a V -band light curve of UU Sge basing on the data provided in [49]. The masses of the components were adopted to be $M_1 = 0.63 M_\odot$ and $M_2 = 0.29 M_\odot$ following [49], the semi-major axis value of $R_{\text{sep}} = 2.46 R_\odot$ was found, by the Kepler's third law, from the period and the masses (see for instance the equation (7.29)). The central wavelength in V -band $\lambda = 5550 \text{ \AA}$ was chosen to avoid additional complications with averaging over wavelengths, which would need much more computational time. As a result, two suitable combinations of parameters were found, they are represented in the Table 6.1. References to the corresponding plots, representing each model versus observational light curves, are given in the second column of the table. In all models we used the limb-darkening coefficient of the primary component $u_1 = 2/3$ (see the Section 2.1), the value $N_0 = 10^{13} \text{ cm}^{-3}$ was taken for neutral H concentration on the upper boundary of the atmosphere (see the Section 2.3), the Planckian mean absorption coefficient was adopted for the lower atmosphere model (see the Section 3.2). For chemical composition, we took relative concentration of He to be 0.027 and of metal (K) 0.001.

Table 6.1 UU Sge models

Model nr.	Figure nr.	T_1, K	T_2, K	R_1, R_\odot	R_2, R_\odot	$i, ^\circ$
1	16	85 000	5600	0.359	0.551	88.0
2	17	80 000	5500	0.335	0.551	88.0

6.2 V477 Lyr

V477 Lyr is the central eclipsing star of the planetary nebula Abell 46. Its light curve is similar to UU Sge (see the Section 6.1). A large reflection effect (with amplitude of 0.5 mag) was discovered by Bond [6]. The inclination of the system is relatively low, which makes light curve analysis difficult. A number of solutions was proposed, we cite them following [50].

Bond communicated a solution of an analysis by Twigg, where an orbital inclination of $i = 80^\circ.8$ and a mass ratio of $M_1/M_2 \sim 2.3$ were found. Radii of the components were reported as $R_1 \sim 0.09 R_\odot$ and $R_2 \sim 0.20 R_\odot$ and the primary temperature as $T_1 \sim 105000$ K. Ritter [62] assumed the

mass of the primary component $M_1 = 0.6 M_\odot$, which implies the mass of the secondary component $M_2 \sim 0.25 M_\odot$. The analysis of J.Kaluzny gives the following parameters: $T_1 \sim 60\,000$ K, $R_1 \sim 0.2 R_\odot$ and $R_2 \sim 0.6 R_\odot$, the inclination is not specified. In this solution, the depth of the secondary minimum could only be modeled if the secondary exhibited limb brightening. However, in [50] it is mentioned that the combination of parameters suggested by Ritter [62] cannot produce the observed eclipses, this fact follows from tests by the *LIGHT2* synthesis code (Hill [21]).

It is stressed in [50] that many physical parameters of V477 Lyr and Abell 46 are unknown, the primary temperature being one of the most important of them. In that work, long-slit spectrography is represented, together with a new *V*-band light curve obtained as a result of CCD-photometry on the 1.0-m Jacobus Kapteyn Telescope and GEC CCD in August 1990 with the use of a Johnson *V*-band filter. The authors attempted to model the light curves using *LIGHT2*, an enhanced version of *LIGHT* [21] synthesis code, and got a number of suitable models. From their data, they choose the following set of model parameters: $M_2/M_1 = 0.29$ (fixed), $R_1 = 0.077 \pm 0.002 R_\odot$, $R_2 = 0.203 \pm 0.003 R_\odot$, $T_{1\text{eff}} = 60\,000$ K (fixed), $T_{2\text{eff}} = 5300 \pm 500$ K, $i = 80^\circ.5 \pm 0.2$. From radial velocity curves, the masses of the components of $M_1 = 0.51 \pm 0.07 M_\odot$ and $M_2 = 0.15 \pm 0.02 M_\odot$ were obtained, with a correction for the reflection effect. The time of minimum found from CCD photometry with the period derived from the least-square analysis are as follows:

$$\begin{aligned} \text{HJD}(\text{Min.I}) = & 2\,448\,135.504\,64 (\pm 0.000\,06) \\ & + 0.471\,729\,09 (\pm 0.000\,000\,0050) \text{E.} \end{aligned} \quad (6.2)$$

We applied our set of programs to model *V*-band light curve of V477 Lyr basing on the data provided in [50]. The masses of the components were adopted to be $M_1 = 0.51 M_\odot$ and $M_2 = 0.15 M_\odot$ following [50], the semi-major axis value of $R_{\text{sep}} = 2.72 R_\odot$ was found, by the Kepler's third law, from the period and the masses, and the central wavelength of the *V*-band $\lambda = 5550 \text{ \AA}$ was adopted to avoid additional complications with averaging over the wavelengths. In all models we used the same free parameters and coefficients (chemical composition of the atmosphere of the secondary, limb-darkening coefficient of the primary etc.) as for UU Sge in the Section 6.1. As a result, four suitable combinations of parameters were found, they are represented in the Table 6.2. References to the corresponding plots representing each model versus observational light curves are given in the second column of the table.

As one can see from the computed models, the range of the primary temperatures remains broad, so additional data is needed to constrain parameters of the system. At the same time it should be emphasized that

Table 6.2 V477 Lyr models

Model nr.	Figure nr.	T_1, K	T_2, K	R_1, R_\odot	R_2, R_\odot	$i, ^\circ$
1	18	102 000	4000	0.23	0.64	80.9
2	19	94 000	4000	0.23	0.61	80.3
3	20	87 000	4000	0.23	0.58	79.7
4	21	74 000	4000	0.23	0.55	79.2

since we deal with direct modeling of irradiated atmospheres, our formalism does not involve physically unfounded parameters of the limb brightening x_2 for the irradiated component nor the heating efficiency α , the latter being dependent on T_1 and T_2 values (Pollacco & Bell in [49] assumed $x_2 = -1.0$ and $\alpha_2 = 1.5$ for V477 Lyr).

We inserted our data for UU Sge and V477 Lyr on the WD cooling track by [31], see the Figure 22. The position of the primary for V477 Lyr has shifted significantly. At the present stage it is virtually impossible to discriminate for this object between a *He* core WD and a *CO* core WD, since its new position on the HR diagram lies at the border dividing these two options.

6.3 V664 Cas

V664 Cas was reported as the nucleus of the planetary nebula HFG 1 in [23], and an estimation of the primary temperature $T_1 = 50\,000 \div 60\,000$ K was given. Grauer *et al.* [18] discovered the variability with the amplitude of $\sim 1.1^m$ and with the orbital period of $P_{\text{orb}} = 0.^d5816$. They supposed that V664 Cas belongs PCBs. Basing on low-resolution spectra, Acker & Stenholm [1] classified it as polar, but in the later catalogue [64] it is cited as PCB. So, very little is known about the evolutionary status of this system and its physical parameters.

V664 Cas is a non-eclipsing variable system with a strong reflection effect. Shimanskii *et al.* [71] realized *BVR*-photometry on 0.7-m telescope in the Kourovka in March 2000. Spectroscopic observations were also made on the 6-m BTA telescope with a long-slit spectrograph and 1024×1024 Photometric CCD in August 2001 and in March and August 2002. The time of the minimum and the period were found, on the basis of observations covering an interval of 2360 days, as follows:

$$\begin{aligned} \text{HJD}(\text{Min.I}) = & 2\,451\,623.059\,64 (\pm 0.001) \\ & + 0.581\,647\,5 (\pm 0.000\,002\,2) \text{E}. \end{aligned} \quad (6.3)$$

Amplitudes of the brightness variation were found to be nearly the same in *BVRI*, which indicates that the flux variability is dominated by the

hot spot observed at various projections, so it implies a small orbital inclination. From radial velocities, the mass function of $f = 0.0068 \div 0.0072 M_{\odot}$ was found, being the lowest known among PCBs and implying the secondary mass to exceed the mass of the primary by a factor more than 1.6. To model light curves of the system, a version of the *SPECTR* code was used. The theoretical solution proposed in [71] is as follows: $R_{\text{sep}} = 3.37 \pm 0.06 R_{\odot}$, $M_1 = 0.57 \pm 0.03 M_{\odot}$, $R_1 = 0.19 \pm 0.02 R_{\odot}$, $M_2 = 1.09 \pm 0.07 M_{\odot}$, $R_2 = 1.30 \pm 0.08 R_{\odot}$, $T_1 = 83\,000 \pm 6000$ K, $T_2 = 5400 \pm 500$ K, $i = 28^{\circ} \pm 2^{\circ}$.

Exter *et al.* realized spectrography of V664 Cas at the 4.2-m William Herschel Telescope in December 1994, and also CCD photometry on the 1-m Jacobus Kapteyn Telescope in December 1994 using a Harris *V*- and *I*-band filter. From their analysis, they obtained a period similar to that of [18] and [71]. The radial velocity curve solution provided a number of sets of the system's parameters. The conclusion of [71] about the mass ratio (*i.e.* that $M_2/M_1 \simeq 1.6$) is confirmed as possibility.

We were provided by Shugarov with *UBV* photometry of the system, and we also received *V*-band photometry from Exter. Magnitudes of *V*-band photometry were not provided, so we applied a transformation coefficient to go from instrumental units to stellar magnitudes. The value of this coefficient was found to provide the best agreement with the Shugarov's data. Observational light curves by Shugarov contain considerable asymmetry in all three bands, the reason for that is unknown. This asymmetry is noticeable also in figures given in [71]. Exter's data is more symmetric, although slight non-symmetry is also present. For the sake of demonstration and comparison, we give in the Figure 23 the V664 Cas *V*-band light curve by the Shugarov's data, and in the Figure 24 the *V*-band light curve by Exters's data is represented.

We applied our programs to model *UBV* light curves of V664 Cas basing on the data provided in [71]. The central wavelength of the *UBV*-bands $\lambda_U = 3500$ Å, $\lambda_B = 4350$ Å, $\lambda_V = 5550$ Å were chosen to avoid additional complications with averaging over the wavelengths. In all models we used the same free parameters and coefficients (the chemical composition of the atmosphere of the secondary, the limb-darkening coefficient of the primary etc.) as in the case of UU Sge and V477 Lyr in the Sections 6.1 and 6.2.

Since our models do not take into account ellipticity, the computed models correspond to spherical stars. To provide a first-order account for ellipticity, we used the *Binary Maker* code (<http://www.binarymaker.com>) to calculate independently light curve perturbations by the tidal distortion in an analogous binary system. This perturbation is represented in the Figure 25. The fist-order corrections were introduced to the theoretical models by adding the corresponding value of correction for tidal distortion

to calculated magnitudes.

Table 6.3 V664 Cas models

Model nr.	A	M_1, M_\odot	M_2, M_\odot	T_1, K	T_2, K	R_1, R_\odot	R_2, R_\odot	$i, ^\circ$
1	3.25	0.55	0.80	86 000	5000	0.074	1.23	36
2	3.25	0.55	0.80	83 000	4900	0.065	1.25	38
3	3.25	0.55	0.80	77 000	4900	0.080	1.49	36
4	3.47	0.57	1.09	80 000	4900	0.100	1.68	33

As a result of modeling, four suitable combinations of parameters were found, they are represented in the Table 6.3, the order is from the best to the worst. The Figures 26–29 demonstrate the best of the models, *i.e.* nr. 1, represented versus the observational data. The best fits were found from minimization of the sum of square dispersions. *U*-band models demonstrate the highest deviations of the square sum from the model, but that is due to their proper high dispersion. Exter’s *V*-band data, having the smallest proper dispersion, demonstrates the smallest deviations of the square sum from the model. Although the instrumental coefficient for Exter’s data is unknown, slight shifts of this coefficient from the chosen value do not impair the quality of our fit. During modeling it was found that the fits are not very sensitive to the masses of the components, so satisfactory light curve fits may be obtained in a wide range of the mass-function and radial velocity semi-amplitudes. The residuals of the models and observational data show some structure in all bands (the Figure 30, for instance, represents *U*-band residuals, note opposite-sign trends near the phases 0.25, 0.75 and 1). This may indicate, for instance, influence of the tidal distortion to the hot spot or other phase effects.

Chapter 7

Evolution of progenitors of Extreme Giant Branch objects

7.1 Analysis of mass loss, mass transfer and angular momentum loss

In this section, a method for studying the orbital evolution of progenitors of Extreme Giant Branch objects (EHBs) is described (on the evolutionary status of these objects, see the Section 1.2.3).

To follow the nuclear evolution on the main sequence of the primary component for different initial stellar masses, the computer code package *sse.f* (Swift Stellar Evolutionary Code, see [28]) may be used, until the donor approaches its critical Roche lobe R_L (set by the adopted mass ratio $q = M_1/M_2$ of the components and by the initial value d_0 of the semi-major axis of the orbit).

The Figure (37) represents H–R diagram for a single star. A part of the track with $\log T_{\text{eff}} \simeq 4.2 - 4.4$ corresponds to the EHB sequence position. The final mass of the *He* white dwarf is $M_{1\text{WD}} = 0.50 M_{\odot}$.

Once the donor fills in its critical Roche lobe, the subsequent evolution depends on the relation between R_2 and R_L (the more evolved star *i.e.* the WD is taken to be the primary component and the donor is the secondary component). If, for instance, the donor reacts to the mass loss and the mass transfer by further expanding its envelope, while the radius of the critical Roche lobe decreases, considerable shrinkage of the orbit can be expected even on the dynamical timescale $\delta t \sim 10^4$ yrs. Analytical and numerical analysis is needed to follow the evolution of the system upon the Roche lobe overfilling: factors influencing the mass and the angular momentum loss should be duly accounted in the model.

The following basic assumptions were made: (1) the progenitor of the sdB star filled in its critical Roche lobe when the former was approaching the tip of RGB during its nuclear evolution; (2) until the donor approaches its critical Roche lobe, its evolution does not differ from that of a single star; (3) the angular momentum is carried away from the system partially by the matter leaving the binary through the first Lagrangian point, partially due to matter corotation to the Alfvén radius.

From simple orbital mechanics and the Kepler’s third law, the subsequent change of the period may be linked to the mass loss rate by the equation

$$\frac{\dot{P}}{P} = -2\frac{\dot{M}}{M} + 3\frac{\dot{M}_2(M_1 - M_2)}{M_1 M_2} + 3K, \quad (7.1)$$

where $M = M_1 + M_2$ is the total mass of the system. In derivation of the formula (7.1), the term accounting the spin angular momentum is neglected due to its negligibly low values in respect to the orbital angular momentum. The term K in (7.1) takes into account the additional angular momentum loss from the system by the matter corotated to the Alfvén radius R_A :

$$\dot{J} \equiv KJ = \frac{2}{3} \dot{M} R_A^2 \Omega. \quad (7.2)$$

KJ is the angular momentum loss from the orbital motion with the Keplerian angular velocity Ω . If one sets $R_A = kR_2$, the term K may be given the following form:

$$K = \frac{2}{3} k^2 \left(\frac{R}{d}\right)^2 \frac{M}{M_1 M_2} \dot{M}, \quad (7.3)$$

d being the semi-major axis of the orbit (for detailed derivation of the principle formulae, see [72]).

In the work [68], a different assumption is introduced. It is assumed that the momentum loss rate from the system is described by the relation

$$\frac{\dot{J}}{J} = f \frac{M_1}{M_2} \frac{\dot{M}}{M}, \quad (7.4)$$

f being a free parameter introduced so that the period varies as a unique function of the current masses. Such choice of the free parameter leads to the following relation between f , the period change and the masses:

$$f = \frac{\Delta \log P - \Delta \log M + 3\Delta \log(M_1 M_2)}{3 \left[\frac{\dot{M}}{M_2} \Delta \log M_2 - \Delta \log M \right]}. \quad (7.5)$$

It may be demonstrated that introduction of the coefficient f is equivalent to rewriting the relation (7.1) in the following way:

$$\frac{\dot{P}}{P} = - \left[2 + (1 - f) \frac{M_1}{M_2} \right] \frac{\dot{M}}{M} + 3 \frac{\dot{M}_2(M_1 - M_2)}{M_1 M_2}, \quad (7.6)$$

(considering $K \equiv 0$). Numerical modeling showed that introduction of the coefficient f does not influence fundamentally the model results (if the deviation of latter from unity is not very large), so we do not include the parameter f into our model. The Figure (43) illustrates the evolution of the donor's radius for different values of k with fixed $f \equiv 1$ and for different values of f with fixed $k \equiv 0$. One may see that increment of f is generally equivalent to higher values of k .

Mass loss rate of the donor \dot{M}_2 is defined by the Roche lobe overfilling $\Delta R = R_2 - R_L > 0$ as

$$\dot{M}_2 = \frac{M_2}{t_{HD}} \left(\frac{\Delta R}{R_L} \right)^3, \quad (7.7)$$

$t_{HD} \sim R_2/V_s$ being the hydrodynamical timescale. To avoid t_{HD} calculations that would require knowledge of temperature-dependent sound velocity V_s , it is convenient to introduce the free fall timescale as

$$t_{ff} \simeq R_2/V_{\text{esc}}, \quad (7.8)$$

and, using the fact that the escape velocity $V_{\text{esc}} = \sqrt{R_2/2GM_2}$ is much higher than V_s , it may be set

$$t_{HD} \simeq C \cdot \sqrt{R_2^3/GM_2}, \quad (7.9)$$

C being a constant of about 10^2 . In this way unphysically high mass loss rates are avoided. It follows from such estimations that typically $t_{HD} \sim (10^5 \div 10^6)$ sec, which is roughly one order of magnitude shorter than the thermal timescale of the donor.

The Roche R_L lobe radius is found from the empirical fit of [13],

$$\frac{R_L}{d} = \frac{0.49 q^{2/3}}{0.6 q^{2/3} + \ln(1 + q^{1/3})}. \quad (7.10)$$

The mass accretion rate is set by a predefined value of the mass transfer effectiveness parameter

$$Q = \frac{\dot{M}_2}{\dot{M}} \quad (7.11)$$

($0 \leq Q \leq 1$), that is one of the initial parameters of the model. The increment of the stellar radius, when the star overfills its Roche lobe, is found from the mass-radius-age relation for a single star (which takes into account deviations from the equilibrium radius value due to mass loss) as

$$\Delta \log R_2 = \log \frac{M_2}{M_2^0} - t_{KH} \frac{d \log M_2}{dt}, \quad (7.12)$$

M_2^0 being the stellar mass at the moment of Roche lobe overfilling and

$$t_{KH} = GM_2^2/R_2L_1^0 \quad (7.13)$$

being the Kelvin-Helmholtz (*i.e.* heat diffusion) timescale (L_1^0 is the luminosity at the moment of Roche lobe overfilling). Generally, this relation also should contain a nuclear time-dependent term; but in our specific

case it may be ignored without loss of accuracy due to the fact that the timescale of mass transfer is much shorter comparable to the nuclear evolution timescale.

As it follows from (7.12), a logarithmic dependence exists between the primary radius increment ΔR_2 and the mass loss rate \dot{M}_2 . Due to this fact, joint application of the equations (7.7) and (7.12) may result, for several combinations of parameters, in unphysically rapid growth of the donor's radius combined with a dramatic mass loss. Actually, the extent of overfilling cannot be unlimitedly high: it is always restricted by the slit width between the stellar surface and the Roche lobe. The characteristic dimension of this slit should be estimated through the effective size of the neck near the first Lagrangian point. Following [40], the cross-section S of the neck is represented as

$$S = 2\pi \frac{\gamma RT}{\mu} \frac{1}{p} \frac{d^3}{GM}, \quad (7.14)$$

$\gamma = C_p/C_v$ being the ratio of specific heats, μ being the mean molar mass of the gas, p is a factor following from the Roche lobe geometry. For $R_L \ll d$ this factor may be given the following form:

$$p \simeq \frac{M_2}{M} \left(\frac{d}{R_L} \right)^3. \quad (7.15)$$

Thus the equation (7.14) yields

$$S \simeq 2\pi \frac{\gamma RT}{\mu} \frac{R_L^3}{GM_2}. \quad (7.16)$$

So the linear measure of the neck may be found as

$$\frac{l}{R_L} \simeq \sqrt{8 \frac{\gamma RT}{\mu}} \bigg/ \sqrt{\frac{GM_2}{R_L}} \simeq 3 \frac{V_s}{V_{\text{esc}}}. \quad (7.17)$$

Typical values of l/R_L are $\simeq 30\%$.

Considering this diameter of the neck as chord to the Roche lobe, the height scale H may be estimated from a simple geometry as

$$\frac{H}{R_L} \simeq 1 - \sqrt{1 - \left(\frac{l}{2R_L} \right)^2}. \quad (7.18)$$

From this kind of evaluations, the relative height scale is estimated as $H/R_L \simeq 1\%$. So, the admissible Roche lobe overfilling rates ΔR_2 should be restricted by several percent. Numerical models demonstrate that the evolution of the system is not sensitive, in qualitative terms, to specific choice of the limiting value $\Delta R_{2\text{lim}}$.

7.2 Mass transfer stability conditions

The timescale of the mass transfer depends on the critical Roche lobe reaction to the mass loss by the donor. The mass transfer may occur in the orbital evolutionary timescale or much quicker, in the dynamical either in the thermal timescale.

When the donor loses a fraction of its mass, its hydrostatic and thermal equilibrium conditions are broken. Equilibria are re-established in the dynamical (sound-crossing) and thermal (heat-diffusion) timescales, respectively, and these processes are accompanied with radius changes of the donor. The Roche lobe radius also reacts to the mass loss. The stability of the mass loss is provided so long as the radii of the donor and of its Roche lobe change in the same way; otherwise, the process is unstable and happens in a shorter timescale.

Following [69], the behavior of the quantity

$$\Delta\zeta = \frac{M_2}{\Delta R} \frac{\delta\Delta R}{\delta M_2} \quad (7.19)$$

is important and should be studied in detail. Intrinsically, it is the dimensionless variation of the $\Delta R \equiv R_2 - R_L$ in response to a change in the mass of the donor. The stability conditions of the mass transfer are defined by values of the following exponents in power-law fits $R_2 \sim M_2^\zeta$:

$$\zeta_{\text{ad}} \equiv \left. \frac{\partial \ln R_2}{\partial \ln M_2} \right|_{\text{ad}}, \quad (7.20)$$

$$\zeta_{\text{therm}} \equiv \left. \frac{\partial \ln R_2}{\partial \ln M_2} \right|_{\text{therm}}, \quad (7.21)$$

$$\zeta_{\text{RL}} \equiv \left. \frac{\partial \ln R_2}{\partial \ln M_2} \right|_{\text{RL}}. \quad (7.22)$$

Here ζ_{ad} , ζ_{therm} and ζ_{RL} are the adiabatic mass-radius exponent (for a constant entropy profile), the thermal mass-radius exponent (for a star remaining in the thermal equilibrium state) and the Roche lobe mass-radius exponent (taken along the evolutionary path of the binary). Stability conditions require that the donor remains inside its Roche lobe after the loss of a small amount of its mass, $\delta M_2 < 0$. So the fulfilment of the condition

$$\zeta_{\text{RL}} < (\zeta_{\text{ad}}, \zeta_{\text{therm}}) \quad (7.23)$$

is needed.

For polytropic stars with index n , the adiabatic mass-radius exponent may be found as

$$\zeta_{ad} = \frac{n-1}{n-3} \quad (7.24)$$

(see, for instance, [69]). However, this approximation works only for stars with small core masses. If the core constitutes a noticeable fraction of the total mass of the star, departures from this relation becomes significant. In this case much better results are provided with the help of approximation given by [24]. The star is modeled by a condensed polytrope with a central point mass (far from real near the center of the star, this approximation becomes rather better in the outer layers which are analyzed here). Within this simplification, the adiabatic mass-radius exponent may be fitted (for $n = 3/2$) by the following function with better than 1% accuracy:

$$\zeta_{ad} \simeq \frac{2m}{3(1-m)} - \frac{1-m}{3(1+2m)} - 0.03m + \frac{0.2m}{1+(1-m)^{-6}}, \quad (7.25)$$

where $m = M_{c2}/M_2$, M_{c2} being the mass of the core.

According to [63], typical values of the thermal mass-radius exponent are

$$-0.3 < \zeta_{\text{therm}} < -0.2. \quad (7.26)$$

Since the adiabatic exponent ζ_{ad} remains larger than -0.2 unless $m < 0.08$, the criterion of thermal stability is stronger than the criterion of adiabatic stability unless the relative core mass is very small.

For the Roche lobe mass-radius exponent, a simple expression is given, for instance, by [63] (basing on the standard arguments from [69]):

$$\zeta_{\text{R}_L} = q(1-Q)\frac{2\nu+1}{1+q} + 2Qq - 2 + \beta(1+Qq), \quad (7.27)$$

where $\nu = \frac{2}{3}k^2 \left(\frac{R_1}{d}\right)^2 \frac{M^2}{M_1 M_2}$ (so that $\frac{j}{J} = \nu \frac{\dot{M}}{M}$, see the equations (7.2) and (7.3)) and $\beta = \frac{d \ln(R_L/d)}{d \ln q}$. The expression for β is obtained by differentiation of the formula (7.10):

$$\beta_2 = \frac{q^{1/3}}{3} \left[\frac{2}{q^{1/3}} - \frac{1.2q^{1/3} + \frac{1}{1+q^{1/3}}}{0.6q^{2/3} + \ln(1+q^{1/3})} \right]. \quad (7.28)$$

So, the investigation of stability of the mass transfer reduces to calculations of the mass-radius exponents according to the equations (7.25), (7.26) and (7.27) and to verification of the condition (7.23). The results of numerical calculations are represented in the Section 7.4.

7.3 Numerical solution of the main equations

The equations from the previous section may be solved numerically. For this purpose, the input parameters (among which are the masses of the stars, the separation, the angular momentum loss parameter k , the parameter of the mass transfer effectiveness Q , the chemical composition of the donor) are provided with initial values. Thereafter, the nuclear evolution of the primary on the main sequence is followed with the help of the *sse.f* evolutionary code, until the radius of the primary reaches its critical Roche lobe. The output file of *sse.f* includes $\log L$, $\log R$, $\log T_{\text{eff}}$ values, also the core mass M_c and mass loss rate \dot{M} as functions of evolutionary time from the Zero-Age Main-Sequence (ZAMS).

From this point, the integration is realized step by step. At each step, the Kelvin-Helmholtz timescale t_{KH} is found according to (7.13) and then, the donor radius increment ΔR_2 is obtained from (7.12). At the same time it is checked whether ΔR increment exceeds the preset limit of $\Delta R_{2\text{lim}}$. The increment of the orbital period P is calculated from the expression (7.1) using the definitions (7.2) – (7.3), and the critical Roche lobe radius R_L is found by (7.10). Basing on the Roche lobe overfilling rate $R_2 - R_L$, the increment of the mass of the donor is computed from (7.7) with the use of the hydrodynamical timescale t_{HD} by (7.9). The new value of the semimajor axis d is found basing on the new values of the total mass and the period of the system as

$$d = \left[G(M_1 + M_2) \left(\frac{P}{2\pi} \right)^2 \right]^{\frac{1}{3}}. \quad (7.29)$$

This iteration process is repeated (with a variable time increment Δt , which is taken in each step so that the mass of the donor does not change more than about 0.1%), until one of the two conditions is satisfied: (1) the radius of the donor R_2 at a subsequent step becomes again smaller than the critical Roche lobe radius R_L . In this case, due to the mass loss, the donor shrinks below its Roche lobe, the mass transfer disrupts, and the consequent orbital evolution discontinues; (2) the orbital evolution accompanied by shrinkage of the orbit leads to shortening of the period down to $\sim 20^d$. This corresponds to formation of a close binary. Below this range, the basic prerequisites of the described model are broken (Alfvén radius concept is not applicable, complicated hydrodynamics should be involved), so integration is stopped at this point.

7.4 Results of numerical modeling

Calculations were made for various sets of the initial parameters in order to clarify how the evolution of a binary depends on the starting characteristics of the system. The evolution of the period and of the semi-major axis was investigated at different values of the parameters characterizing the system, in order to reveal the factors influencing in the greatest extent orbit shrinkage and close binary formation.

As it could have been expected, it was discovered that the final orbit of the system is quite sensitive to the initial separation of the components, to the ratio of the mass transfer rate to the mass loss rate, and to the corotation radius. For larger initial separations the system has time only for moderate orbit shrinkage, when the primary star contracts again and its radius "drops" again below the Roche lobe. The Roche lobe contraction follows the contraction of the orbit, but the donor, having lost certain amount of its mass, contracts quicker than the Roche lobe, so its radius becomes again smaller than R_L , and the mass transfer disrupts. However, if the stars are initially close enough to each other, the timescale of the contraction of the secondary component is longer than the timescale of the Roche lobe contraction, so the donor overfills its Roche lobe until the orbit shrinks dramatically. This is illustrated by the Figure (38) where the evolution of the semimajor axis of a system is represented for different initial separations d_0 : in all tracks, except for the one with $d_0 = 150 R_\odot$, initial separations are too large for the orbit to shrink significantly during the mass transfer phase. Growth of the separation before the Roche lobe is filled in occurs due to the general mass lost by the system. In the Figure (39) the Roche lobe and the donor radius evolution is followed for two values of d_0 . It is seen that after the radius of the donor reaches the Roche lobe, both radii evolve jointly. On the pair of the tracks with $d_0 = 250 R_\odot$ the mass transfer disrupts before the orbit shrinks significantly, on the tracks with $d_0 = 200 R_\odot$ the joint evolution leads to drastic shrinkage of the orbit. The evolution of the donor mass is represented in the Figure (40).

Smaller values of the corotation radius do not enable effective orbit shrinkage. This is illustrated by the Figure (41), where the evolution of the semi-major axis of a system is represented for different values of the coefficient k (see the equation (7.3)).

With high accretion rates ($\dot{M}_1 \geq 0.3 \dot{M}$), a system loses the angular momentum much more effectively, and this favors close binary formation. In the Figure (42) the period evolution is shown for different values of the mass accretion effectiveness Q .

The timescale for formation of a close binary, following the Roche lobe overfilling by the donor, is $\sim 10^7$ yrs, which is comparable to the

thermal timescale of the low mass companion. Our results indicate that the orbital evolution of the system, being sensitive to the parameters of mass and momentum loss effectiveness, may follow in different ways. With some combinations of these parameters, effective shrinkage of the orbit is provided, in other cases, the mass transfer disrupts before the semi-major axis shrinks considerably. That should explain why pre-EHB systems with very different orbital separations are found.

A simple approximating formula was found for the mass loss rate:

$$\dot{M}_2 = C \cdot \frac{L_2}{M_2 R_2^{3.2}}, \quad (7.30)$$

where $C \sim (2 \cdot 10^{-4} \div 2 \cdot 10^{-3})$, and L , M and R are correspondingly luminosity, mass and the radius of the star in solar units. The relation (7.30) holds for the phase of Roche lobe filling irrespectively of the value of the parameter k and the mass accretion rate Q over more than one order of magnitude changes in the radius of the donor R_2 and the separation of the components d . The value of the numerical factor C depends on choice of the hydrodynamical timescale t_{HD} , the value of the R power slightly depends on the initial mass ratio q , having a tendency to decrease somewhat with increment of the initial donor mass. In the Figure (44) \dot{M}_2 is depicted in accordance with the equation (7.30), together with the linear dependence, in order to demonstrate the quality of the fit. Noticeable departures from the linear relation occur when the radius of the donor becomes appreciably smaller than the Roche lobe radius. This linear dependence holds also for the regime when the trend of the stellar radius changes for the opposite when the donor (remaining within its Roche lobe) switches from increase of its radius to decrease; however, the numerical factor changes in this case (but not the power coefficient at R_2). The relation (7.30) holds for the donor masses up to $M_2 \sim 0.3M_\odot$. With higher donor masses, C becomes dependent on the value of the parameter k , the value of R power also tends to change slightly from trend to trend.

It was proved that the most important role in close binary formation play the initial separation of the components d_0 and the angular momentum loss parameter k , as well as the mass transfer rate parameter Q . It should be concluded that binarity indeed favors EHB formation. The assumption that the progenitors of EHB objects belong to the binaries with initial separations of $(100 \div 150) R_\odot$ and fill in their critical Roche lobes while being close to the RGB tip, leads one to the deduction that considerable shrinkage of the orbit can be achieved due to the combined effects of the angular momentum loss and appreciable accretion on its low mass companion in the hydrodynamical timescale of the donor. These effects result in formation of a helium white dwarf with a mass of about $0.5 M_\odot$. According to

the proposed scenario, sufficiently high accretion rates ($Q \sim 0.3$) and large Alfvén radii $R_A > (3 \div 4) R_2$ are the prerequisite conditions for formation of binaries with EHB objects.

These results support the previous conclusion of [45] where it was found that the large observed range of P_{orb} and sdB masses presents a challenge to simple theories of formation of sdB stars based on common envelope scenario. More far reaching conclusions will be possible after more detailed and reliable data is provided on physical parameters of EHB components on the base of further analysis of spectra, light curves and radial velocity curves of these objects.

Numerical calculations were realized also to check the fulfillment of the set of the stability conditions in the Section 7.2. The analysis showed that in most cases the stability condition (7.23) is not fulfilled. This result is demonstrated by the Figures (32) – (36). They represent behavior of the mass-radius exponents ζ_{ad} , ζ_{therm} and ζ_{RL} as functions of the mass ratio q in the course of the evolution of a binary system.

In the Figure (31) behavior of the Roche lobe mass-radius exponent ζ_{RL} is represented alone as function of the parameters k and Q . It may be concluded from this figure that almost for the whole range of these parameters, ζ_{RL} remains relatively high ($\zeta_{\text{RL}} > -0.3$, the line $\zeta_{\text{RL}} = 0.3$ is also represented in this figure for comparison), except for low values of k and specifically Q in the very beginning of the orbital evolution. As it has been already mentioned, such low values of these parameters do not enable effective shrinkage of the orbit, and the figure supports this conclusion (the corresponding lines end up before q reaches significant values, *i.e.* before a considerable fraction of the mass is transferred to the accretor). For higher values of k and Q , the Roche lobe mass-radius exponent remains higher than -0.3 , the latter value corresponding to the thermal mass-radius exponent. This result means that the mass transfer is generally unstable at least in the heat diffusion (Kelvin-Helmholtz) timescale.

The Figure (32) repeats the previous one, but for larger initial separation, $d_0 = 1000 R_{\odot}$. As it should be expected, the results are very similar. So large separations do not enable effective orbital shrinkage for any combinations of the parameters k and Q , so the mass transfer disrupts at smaller values of q . It is seen that the mass transfer is stable only for small Q , but if k is large, stability is lost soon after beginning of the mass transfer.

The Figures (33) – (36) represent adiabatic, thermal and Roche lobe mass-radius exponents as functions of the mass ratio q for some values of the coefficients k and Q . As it may be expected, stability is mostly defined by the thermal mass-radius exponent ζ_{therm} , since $\zeta_{\text{therm}} < \zeta_{\text{ad}}$ during practically entire orbital evolution phase, except for the very beginning,

when the donor has not still formed the core. Values of ζ_{RL} , which are generally higher than ζ_{ad} and ζ_{therm} , support the conclusion of instability of the mass transfer in the thermal and, in practice, also in the adiabatic timescales.

Chapter 8

Achieved objectives and conclusions

8.1 Achieved objectives

In the course of the present work, the following objectives were achieved:

- an original two-layer model of the atmosphere of the unevolved companion, irradiated by far UV flux from the near-by primary star, was elaborated and realized in computer codes, together with a monochromatic light curve constructing algorithm;
- influence of PCB parameters on conditions in the atmosphere of the secondary component was studied;
- monochromatic light curves of selected PCBs (eclipsing and non-eclipsing) were modeled theoretically and fitted to observations, sets of parameters for these systems were proposed;
- the orbital evolution of binary progenitors of EHB stars was investigated, conditions necessary to effective semi-major axis shrinkage were established. Empirical relation for mass-loss rate was found;
- mass transfer stability conditions were studied in binary progenitors of EHBs.

8.2 Conclusions

Basing on the investigations carried through in this Thesis, the following conclusions may be made:

- far UV flux from the hot primary component in PCB systems is absorbed in a relatively thin layer of the atmosphere of the secondary companion ($\Delta r \sim 10^8$ cm) where LTE is non-existent. This layer turns to be transparent for photons with $\lambda > 912$ Å, 912 Å being the Lyman limit;
- recombinations are the important cooling mechanism in this layer, but they cannot provide drain for the whole energy of the impinging flux. A considerable portion of the energy from the outward flux

is spent on electron gas heating and possibly on excitation of non-stationary processes with timescales comparable to the orbital period;

- a temperature inversion exists in the overheated upper atmospheric layers of the secondary. One of the consequences of this inversion is presence of the limb-brightening effect, contrary to the ordinary limb-darkening present in atmospheres of single stars or in weakly-irradiated atmospheres;
- initially wide pairs may evolve to short-period systems in the course of the mass loss after critical Roche lobe overfilling by one of the components. Effectiveness of shrinkage of the orbit critically depends on the initial separation of the system as well as on effectiveness of the orbital momentum loss mechanisms. Depending on these factors, pairs with a wide range of periods may be formed, including systems with EHB properties;
- investigations of mass transfer stability demonstrate that the stability conditions are not fulfilled in most cases, including all cases leading to formation of a short-period binary. This points to instability of mass transfer. However, despite the fact that the mass transfer timescale is quite short ($\sim 10^4$ yrs), it may result in significant orbital period changes.

Appendix A

Absorption coefficients

A.1 Cross-sections of hydrogen-like atoms

A.1.1 Neutral H cross-section

Neutral H absorption coefficients are calculated following the formulae by Unsold. The bound-free absorption coefficient $a_{H_{bf}}$ is

$$a_{H_{bf}}(\nu, T) \simeq a_0 \lambda^3 \left\{ \frac{kT}{2I} \left[\exp\left(-\frac{\chi_{n_0+3}}{kT}\right) - \exp\left(-\frac{I}{kT}\right) \right] + \sum_{n=n_0+2}^{n_0+2} \frac{g'_n}{n^3} \exp\left(-\frac{\chi_n}{kT}\right) \right\}. \quad (\text{A.1})$$

The absorption coefficient $a_{H_{ff}}$ for free-free transitions is

$$a_{H_{ff}}(\nu, T) \simeq a_0 \lambda^3 \frac{kT}{2I} g_f \exp\left(-\frac{I}{kT}\right). \quad (\text{A.2})$$

In (A.1) and (A.2), g'_n and g_f are the Gaunt factors calculated according to the following expressions (see [17]):

$$g'_n = 1 - 0.3456 \left(\frac{I}{h\nu}\right)^{-\frac{1}{3}} \left(\frac{I}{h\nu n^2} - \frac{1}{2}\right), \quad (\text{A.3})$$

$$g'_f = 1 + 0.3456 \left(\frac{I}{h\nu}\right)^{-\frac{1}{3}} \left(\frac{I}{h\nu} + \frac{1}{2}\right). \quad (\text{A.4})$$

In the formulae (A.1) – (A.4), the following designations are used: $a_0 \simeq 1.0449 \cdot 10^{-26} \text{ cm}^2/\text{\AA}^3$ is the atomic absorption coefficient; $I \simeq 13.60 \text{ eV}$ is the ionization potential of the first level; $\chi_n = I(1 - 1/n^2)$ is the ionization potential of the level number n ; $n_0 = \left\lceil 1 + \sqrt{I/h\nu} \right\rceil$ is the lowest level ionized by ν -frequency ionization. Since the formula (A.4) results in unphysically high values inside some frequency ranges, we limit g_f value by $g_{f \max} \equiv 1.5$.

The formulae (A.3) and (A.4) do not take into account negative absorption; for this reason we should use the following expression for the total absorption coefficient of neutral H

$$a_H(\nu, T) = (a_{H_{bf}} + a_{H_{ff}}) \left[1 - \exp\left(-\frac{h\nu}{kT}\right) \right]. \quad (\text{A.5})$$

For hydrogen-like atoms analogous equations are applicable, with the following correction: the expressions for the bound-free and the free-free absorption coefficients should be multiplied with the square atomic number Z^2 , with simultaneous increment of the ionization potential I by Z^2 . The respective Gaunt factors also should be applied. We used this method for neutral He ($Z = 2$) absorption coefficients computations, adopting unit Gaunt factors.

A.1.2 H^- cross-section

The following expressions are applied to compute the hydrogen negative ion absorption coefficient [17]:

$$a_{H_{bf}^-}(\nu, T, P_e) \simeq 4.158 \cdot 10^{-10} a_{bf} P_e \Theta^{\frac{5}{2}} \cdot 10^{0.754\Theta} \quad [\text{cm}^2], \quad (\text{A.6})$$

$$a_{H_{ff}^-}(\nu, T) \simeq 10^{f_0+f_1 \log \Theta+f_2 \log^2 \Theta} \quad [\text{cm}^2]. \quad (\text{A.7})$$

In these formulae P_e is the electron gas pressure in dyn and $\Theta = \frac{5040}{kT}$. The numerical coefficients a_{bf} , f_0 , f_1 and f_2 are expressed empirically as follows:

$$\log a_{bf} = \begin{cases} -16.20450 + 0.17280 \cdot 10^{-3} \lambda_1 + 0.39422 \cdot 10^{-7} \lambda_1^2 + \\ \quad + 0.51345 \cdot 10^{-11} \lambda_1^3, & \text{if } 1500 \text{ \AA} < \lambda < 5250 \text{ \AA}; \\ -16.40383 + 0.61356 \cdot 10^{-6} \lambda_1 - 0.11095 \cdot 10^{-7} \lambda_1^2 + \\ \quad + 0.44965 \cdot 10^{-13} \lambda_1^3, & \text{if } 5250 \text{ \AA} \leq \lambda < 11\,250 \text{ \AA}; \\ -15.95015 - 0.36067 \cdot 10^{-3} \lambda_1 + 0.86108 \cdot 10^{-7} \lambda_1^2 - \\ \quad - 0.90741 \cdot 10^{-11} \lambda_1^3, & \text{if } 11\,250 \text{ \AA} \leq \lambda < 15\,000 \text{ \AA}, \end{cases} \quad (\text{A.8})$$

where $\lambda_1 = \lambda - 8500$ [\AA];

$$\begin{aligned} f_0 &= -31.63602 + 0.48735 \log \lambda + \\ &\quad + 0.296586 \log^2 \lambda - 0.0193562 \log^3 \lambda, \\ f_1 &= 15.3126 - 9.33651 \log \lambda + \\ &\quad + 2.000242 \log^2 \lambda - 0.1422568 \log^3 \lambda, \\ f_2 &= -2.6117 + 3.22259 \log \lambda - \\ &\quad - 1.082785 \log^2 \lambda + 0.1072635 \log^3 \lambda. \end{aligned} \quad (\text{A.9})$$

We extended the range of wavelengths used in the equation (A.6). For $15\,000 \text{ \AA} \leq \lambda < 17\,000 \text{ \AA}$ we use the third of the empirical fits (A.8), elsewhere we adopt $a_{bf} \equiv -20$. The fit (A.7) is valid for $3038 \text{ \AA} \leq \lambda \leq 91\,130 \text{ \AA}$, elsewhere we adopt $a_{H_{ff}^-} \equiv 0$.

Since the fit (A.6) does not take into account induced transitions, the total absorption coefficient of H^- is given by the following expression:

$$a_{H^-}(\nu, T, P_e) = a_{H_{bf}^-} \left[1 - \exp\left(-\frac{h\nu}{kT}\right) \right] + a_{H_{ff}^-}. \quad (\text{A.10})$$

Note: Since some expressions for absorption coefficients include non-continuous empirical expressions, it may result in non-continuous behavior of the absorption coefficients in several wavelength ranges. That may lead to minor calculation-induced peculiarities, for instance in computed spectra. However, they are of local nature and do not affect the results in general.

A.2 Ionization in the atmosphere

We consider that the atmosphere of the secondary contains three elements: hydrogen, helium and a metal. The metal predominantly plays role of electrons donor, its role as absorption agent is negligible. Four absorption agents are taken into account in our model: neutral H ; hydrogen negative ion H^- ; neutral He ; free electrons. For each element j we find ratios of its particle concentration (neutral and once ionized, higher ionizations are neglected) N_j to neutral H atoms concentration N_H :

$$A_j = N_j/N_{H\text{neut}}. \quad (\text{A.11})$$

When LTE is established in the atmosphere, the Boltzmann-Saha law is valid:

$$\frac{N_{j1}}{N_{j0}} = \frac{\Phi_j}{P_e}, \quad (\text{A.12})$$

N_{j0} and N_{j1} being respectively the number of neutral and single ionized atoms of the element j , P_e being the electron gas pressure and

$$\Phi_j(T) = 0.333 \frac{2B_{1j}}{B_{0j}} T^{\frac{5}{2}} \exp\left(-\frac{11\,600\chi_j}{T}\right) \quad [\text{dyn}]. \quad (\text{A.13})$$

Here χ_j is the ionization potential (in eV) of the element j , ratios of statistical sums $2B_{1j}/B_{0j}$ for different elements are given by [3].

Following [17], we obtain the electron gas pressure by numerical solution of the following transcendental equation:

$$P_e = P \frac{\sum_j A_j \frac{\Phi_j}{\Phi_j + P_e}}{\sum_j A_j \left[1 + \frac{\Phi_j}{\Phi_j + P_e} \right]} \quad (\text{A.14})$$

(j in the sums runs through values 1 – H , 2 – He and 3 – metal).

To compute the total and the mean absorption coefficients, we need values of N_{j0} and N_{j1} . They are computed with the use of the following expressions:

$$\begin{aligned} N_{j0} &= \frac{P-P_e}{kT} \frac{P_e}{\Phi_j+P_e}, \\ N_{j1} &= \frac{P-P_e}{kT} \frac{\Phi_j}{\Phi_j+P_e}. \end{aligned} \quad (\text{A.15})$$

A.3 Total absorption coefficient

Once the ionization state of medium is obtained, the total absorption coefficient may be readily found as sum of the absorption coefficients of the four above-mentioned agents:

$$\kappa(\nu, T, P) = N_{H0}a_H + N_{H0}a_{H^-} + N_{He0}a_{He} + \sigma_0 N_e, \quad (\text{A.16})$$

$\sigma_0 = 0.6655 \cdot 10^{-24} \text{ cm}^2$ being the Thompson cross-section of free electrons, $N_e = P_e/kT$ being the concentration of free electrons, the cross-sections a_H , a_{He} and a_{H^-} are computed by the expressions (A.5) and (A.10).

A.4 Mean absorption coefficients

The mean absorption coefficient $\bar{\kappa}(T, P)$ is needed in some calculations. There exist various methods of $\bar{\kappa}$ definition. The Planck mean and the Rosseland mean are widely used for this purpose. Our algorithm provides the possibility to apply any of them.

The Planckian mean is defined as follows:

$$\begin{aligned} \bar{\kappa}_{\text{Pl}}(T, P) &= \frac{\int_0^\infty \kappa(\nu, T, P) B(\nu, T) d\nu}{\int_0^\infty B(\nu, T) d\nu} \\ &= \frac{\pi}{\sigma T^4} \int_0^\infty \kappa(\nu, T, P) B(\nu, T) d\nu, \end{aligned} \quad (\text{A.17})$$

The Rosseland mean is defined as follows:

$$\begin{aligned} \bar{\kappa}_{\text{Ros}}(T, P) &= \frac{\int_0^\infty \frac{d}{dT} B(\nu, T) d\nu}{\int_0^\infty \frac{1}{\kappa(\nu, T, P)} \frac{d}{dT} B(\nu, T) d\nu} \\ &\simeq \frac{\int_0^\infty \frac{1}{\kappa(\nu, T, P)} \frac{z^4 e^z}{(e^z - 1)^2} dz}{\int_0^\infty \frac{1}{\kappa(\nu, T, P)} \frac{z^4 e^z}{(e^z - 1)^2} dz} \\ &\text{where } z = \frac{h\nu}{kT}. \end{aligned} \quad (\text{A.18})$$

In the formulae (A.17) and (A.18),

$$B(\nu, T) = \frac{2h\nu^3}{c^2} \frac{1}{\exp\left(\frac{h\nu}{kT}\right) - 1} \quad (\text{A.19})$$

is the Planck law, σ is the Stephan-Boltzmann constant.

A.5 Technical details

- (i) To provide calculations precision, upper limits and numbers of steps in the numerical integration in the formulae (A.17) and (A.18) are chosen to be parameters-dependent.
- (ii) Calculations of the mean absorption coefficients are time-consuming; however, these coefficients are used actively in model atmosphere computations. In order to accelerate computations, we tabulate these means as two-argument functions of pressure and temperature (for given chemical composition of the atmosphere). So in model atmosphere calculations we interpolate these tables instead of direct integrations. If temperatures and pressures in the atmosphere exceed the ranges of the interpolation tables, we compute the means directly.

Appendix B

Figures

B.1 Geometry of the system

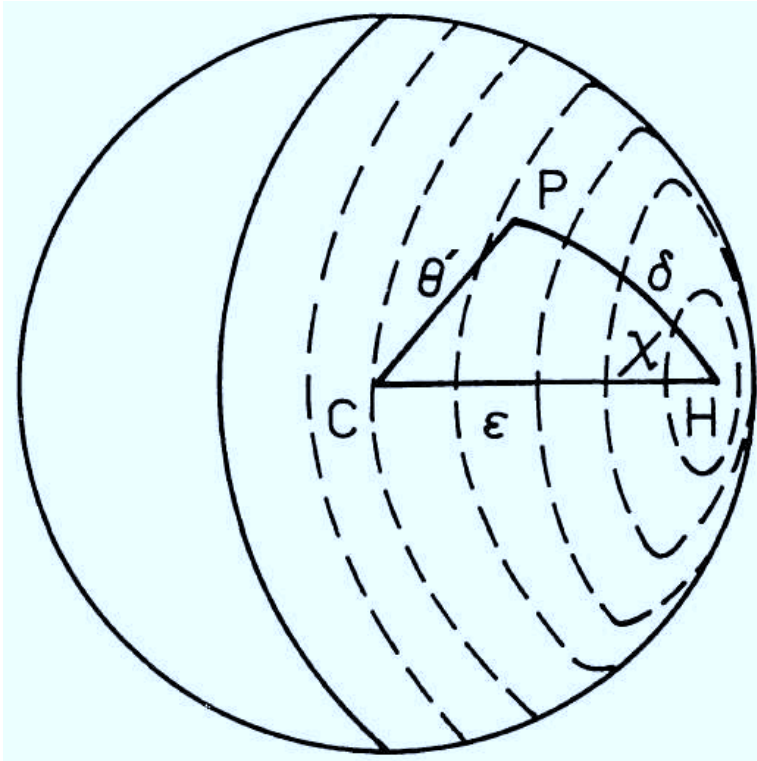


Figure 1. Geometry of the illuminated disc, figure by [46]. C is the visual center of the disc, H is the substellar point, P is an arbitrary point on the surface of the star, ϵ is the angular distance from the substellar point to the center of the disc, δ is the angular distance of the current zone from the substellar point, χ is the angle along the current zone defining the point P position, $\theta' = \pi - \theta$ is the phase angle (see the Section 4.1 for details.)

B.2 Flow block diagram of the program

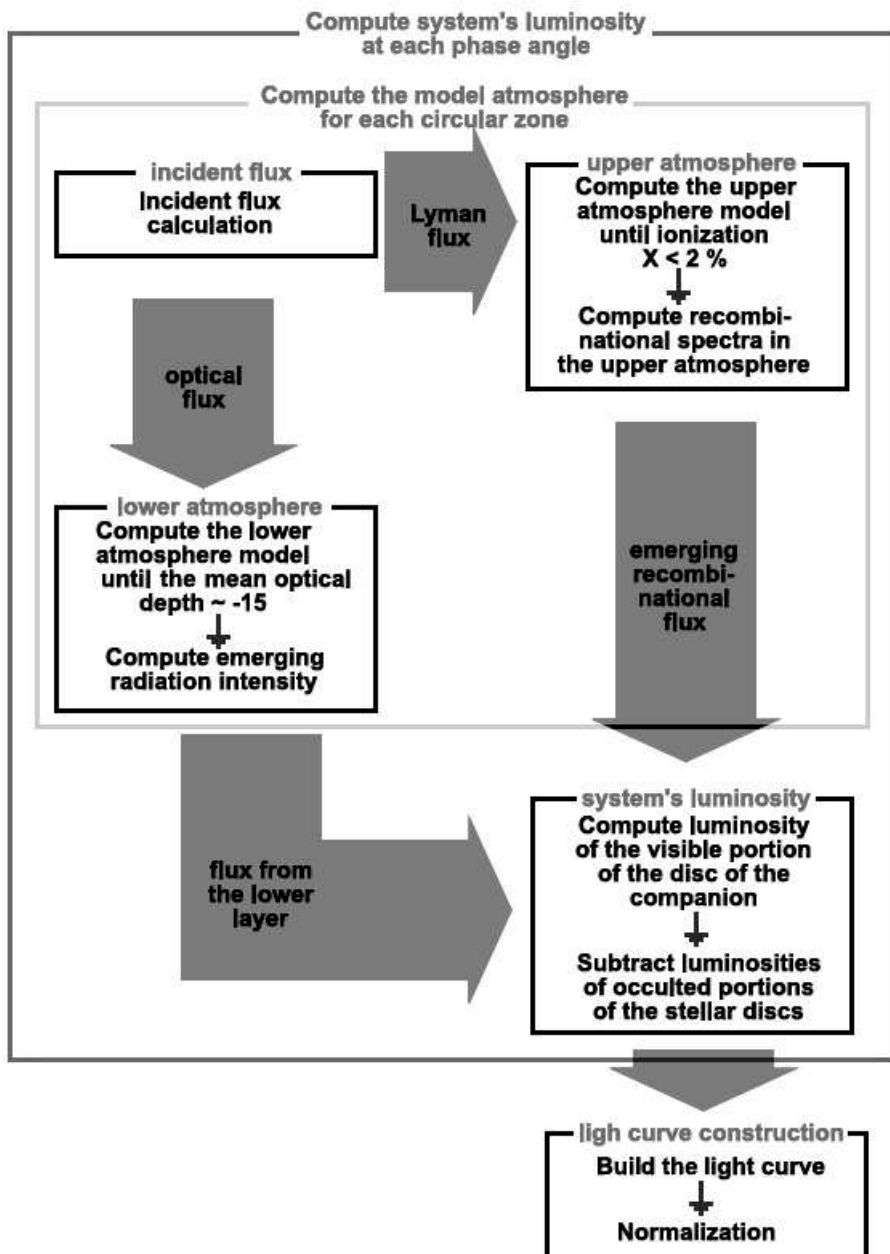


Figure 2.

B.3 Models of the upper atmosphere

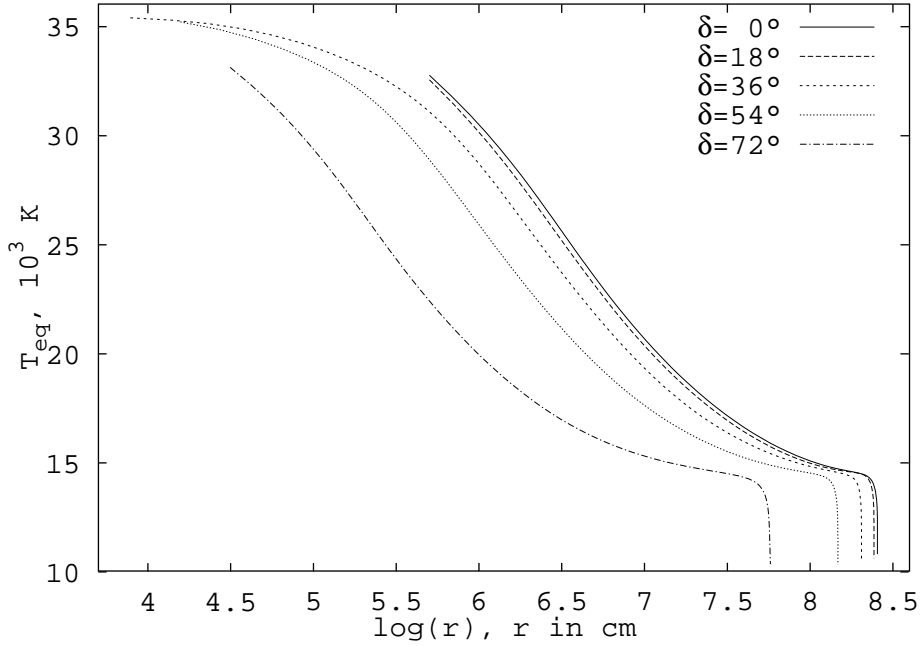


Figure 3. Equilibrium temperature T_{eq} for different angular distances δ from the substellar point. $T_{\text{1eff}} = 60\,000\text{ K}$, $N_0 = 5 \cdot 10^{12}\text{ cm}^{-3}$, other parameters are given in the Section 2.7.2.

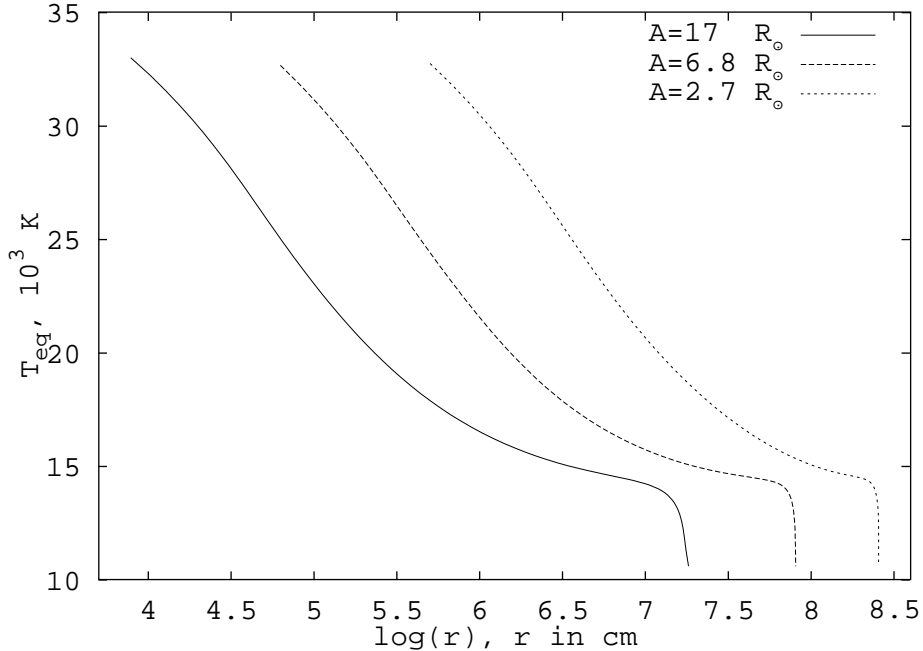


Figure 4. Equilibrium temperature T_{eq} for different semimajor axis values A . $T_{\text{1eff}} = 60\,000\text{ K}$, $\delta = 0^\circ$, other parameters are the same as in the Figure 3.

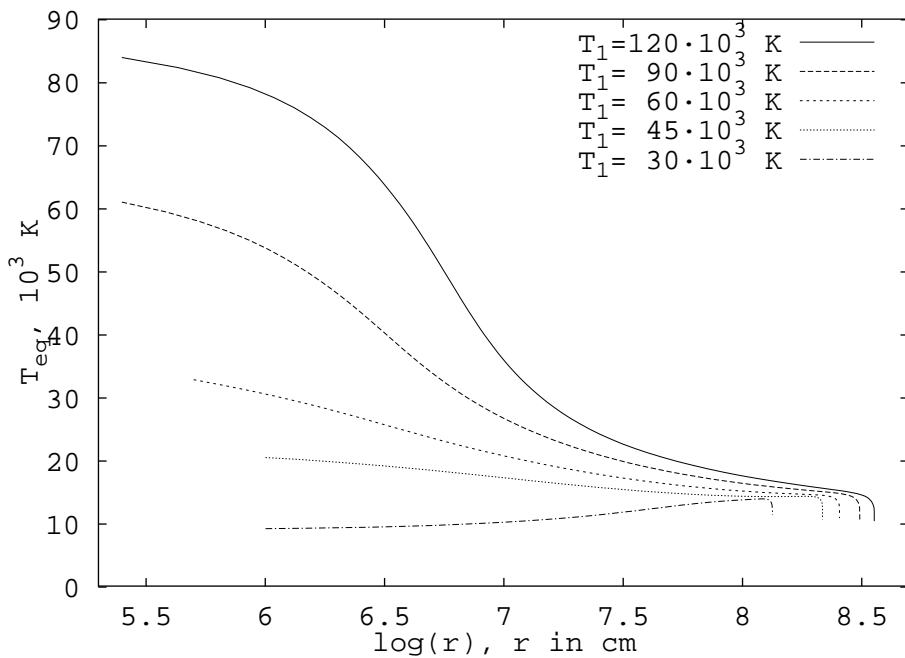


Figure 5. Equilibrium temperature T_{eq} at the substellar point for different primary effective temperatures $T_{1\text{eff}}$. System's parameters are the same as in the Figure 3.

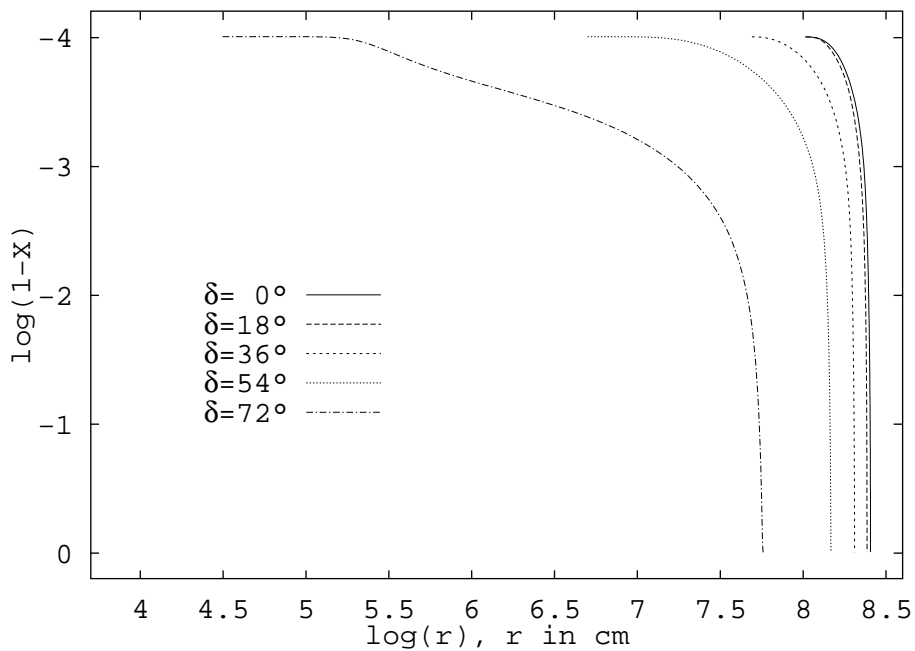


Figure 6. Ionization X for different angular distances δ from the substellar point. $T_{1\text{eff}} = 60\,000$ K, other parameters are the same as in the Figure 3.

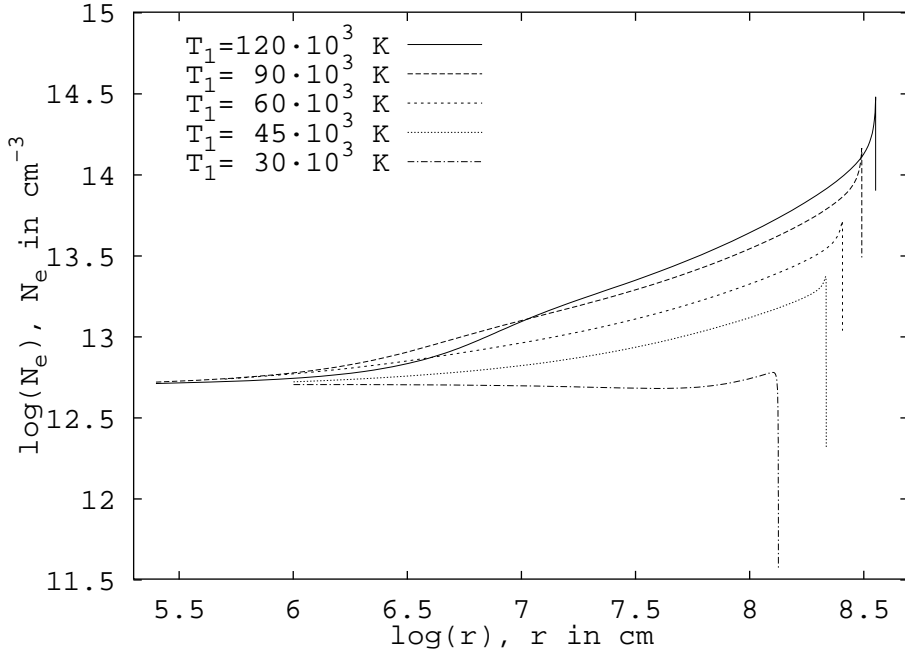


Figure 7. Electron concentration N_e at the substellar point for different primary effective temperatures $T_{1\text{eff}}$. System's parameters are the same as in the Figure 3.

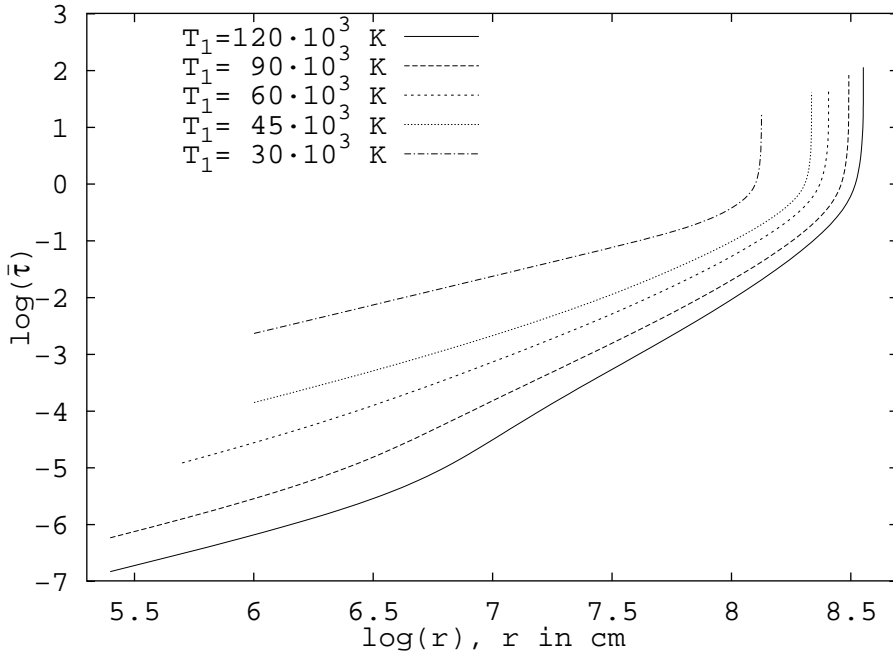


Figure 8. Mean optical depth $\bar{\tau}$ in Lyman continuum at the substellar point for different primary effective temperatures $T_{1\text{eff}}$. System's parameters are the same as in the Figure 3.

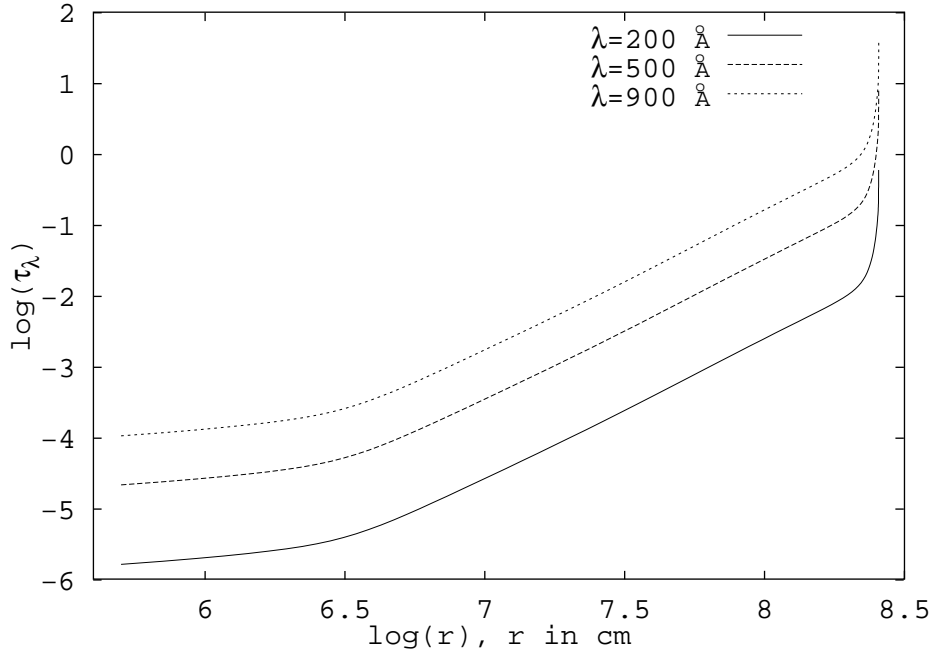


Figure 9. Monochromatic optical depth τ_λ at the substellar point. $T_{\text{1eff}} = 60\,000$ K, other parameters are the same as in the Figure 3.

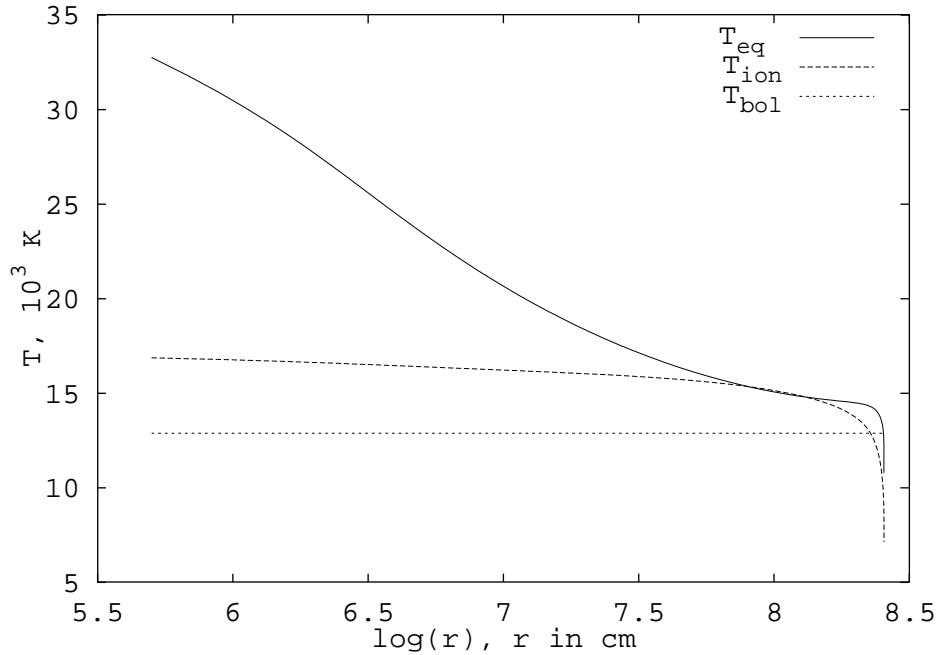


Figure 10. Equilibrium temperature T_{eq} , ionization temperature T_{ion} and bolometric temperature of the impinging flux T_{eq} at the substellar point. $T_{\text{1eff}} = 60\,000$ K, other parameters are the same as in the Figure 3.

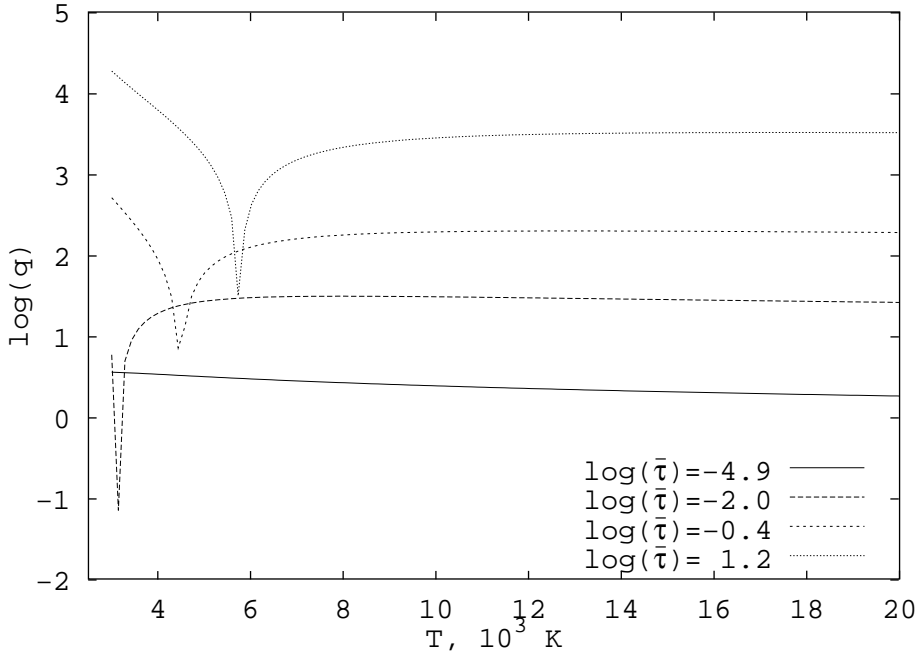


Figure 11. Cooling function $q(T)$ at different mean optical depths $\bar{\tau}$ in the Lyman continuum. The substellar point is considered, $T_{\text{1eff}} = 60\,000$ K, other parameters are the same as in the Figure 3.

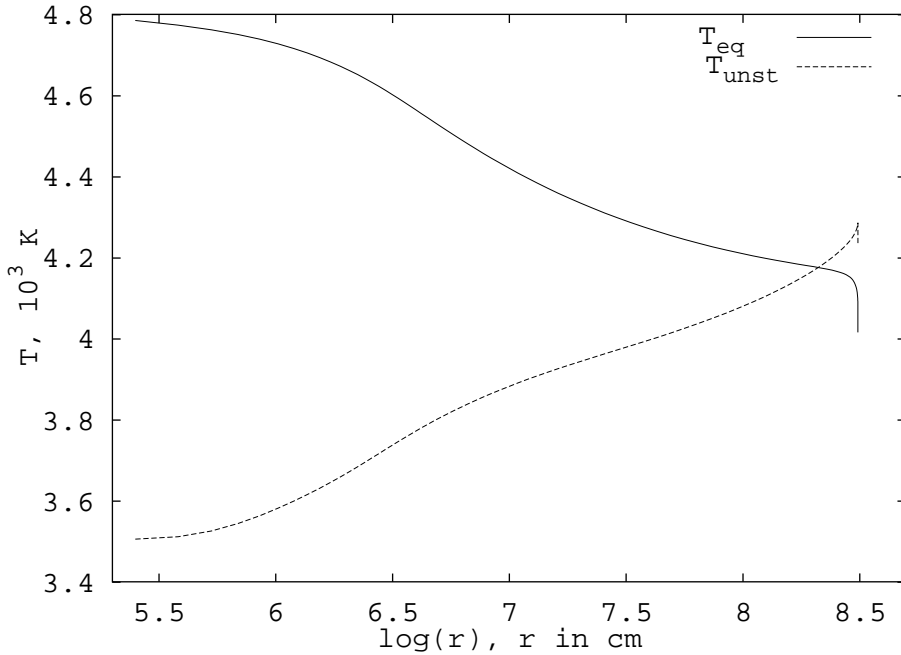


Figure 12. Cooling coefficient maximum temperature profile T_{unst} . Equilibrium temperature T_{eq} is also plotted for comparison. The substellar point is considered, $T_{\text{1eff}} = 60\,000$ K, other parameters are the same as in the Figure 3.

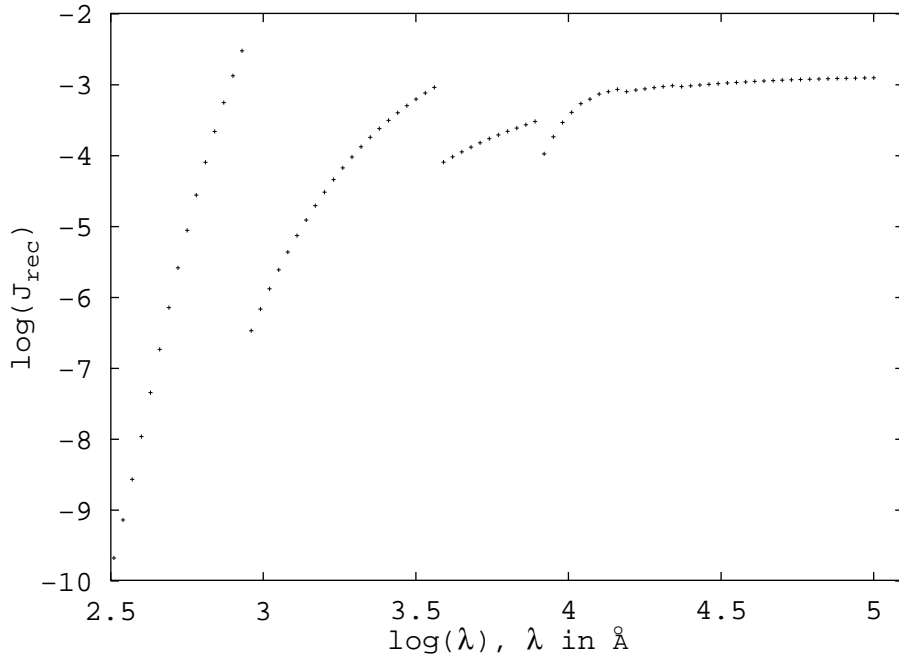


Figure 13. Recombination spectrum of emerging radiation. The sub-stellar point is considered, $T_{\text{eff}} = 60\,000$ K, other parameters are the same as in the Figure 3.

B.4 Examples of continuum spectra of a system

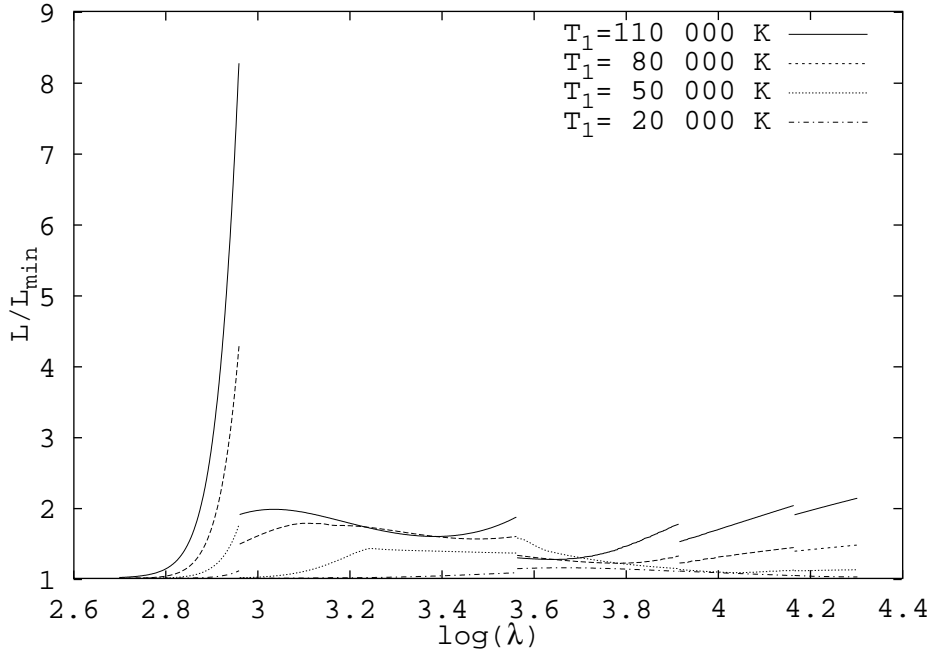


Figure 14. Continuum spectra of systems with different effective temperatures of the primary component. The parameters of the model system are close to that of V477 Lyr: $T_2 = 4000\ \text{K}$, $R_{\text{sep}} = 2.72 R_{\odot}$, $R_1 = 0.23 R_{\odot}$, $R_2 = 0.64 R_{\odot}$, $i = 80^\circ$. The phase angle $\theta = 180^\circ$ corresponds to the maximum of the reflection effect.

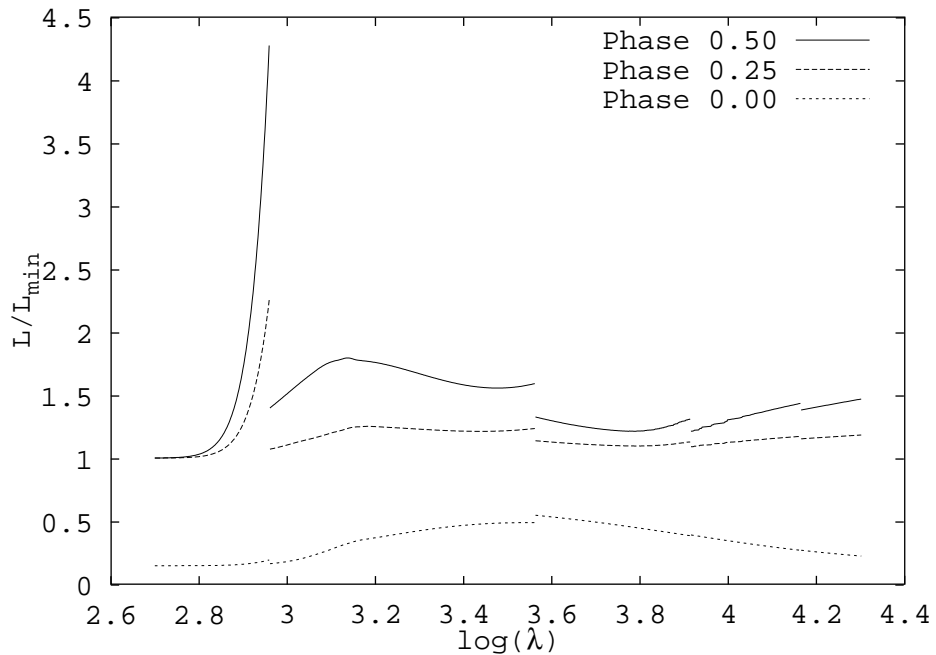


Figure 15. Continuum spectra of a system in different orbital phases (phase 0.00 corresponds to the minimum light, phase 0.50 to the maximum). The parameters of the model system are close to that of V477 Lyr: $T_1 = 80\,000$ K, $T_2 = 4000$ K, $R_{\text{sep}} = 2.72 R_\odot$, $R_1 = 0.23 R_\odot$, $R_2 = 0.64 R_\odot$, $i = 80^\circ$.

B.5 Modeling of light curves of selected PCBs

B.5.1 UU Sge

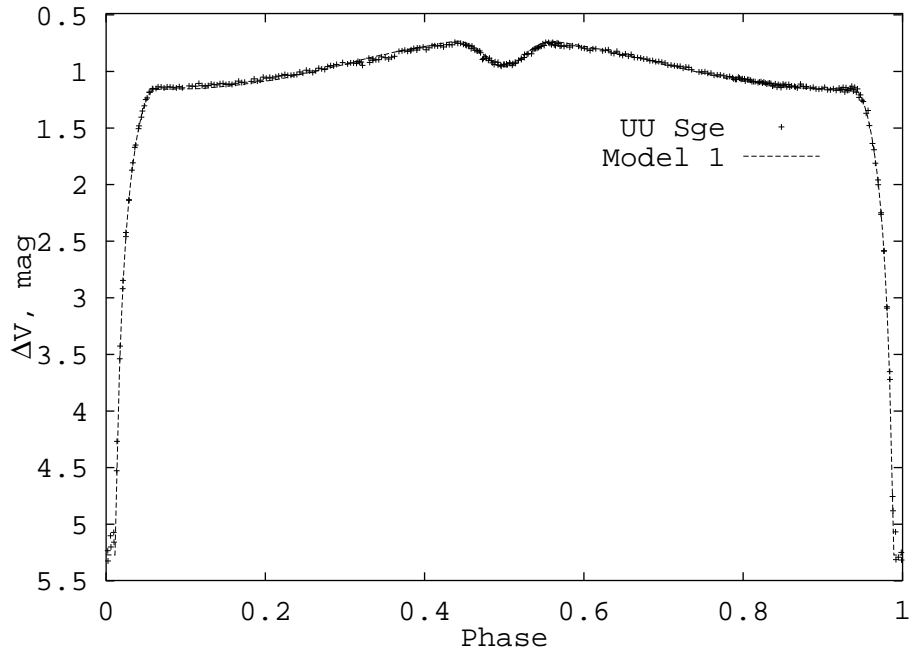


Figure 16. UU Sge V -band light curve and the model. The model system parameters are: $T_1 = 85\,000$ K, $T_2 = 5500$ K, $R_{\text{sep}} = 2.46 R_{\odot}$, $R_1 = 0.359 R_{\odot}$, $R_2 = 0.551 R_{\odot}$, $i = 88^{\circ}.0$.

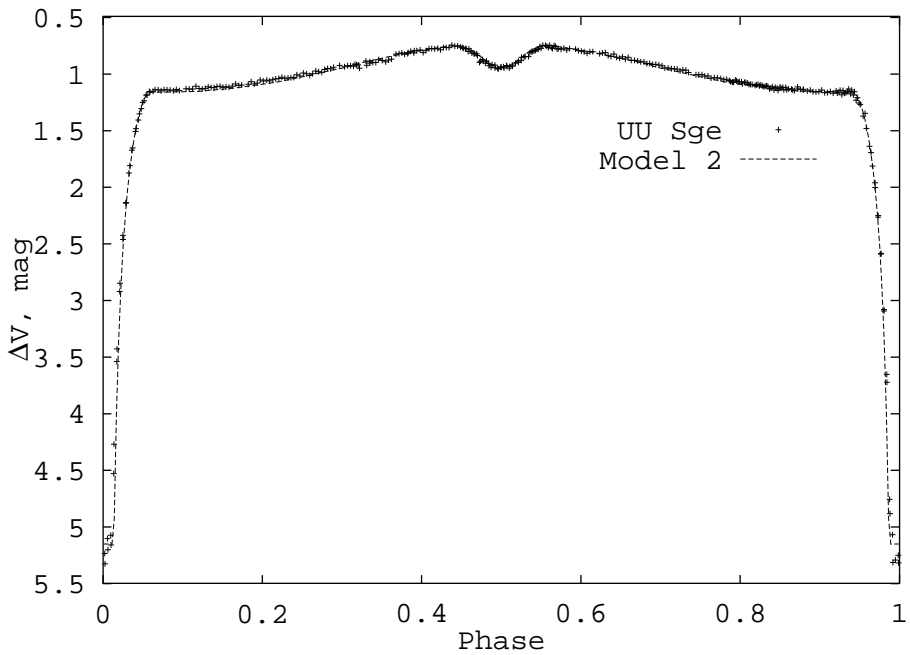


Figure 17. UU Sge V -band light curve and the model. The model system parameters are: $T_1 = 80\,000$ K, $T_2 = 5500$ K, $R_{\text{sep}} = 2.46 R_{\odot}$, $R_1 = 0.335 R_{\odot}$, $R_2 = 0.551 R_{\odot}$, $i = 88^{\circ}.0$.

B.5.2 V477 Lyr

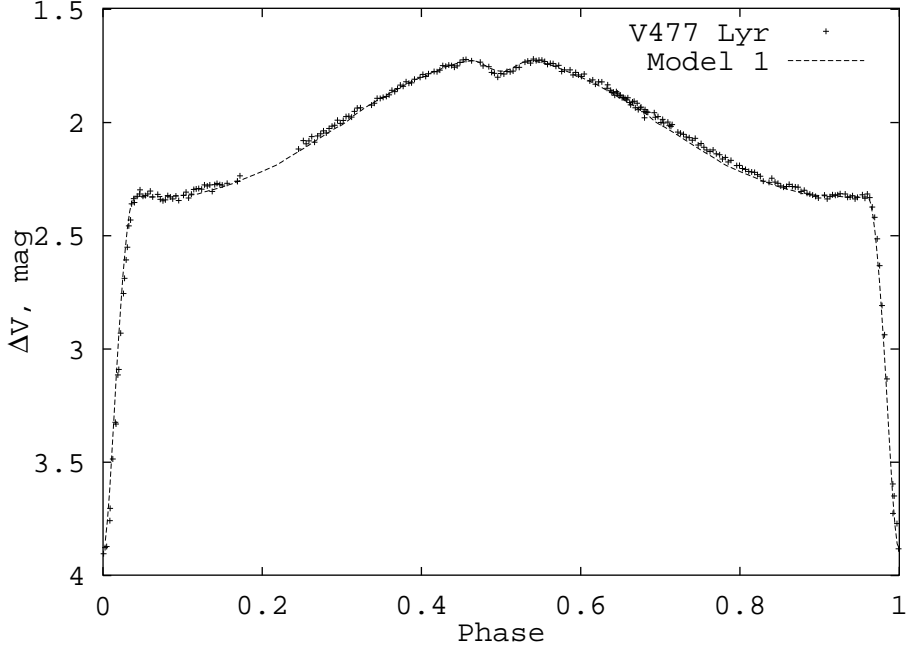


Figure 18. V477 Lyr V -band light curve and the model. The model system parameters are: $T_1 = 102\,000$ K, $T_2 = 4000$ K, $R_{\text{sep}} = 2.72 R_{\odot}$, $R_1 = 0.23 R_{\odot}$, $R_2 = 0.64 R_{\odot}$, $i = 80^{\circ}.9$.

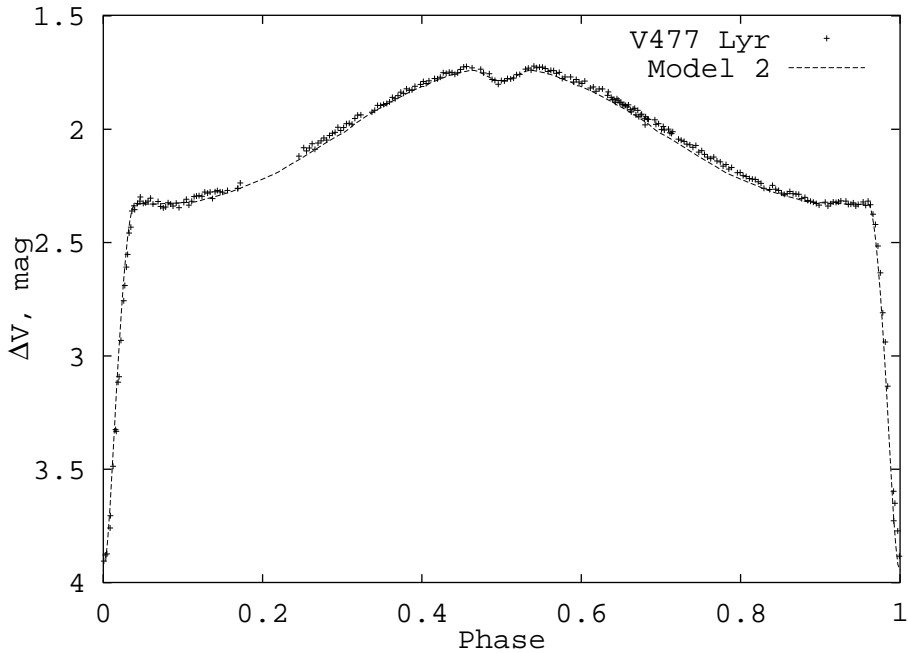


Figure 19. V477 Lyr V -band light curve and the model. The model system parameters are: $T_1 = 94\,000$ K, $T_2 = 4000$ K, $R_{\text{sep}} = 2.72 R_{\odot}$, $R_1 = 0.23 R_{\odot}$, $R_2 = 0.61 R_{\odot}$, $i = 80^{\circ}.3$.

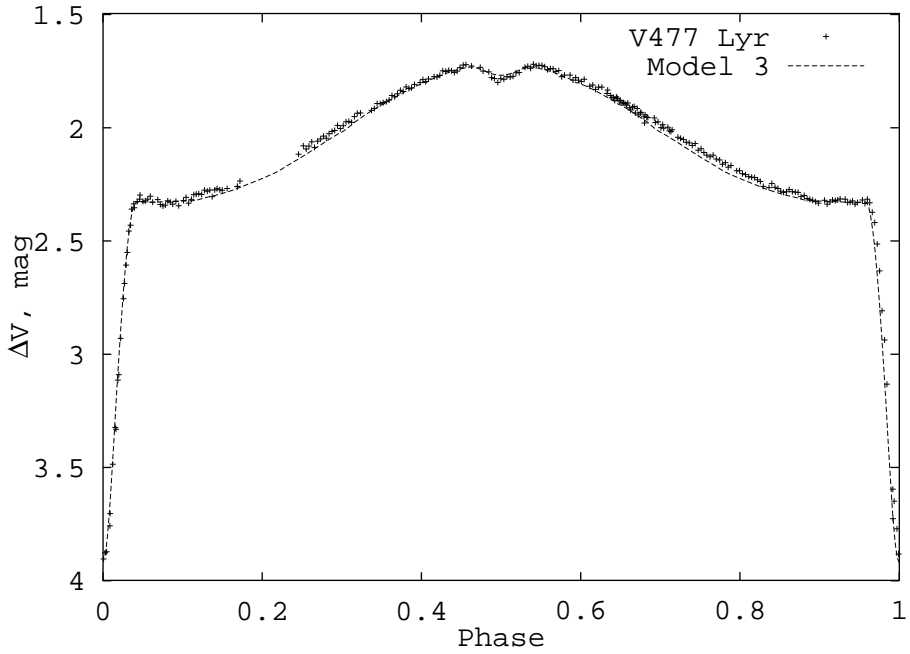


Figure 20. V477 Lyr V-band light curve and the model. The model system parameters are: $T_1 = 87000$ K, $T_2 = 4000$ K, $R_{\text{sep}} = 2.72 R_{\odot}$, $R_1 = 0.23 R_{\odot}$, $R_2 = 0.58 R_{\odot}$, $i = 79^{\circ}.7$.

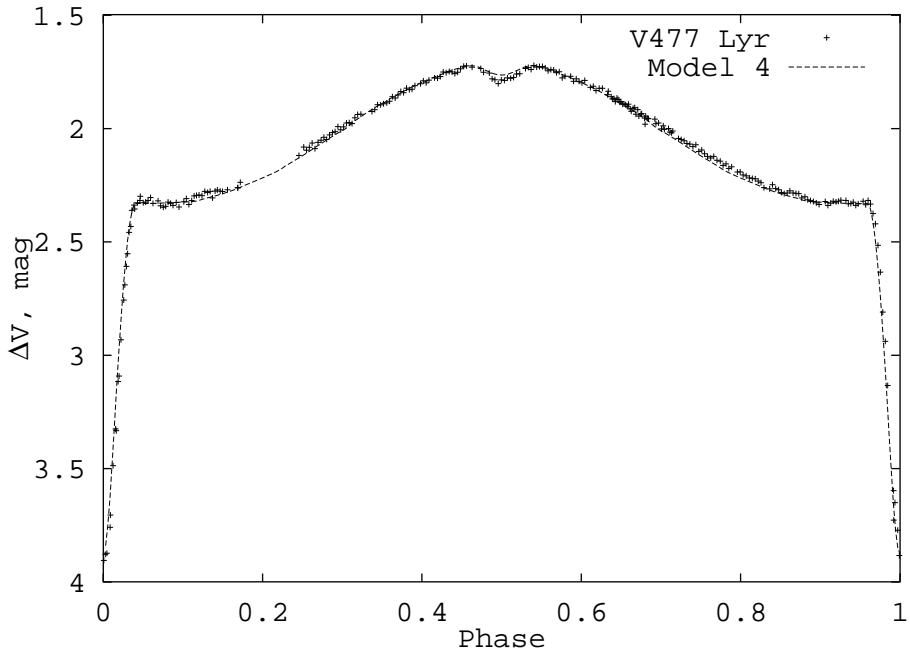


Figure 21. V477 Lyr V-band light curve and the model. The model system parameters are: $T_1 = 74000$ K, $T_2 = 4000$ K, $R_{\text{sep}} = 2.72 R_{\odot}$, $R_1 = 0.23 R_{\odot}$, $R_2 = 0.55 R_{\odot}$, $i = 79^{\circ}.2$.

B.5.3 V477 Lyr and UU Sge positions on the HR diagram

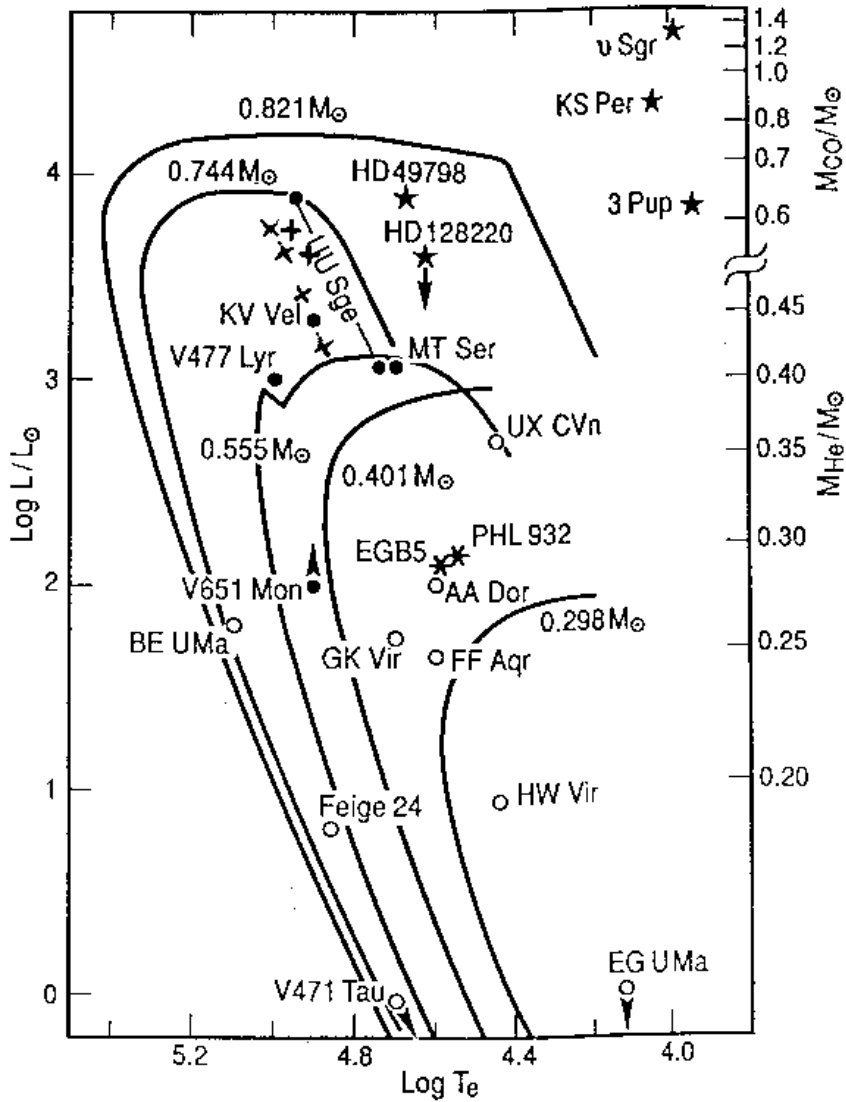


Figure 22. Hertzsprung-Russell diagram by [30] with the new positions of V477 Lyr (crosses) and UU Sge (pluses).

B.5.4 V664 Cas

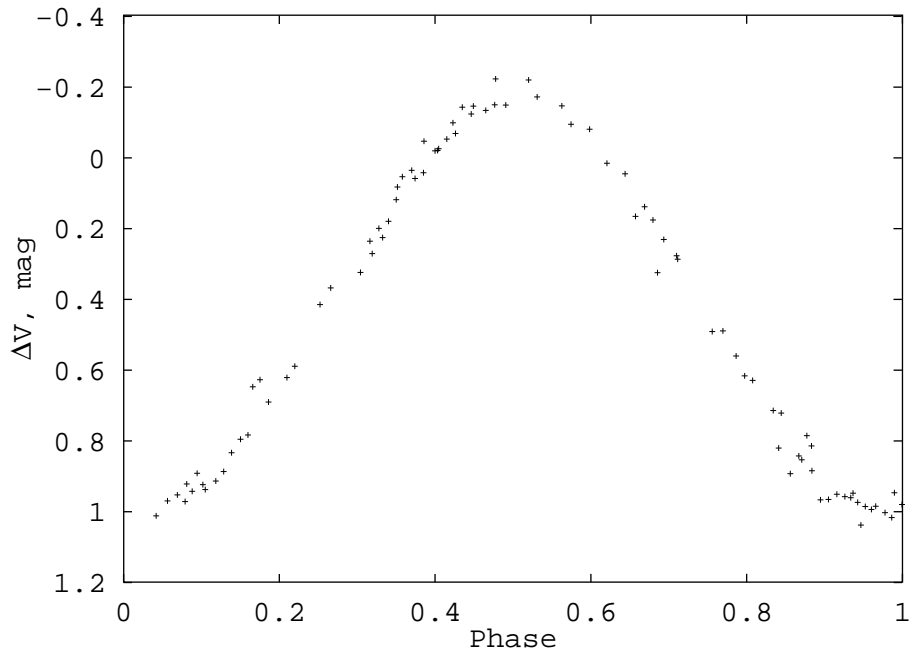


Figure 23. V664 Cas *V*-band observational light curve, Shugarov's data.

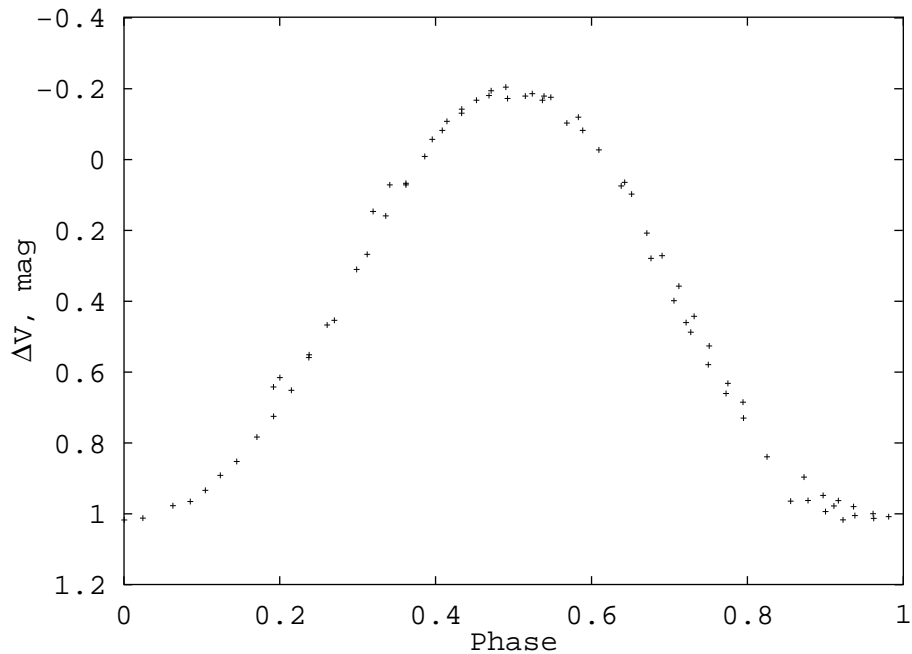


Figure 24. V664 Cas *V*-band observational light curve, Exter's data.

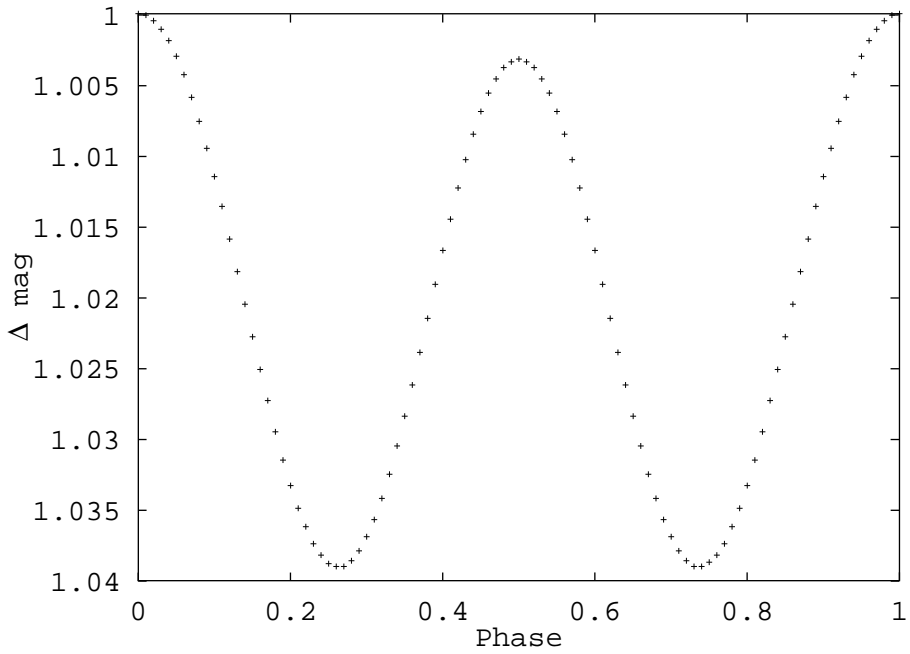


Figure 25. Tidal distortion in V664 Cas light curves.

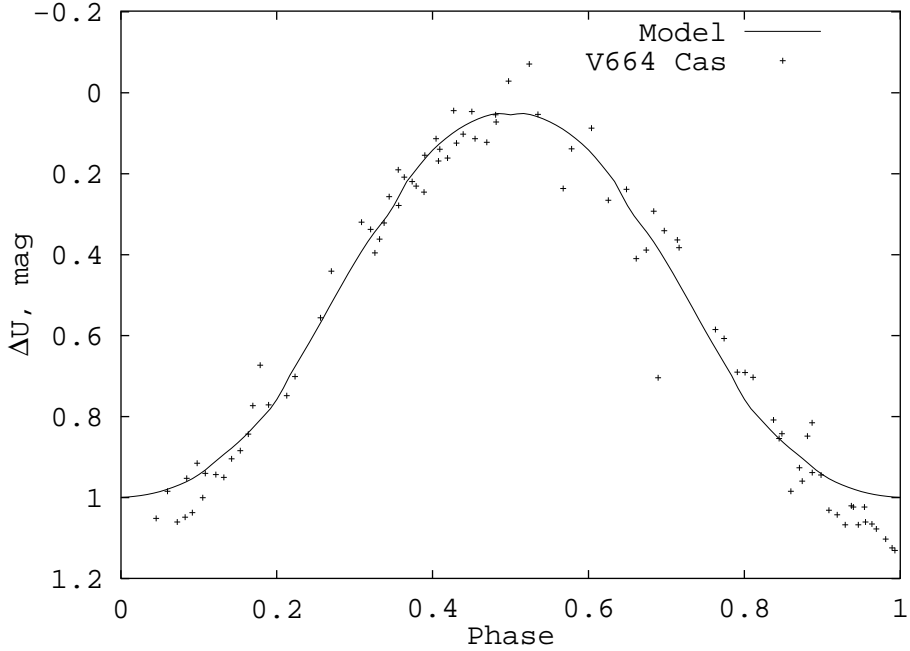


Figure 26. V664 Cas *U*-band light curve by Shugarov and the model. The model system parameters are: $T_1 = 86\,000$ K, $T_2 = 5000$ K, $R_{\text{sep}} = 3.25 R_{\odot}$, $R_1 = 0.074 R_{\odot}$, $R_2 = 1.23 R_{\odot}$, $i = 36^\circ$.

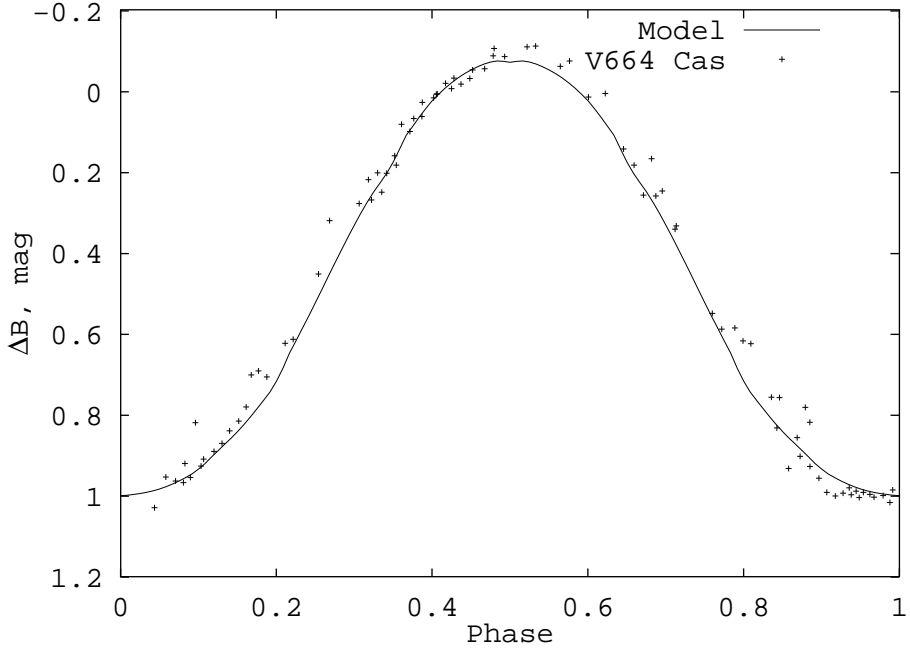


Figure 27. V664 Cas *B*-band light curve by Shugarov and the model. The model system parameters are: $T_1 = 86\,000$ K, $T_2 = 5000$ K, $R_{\text{sep}} = 3.25 R_\odot$, $R_1 = 0.074 R_\odot$, $R_2 = 1.23 R_\odot$, $i = 36^\circ$.

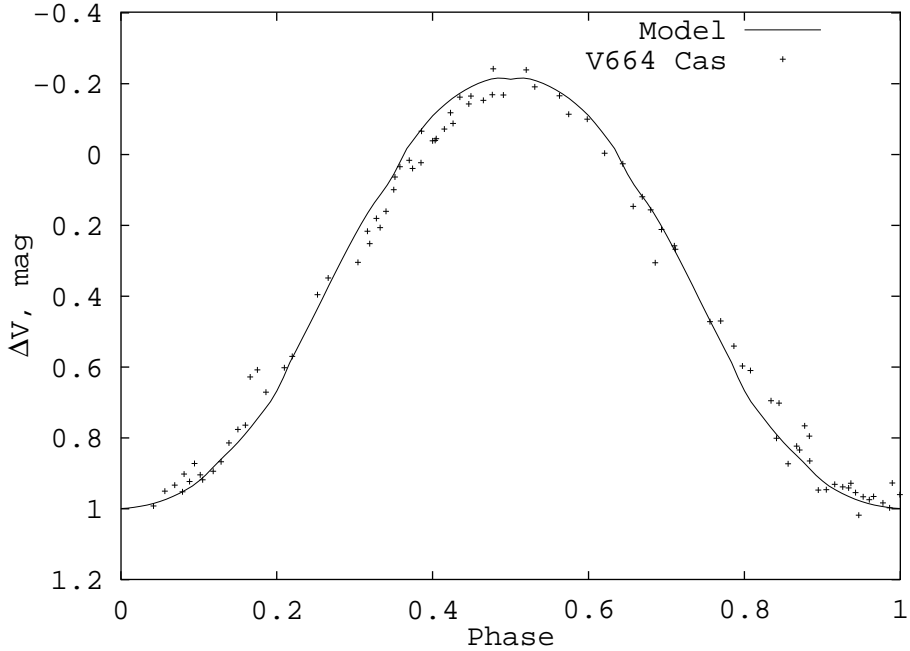


Figure 28. V664 Cas *V*-band light curve by Shugarov and the model. The model system parameters are: $T_1 = 86\,000$ K, $T_2 = 5000$ K, $R_{\text{sep}} = 3.25 R_\odot$, $R_1 = 0.074 R_\odot$, $R_2 = 1.23 R_\odot$, $i = 36^\circ$.

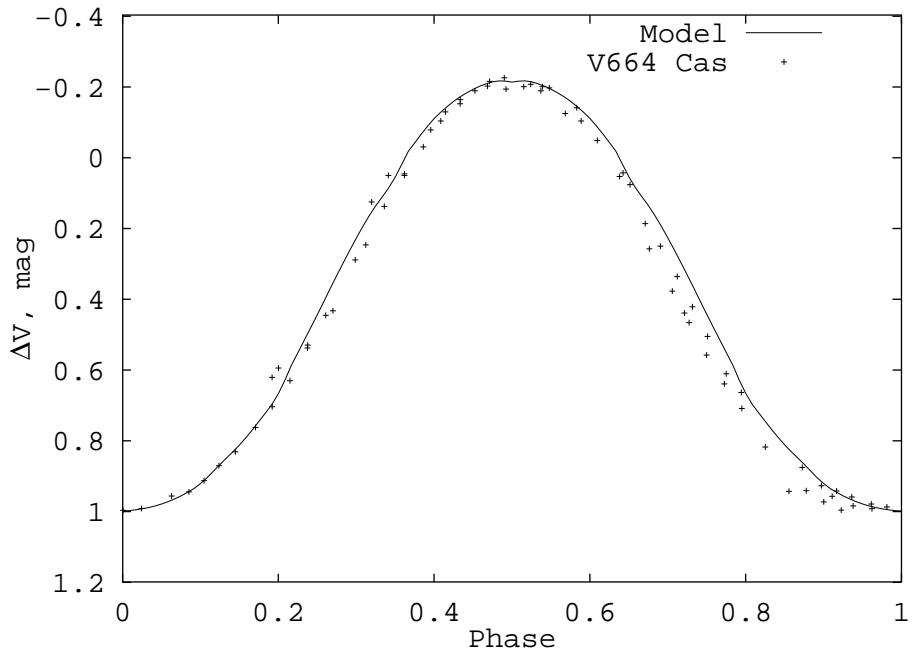


Figure 29. V664 Cas *V*-band light curve by Exter and the model. The model system parameters are: $T_1 = 86\,000$ K, $T_2 = 5000$ K, $R_{\text{sep}} = 3.25 R_\odot$, $R_1 = 0.074 R_\odot$, $R_2 = 1.23 R_\odot$, $i = 36^\circ$.

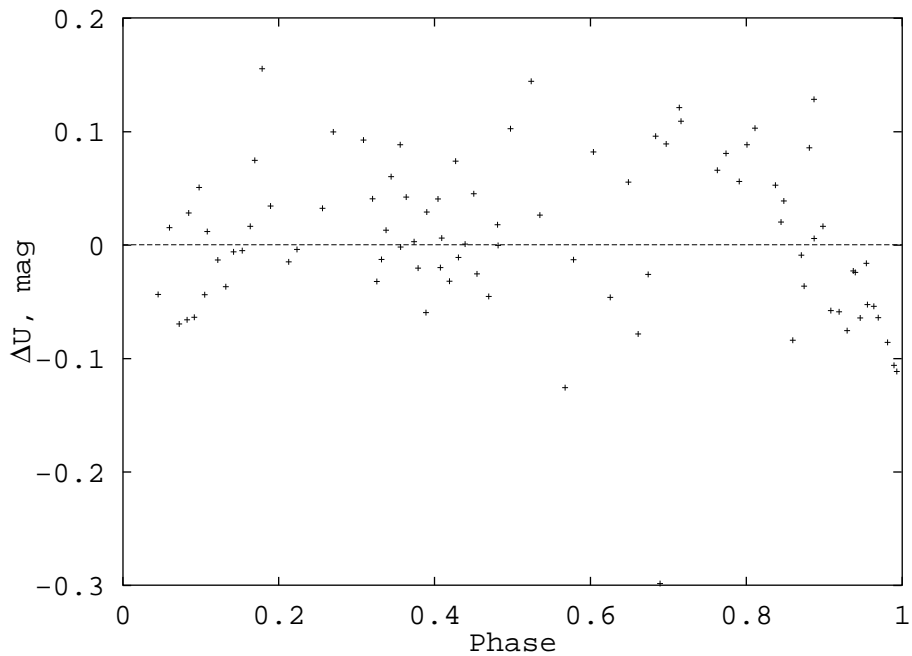


Figure 30. V664 Cas *U*-band residuals between the light curve by Shugarov and the model light curve.

B.6 Mass transfer stability in EHB progenitors

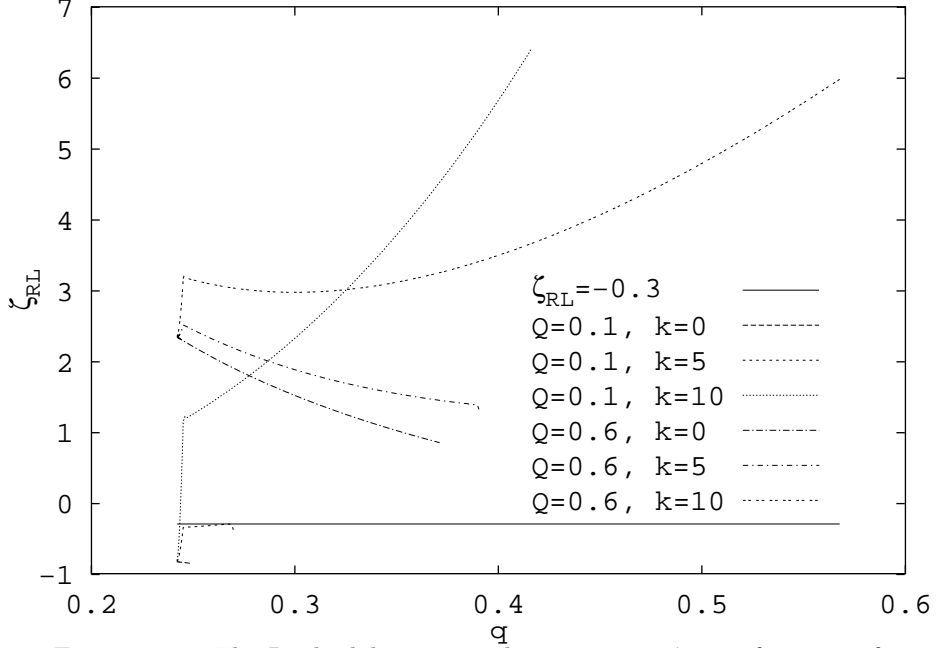


Figure 31. The Roche lobe mass-radius exponent ζ_{RL} as function of the mass ratio q , for different parameters k and Q . The initial system parameters are: $M_{1\text{init}} = 0.23 M_{\odot}$, $M_{2\text{init}} = 0.95 M_{\odot}$, $d_0 = 200 R_{\odot}$.

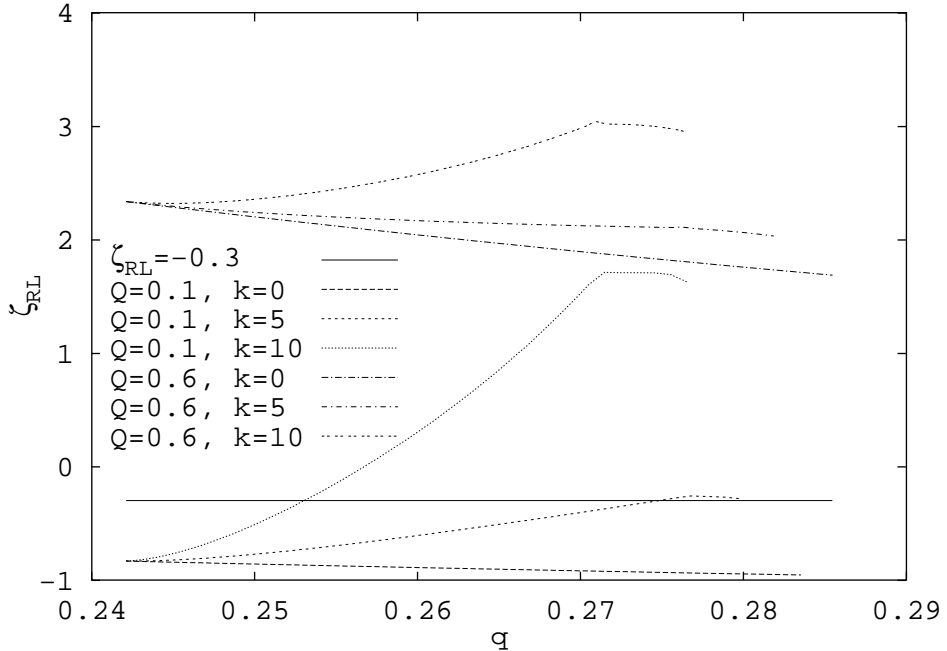


Figure 32. The Roche lobe mass-radius exponent ζ_{RL} as function of the mass ratio q , for different parameters k and Q . The initial system parameters are: $M_{1\text{init}} = 0.23 M_{\odot}$, $M_{2\text{init}} = 0.95 M_{\odot}$, $d_0 = 1000 R_{\odot}$.

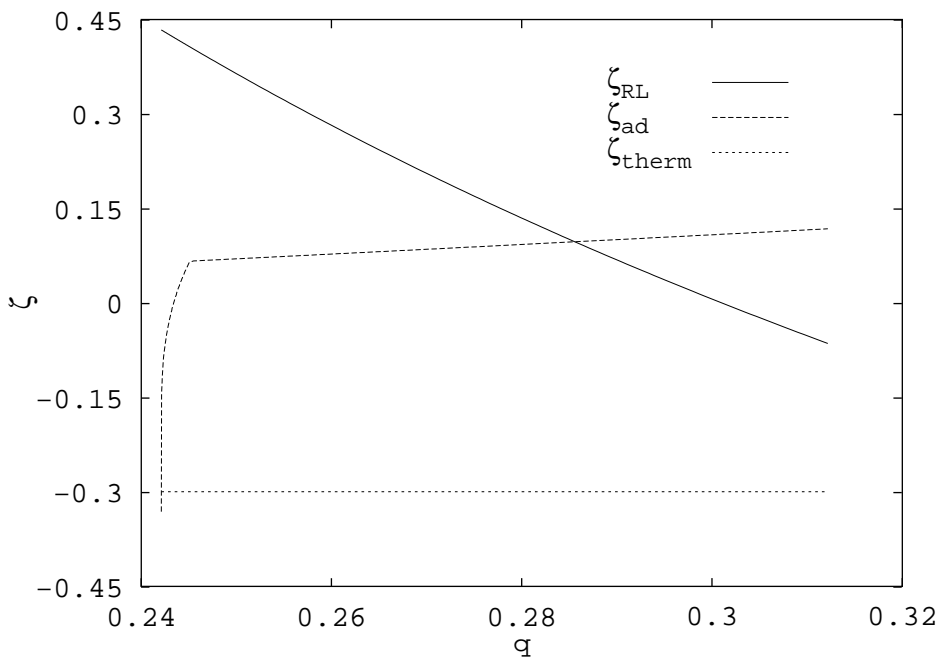


Figure 33. Mass-radius exponents as functions of the mass ratio q . The initial system parameters are: $M_{1\text{init}} = 0.23 M_{\odot}$, $M_{2\text{init}} = 0.95 M_{\odot}$, $d_0 = 200 R_{\odot}$, $k = 0$, $Q = 0.3$.

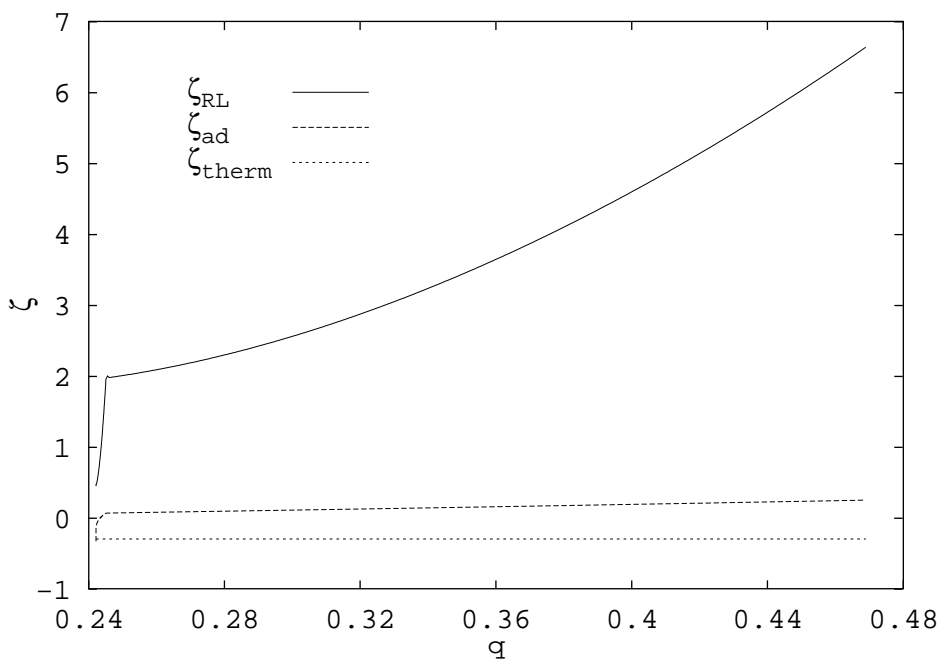


Figure 34. Mass-radius exponents as functions of the mass ratio q . The initial system parameters are: $M_{1\text{init}} = 0.23 M_{\odot}$, $M_{2\text{init}} = 0.95 M_{\odot}$, $d_0 = 200 R_{\odot}$, $k = 10$, $Q = 0.3$.

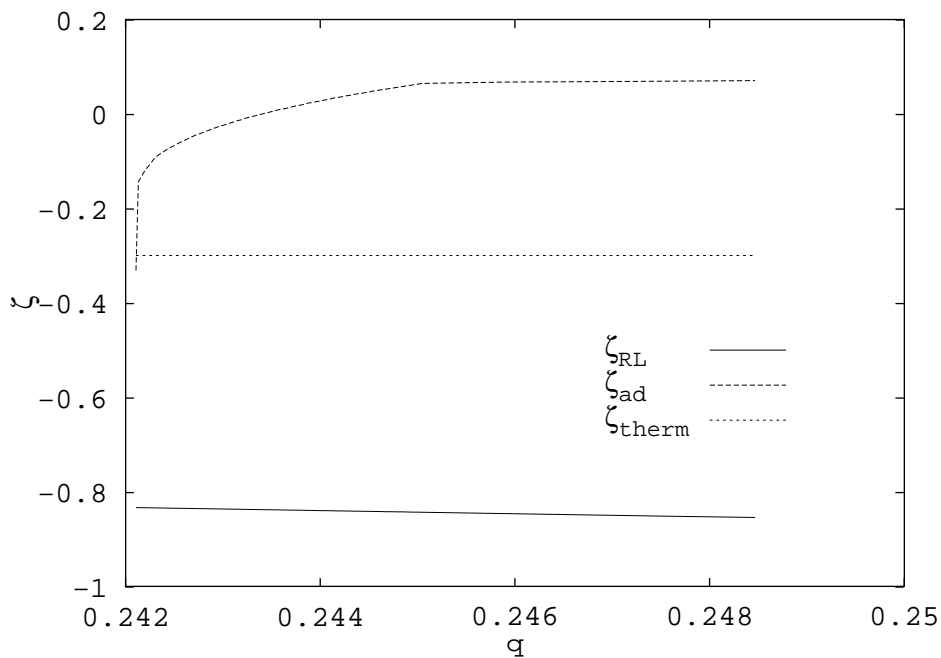


Figure 35. Mass-radius exponents as functions of the mass ratio q . The initial system parameters are: $M_{1\text{init}} = 0.23 M_{\odot}$, $M_{2\text{init}} = 0.95 M_{\odot}$, $d_0 = 200 R_{\odot}$, $k = 0$, $Q = 0.1$.

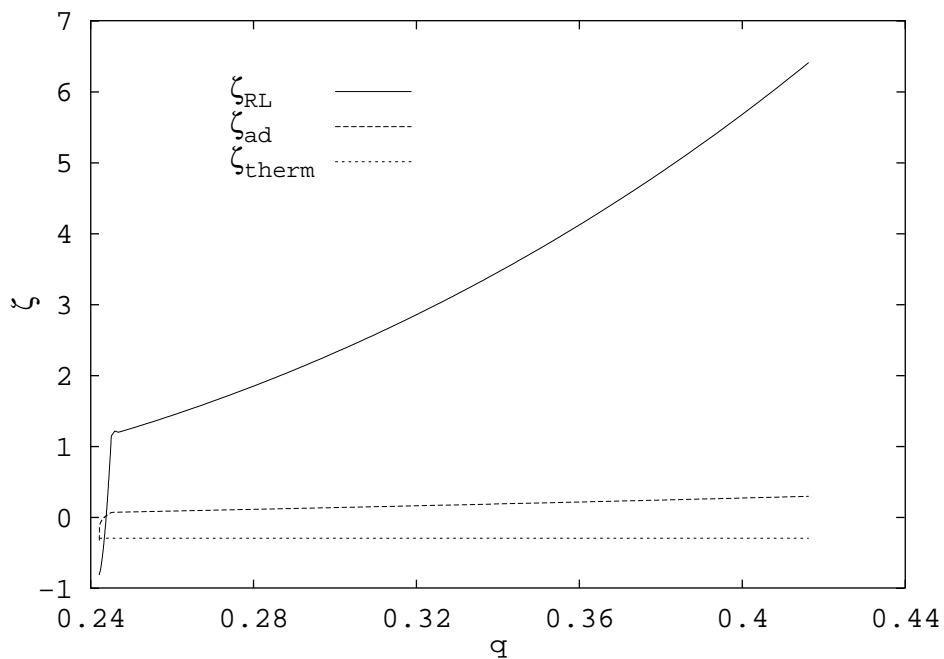


Figure 36. Mass-radius exponents as functions of the mass ratio q . The initial system parameters are: $M_{1\text{init}} = 0.23 M_{\odot}$, $M_{2\text{init}} = 0.95 M_{\odot}$, $d_0 = 200 R_{\odot}$, $k = 10$, $Q = 0.1$.

B.7 Evolution of EHB progenitors

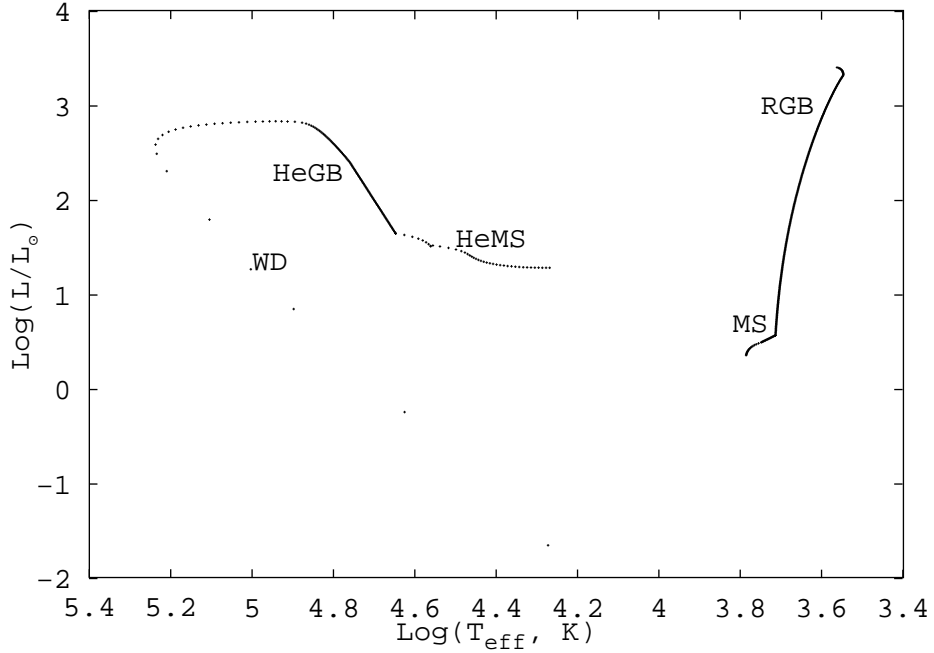


Figure 37. H-R diagram for a single star. $M_{1\text{init}} = 0.9 M_{\odot}$, metallicity $z = 0.004$ and the parameter of mass loss in Reimers formula $\eta = 0.85$, *i.e.* about twice of a standard value. MS stands for Main Sequence, RGB stands for Red Giant Branch, HeMS stands for Helium Main Sequence, HeGB stands for Helium Giant Branch, WD stands for White Dwarf.

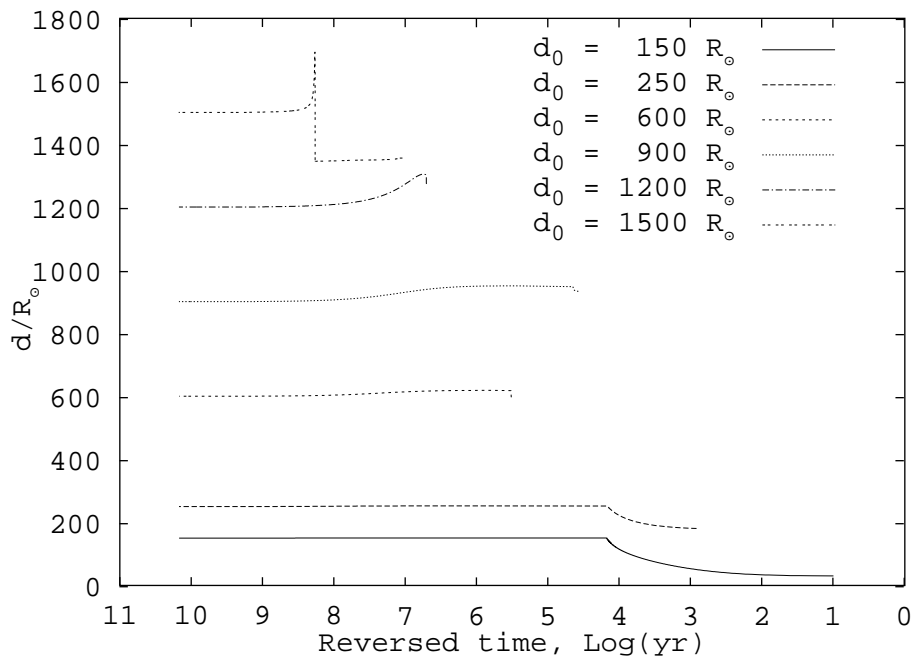


Figure 38. Separation d evolution for its different initial values d_0 . The initial mass of the accretor $M_{1\text{init}} = 0.23 M_\odot$, and that of the donor $M_{2\text{init}} = 0.95 M_\odot$, mass transfer parameters are $Q = 0.3$, $k = 6$. The time on the x-axis is counted backwards, so that the zero point is the final point of the model computation.

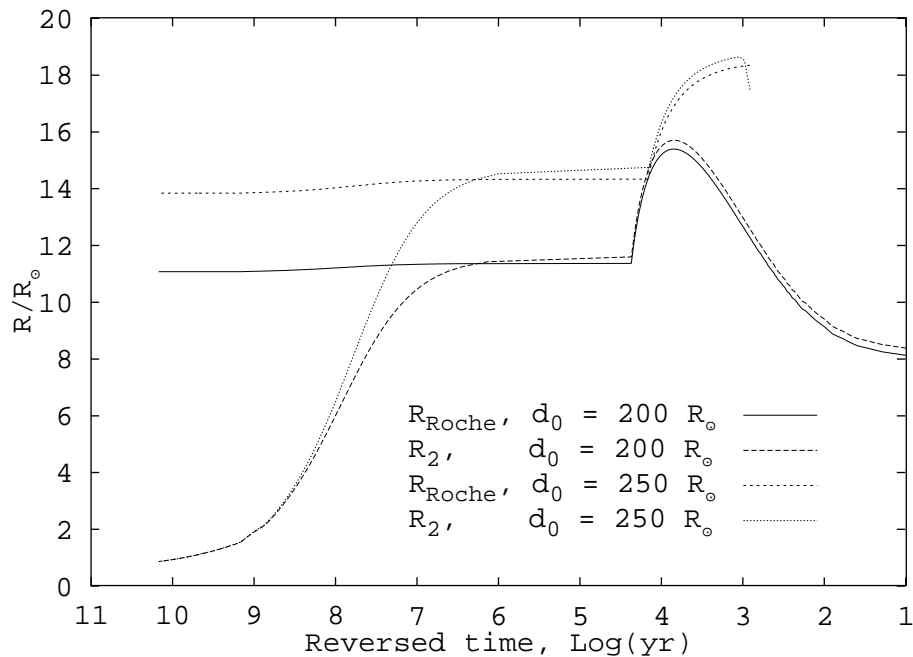


Figure 39. Roche lobe radius R_L and donor's radius R_2 evolution for different initial values of the separation d_0 . The initial system parameters are: $M_{1\text{init}} = 0.23 M_\odot$, $M_{2\text{init}} = 0.95 M_\odot$, $Q = 0.3$, $k = 6$.

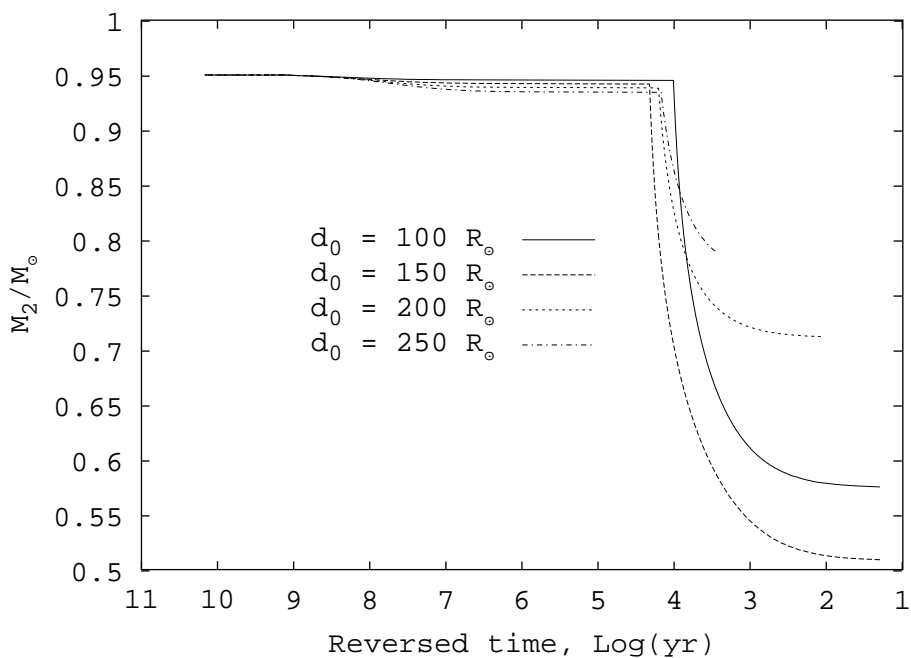


Figure 40. Donor's mass M_2 evolution for different initial values of the separation d_0 . The initial system parameters are: $M_{1\text{init}} = 0.23 M_\odot$, $M_{2\text{init}} = 0.95 M_\odot$, $k = 5$, $Q = 0.5$.

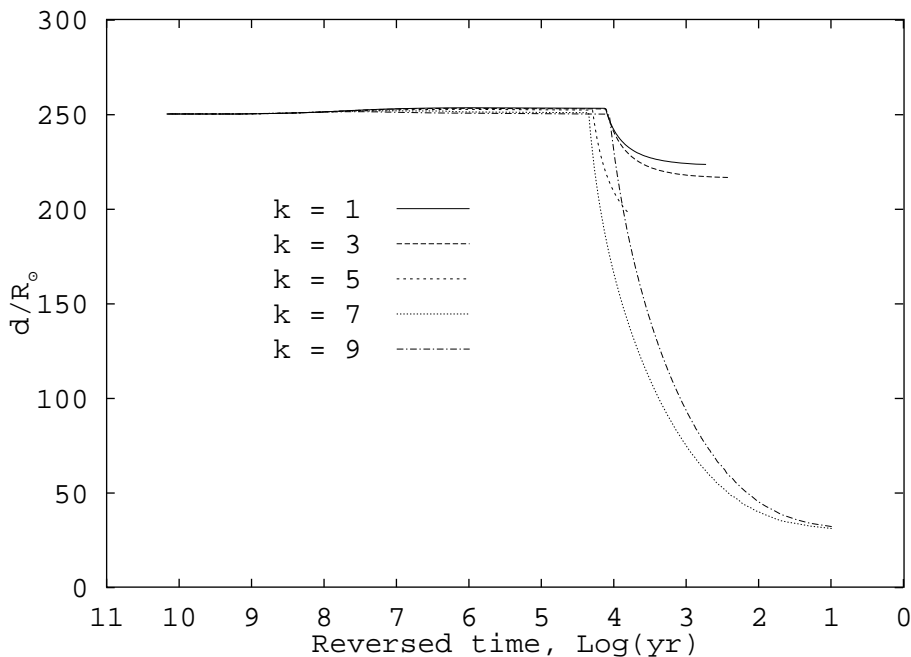


Figure 41. Separation d evolution for different values of the angular momentum loss parameter k . The initial system parameters are: $M_{1\text{init}} = 0.23 M_\odot$, $M_{2\text{init}} = 0.95 M_\odot$, $d = 250 R_\odot$, $Q = 0.3$.

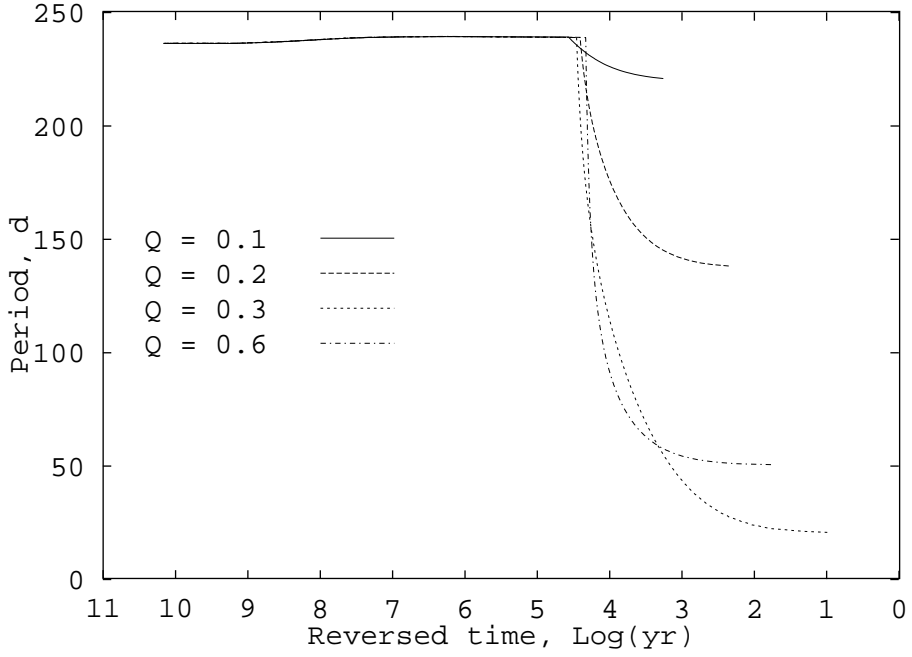


Figure 42. Period P evolution for different values of the mass transfer effectiveness parameter Q . The initial system parameters are: $M_{1\text{init}} = 0.23 M_{\odot}$, $M_{2\text{init}} = 0.95 M_{\odot}$, $d = 170 R_{\odot}$, $k = 5$.

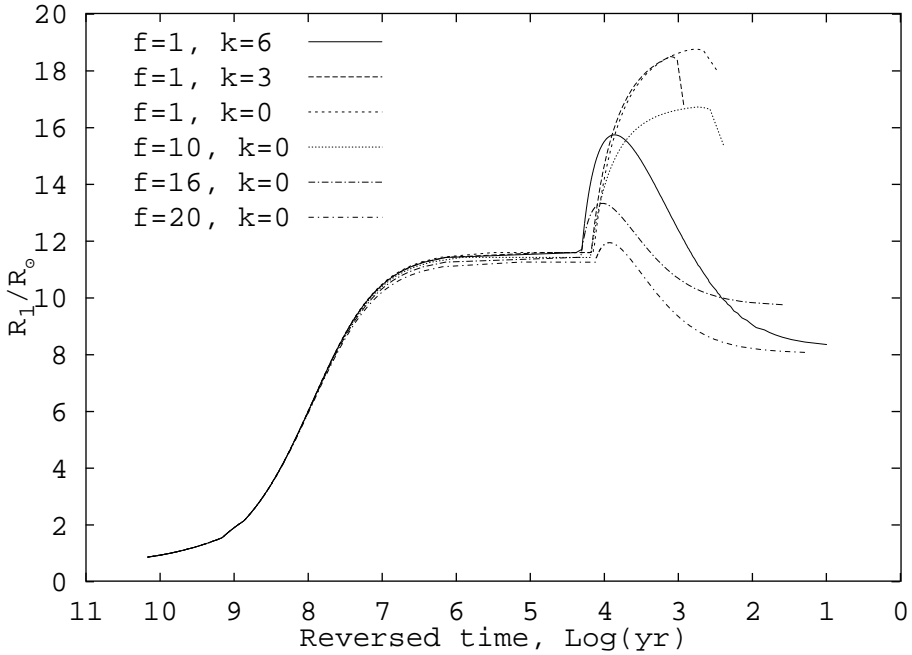


Figure 43. Donor's radius R_2 evolution for different momentum loss parameters k and f . The initial system parameters are: $M_{1\text{init}} = 0.23 M_{\odot}$, $M_{2\text{init}} = 0.95 M_{\odot}$, $d = 200 R_{\odot}$, $Q = 0.3$.

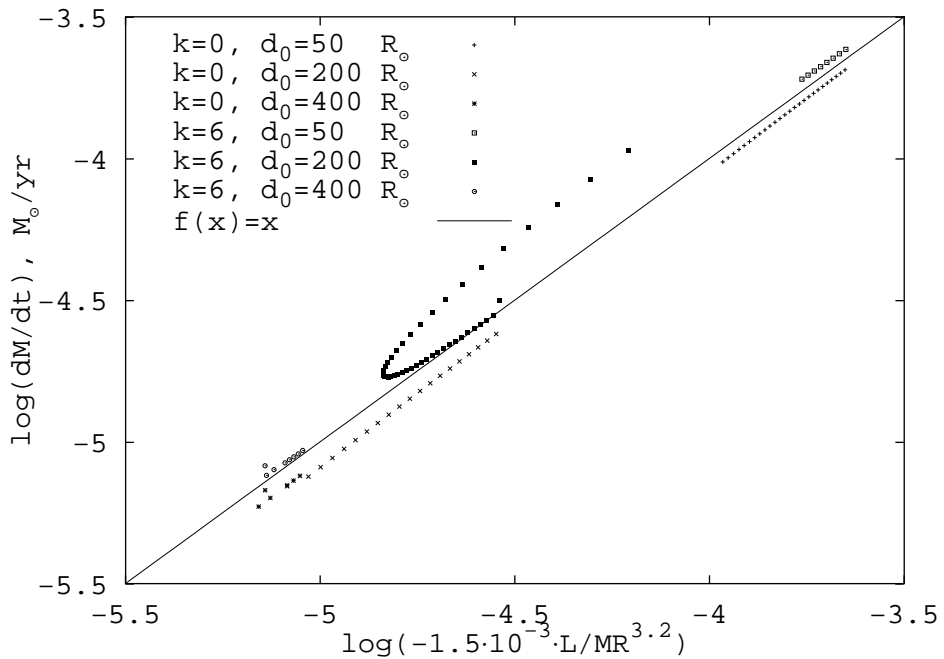


Figure 44. \dot{M} as function of $-1.5 \cdot 10^{-3} L/MR^{3.2}$ for different values of k and d_0 . Straight line $f(x) = x$ is superimposed to demonstrate the quality of the empirical formula. $M_{1\text{init}} = 0.23 M_\odot$, $M_{2\text{init}} = 0.95 M_\odot$, $Q = 0.3$

BIBLIOGRAPHY

- [1] A.Acker & Stenholm, *Astron & Astrophys.*, **233**, L21 (1990).
- [2] S.H.P.Alencar et al., *A&A*, **346**, 556 (1999).
- [3] L.X.Aller, "Astrofizika" (*in Russian*), (Moscow, "Izdatelstvo inostranoj literatury", 1955).
- [4] M.M. Basko & R.A. Sunyaev, *Ap&SS*, **21**, No.1 117 (1973).
- [5] H.E.Bond, R.Ciardullo, M.G.Meakes, "Evolutionary Processes in Interacting Binary Stars", eds. *Y. Kondo et al.*, 240 (1991).
- [6] H.E.Bond, *IAU Circ.* 3480 (1980).
- [7] H.E.Bond, *PASP*, **88**, 192 (1976).
- [8] H.E.Bond, W.Liller & J.E.Mannery, *ApJ*, **223**, 252 (1978).
- [9] A.M.Cherepashchuk, N.A.Katysheva, T.S.Khruzina & S.Yu.Shugarov, "Highly Evolved Close Binary Stars: Catalogue", *Gordon and Breach publishers*, (1996).
- [10] S.R.Cranmer, *MNRAS*, **263**, 989 (1993).
- [11] N.D'Cruz, D.Dorman, R.T.Rood & R.W.O'Connell, *A&A*, **466**, 359 (1996).
- [12] A.Eddington, *MNRAS*, **86**, 320, (1926).
- [13] P.P.Eggleton, *A&A*, **268**, 368, (1983).
- [14] K.M.Exter, D.L.Pollacco, P.F.L.Maxted, R.Napiwotzki & S.A.Bell, *MNRAS*, **359**, Issue 1, 315, (2005).
- [15] D.H.Ferguson & T.A.James, *ApJ*, **433**, 432 (1994).
- [16] L.Formiggini & E.M. Leibowitz, *A&A*, **227**, 121 (1990).
- [17] D.F.Gray, *In: Nablyudeniya i analiz zvezdnyh fotosfer (in Russian)* (Moscow, "Nauka", 1971).
- [18] A.D.Grauer, H.E.Bond, R.Ciardullo & T.A.Fleming, *In: AAS Meeting nr. 149*, 643 (Pasadena, 1987).
- [19] R.Haefner, A.Fiedler, K.Butler & H.Barwig, *A&A*, **428**, 181 (1994).
- [20] R.W.Hilditch, "Interacting binary stars", *The Observatory*, **114**, 212 (1994).

- [21] G.Hill, *Publ. Dom. Astrophys. Obs*, **15**, 297 (1979).
- [22] U.Heber, *A&A*, **155**, 33 (1986).
- [23] J.H.Heckathorn & R.A.Fessen, *A&A*, **143**, 475 (1985).
- [24] M.S.Hjellming & R.F.Webbink, *Astrophysical Journal*, **318**, 794 (1987).
- [25] C.Hoffmeister, G.Richter & W.Wenzel, *In: "Veranderliche Sterne"* (Johann Ambrosius Barth, Leipzig, 1990, russian translation "Nauka", Fizmatlit, 1990).
- [26] D.Hoffleit *Harvard Bull.*, No. 887 (1932).
- [27] I.Hubeny et al., *Astrophysical Journal*, **594**, 1011 (2003).
- [28] J.R.Hurley, O.P.Pols & C.A.Tout, *MNRAS*, **315**, 543 (2000).
- [29] D.G.Hummer & M.J.Seaton, *MNRAS*, **125**, 437 (1963).
- [30] I.Jr.Iben & M.Livio, *PASP*, vol. 105, **694**, 1373 (1993).
- [31] I.Jr.Iben & A.V.Tutukov, *Astrophysical Journal*, **418**, 343 (1993).
- [32] D.Kilkenny, C.Koen, D.ODonoghue & R.S.Stobie, *MNRAS*, **285**, 640 (1997).
- [33] J.Kubát, *In: White Dwarfs, eds. J. Isern, M. Hernandez & E. Garcia-Berro*, **214**, 229 (1997).
- [34] J.Kubát, J.Puls & A.W.A.Pauldrach, *A&A*, **341**, 587, (1999).
- [35] J.Kubát, *In: The Be Phenomenon in Early-Type Stars, IAU Coll. 175, eds. M.A.Smith, H.F.Henrichs & Fabregat J., ASP Conference Series*, **214**, 705, (2000).
- [36] K.R.Lang, "Astrophysical Formulae. A. Compendium for the Physicist and Astrophysicist" (Springer-Verlag, Berlin, Heidelberg, New York, 1974).
- [37] D.Y.Martynov, "Zatmennye peremennye zvezdy" (in Russian), 122, (OGIZ, 1939).
- [38] P.F.L.Maxted, T.R.Marsh, C.Moran, V.S.Dhillon & R.W.Hildtich, *In: 11th European Workshop on WD, ASP Conference series*, **169**, 301, (1999).

- [39] P.F.Maxted, U.Heber, T.R.Marsh, & R.C.North, *MNRAS*, **326**, 1391, (2001).
- [40] F.Meyer & E.Meyer-Hoffmeister, *A&A*, **121**, 29 (1983).
- [41] D.Mihalas, *In: Stellar Atmospheres, W.H. Freeman and Company*, (1978).
- [42] E.A.Milne, *In: "Handbuch der Astrophysik", vol. 3*, 1 (1930).
- [43] E.A.Milne, *MNRAS*, **87**, 43, (1927).
- [44] I.N.Minin, *Astrofizika (in Russian)*, **1**, 275, (1965).
- [45] L.Morales-Rueda, P.F.L.Maxted, T.R.Marsh, R.C.North & U.Heber, *MNRAS*, **338**, 752, (2003).
- [46] W.McD.Napier, *Ap&SS*, **2**, 61 (1968).
- [47] D.E.Osterbrock, *Astrophysics of Gaseous Nebulae*, (eds. G.Burbidge & M. Burbidge, 1974), 11–57.
- [48] B.Paczynski & D.S.Dearborn, *MNRAS*, **190**, 395 (1980).
- [49] D.L.Pollacco & S.A.Bell *MNRAS*, **262**, no. 2, 377 (1993).
- [50] D.L.Pollacco & S.A.Bell *MNRAS*, **267**, no. 2, 452 (1994).
- [51] I.Pustynnik, *Astrofizika (in Russian)*, **3**, 69 (1964).
- [52] I.B.Pustynnik, *In "Dvoynye zvezdy" (in Russian)*, 206 (Moscow, Kosmoinform, 1964).
- [53] I.Pustynnik & V.-V.Pustynski, *Odessa Astron. Publ.*, **9**, 45 (1996).
- [54] I.Pustynnik & V.-V.Pustynski, *In: Planetary Nebulae, Proceed. of the 180th Symp. of the IAU, eds. H.J.Habing, H.J.G.L.M.Lamers*, 131 (1997).
- [55] I.Pustynnik & V.-V.Pustynski, *In: Thermal and Ionization Aspects of Flows from Hot Stars: Observations and Theory, Tartu*, 381 (2000).
- [56] I.Pustynnik & V.-V.Pustynski, *In: 11th European Workshop on White Dwarfs, PASP Conference series*, **169**, 289 (1999).
- [57] I.Pustynnik, V.-V.Pustynski, J.Kubat, *Odessa Astron. Publ.*, **14**, 87 (2001).
- [58] V.-V.Pustynski & I.Pustynnik, *In: 12th European Workshop on White Dwarfs, PASP Conference series*, **226**, 253 (2001).

- [59] V.-V.Pustynski & I.Pustylnik, *Baltic Astronomy*, vol 13, no 1, **226**, 253 (2004).
- [60] V.-V.Pustynski & I.Pustylnik, *Acta Astronomica*, **56**, 83 (2006).
- [61] M.D.Reed, S.D.Kawaler & S.J.Kleinman, *In: 12th European Workshop on White Dwarfs, PASP Conference series*, **226**, 181 (2001).
- [62] H.Ritter, *A&A*, **169**, 139 (1986).
- [63] H.Ritter, *MNRAS*, **309**, 360 (1999).
- [64] H.Ritter & U.Kolb, *Astron. & Astrophys.*, **404**, 301 (2003).
- [65] S.M.Ruciński, *Acta Astronomica*, **23**, 4, 301 (1973).
- [66] R.A.Saffer, P.Bergeron, D.Koester, & J.Liebert, *ApJ*, **432**, 351 (1994).
- [67] N.A.Sahibullin & V.V.Shimansky *Astron. Zhurnal*, **73**, 1 (1996).
- [68] M.J.Sarna & J.-P.De Greve, *Quarterly Journal of the Royal Astronomical Society*, **37**, 11 (1996).
- [69] G.E.Soberman, E.S.Phinney & E.P.J.van den Heuvel, *Astronomy & Astrophysics*, **327**, 620 (1997).
- [70] S.Sobieski, *Astrophys. J. Suppl.*, **12**, 109, 263 (1965).
- [71] V.V.Shimanskii, N.V.Borisov, N.A.Sakhibullin & A.E.Surkov, *Astronomy Reports*, vol. **48**, Issue 7, 563 (2004).
- [72] C.A.Tout & D.S.Hall, *MNRAS*, **253**, 9, (1991).
- [73] N.A.Walton, J.R.Walsh & S.R.Pottash, *Preprint*, (London, University College, 1992).
- [74] R.A.Weid & M.J.Word, *In: "Vzaimodejstvujushchie zvezdy"* (in Russian, (Moskva, "Nauka", 1993).

KOKKUVÕTE

Peegeldusefekti modelleerimine kataklüsmieelsel evolutsioonietapil asuvates lähiskaksiksüsteemides

Kataklüsmieelsel evolutsioonietapil asuvad lähiskaksiksüsteemid (Precataclysmic Binary Systems ehk PCB-d) on 1980-ndatel aastatel klassifitseeritud kaksiktähtede liik, mis vastab järgnevatele kriteeriumitele: 1) peakomponent on valge kääbustäht või selle eellane; 2) kaaslane on peajada väikese massiga täht, s.o. punane kääbus; 3) orbitaalperiood on lühike, tavaliselt $P_{\text{orb}} < 2^{\text{d}}.4$; 4) süsteem asub planetaarse udukogu tsentraalses osas.

Kuna PCB-de orbiitide poolteljed on lühikesed ja peakomponendi efektiivne temperatuur on väga kõrge, siis kaaslase see poolkera, mis on pööratud valge kääbustähe poole, on valgustatud kuuma peatähe poolt saabuva tugeva kiirgusvooga. Tunduv osa sellest on UV või isegi pehme röntgenkiirgus. See voog kutsub esile väga tugeva peegeldusefekti. Peegeldusefektiga kaasnev heleduse kasv PCB-des võib ületada ühte tähesuure.

Käesoleva väitekirja põhiülesandeks oli välja selgitada peatähelt pealangevast kiirgusvoost tingitud füüsikaliste protsesside iseärasusi külma kaaslastähe atmosfääris ning selgitada peegeldusefekti detailsemalt, võimaldamaks täpsemalt modelleerida vaadeldud PCB-de heleduskõveraid ning määrata nende objektide füüsikalisi omadusi.

Sellel eesmärgil on välja töötatud väljastpoolt valgustatud tähe atmosfääri kahekihiline mudel. On koostatud vastav tarkvara ja sellega teostatud mudelarvutused. Meie mudeli originaalsus seisneb selles, et ülemises atmosfäärikihis pole eeldatud lokaalse termodünaamilise tasakaalu kehtivust. Eelduste kohaselt, ülemine kiht on läbipaistev optilisele kiirgusele, kuid neelab efektiivselt kiirgust Lyman'i kontiinumis. Atmosfääri ülakihi modelleerimiseks lahendatakse tasakaaluvõrrandite süsteem (hüdrostaatilise, ionisatsioonilise ja termilise tasakaalu võrrandid). Jahutusmehhanismina on arvestatud elektronide rekombinatsioone vesinikuioonidega. Alumise atmosfäärikihi modelleerimiseks on kasutatud difusioonilähendust.

Kirjeldatud meetodil on koostatud kaaslastähe atmosfääri mudel erinevatel kaugustel tähtsentreid ühendavast teljest. Peatähe kiirgus, läbides kaaslase atmosfääri, osaliselt neeldub ülemises kihis (Lyman'i kontiinum), osaliselt aga siseneb alumisse kihti (optiline kiirgus). Ülakihis neeldunud kvantid kuumendavad atmosfääri, mis emiteerib peamiselt optilist kiirgust. See kiirgus osaliselt lahkub atmosfäärist, osaliselt aga neeldub alumises kihis. Modelleerimisega saadakse tähepinnalt väljuva kiirguse intensiivsuse valitud punkti asukohta ning suuna funktsioonina. Jagades valgustatud tähepinna kontsentrilisteks ringtsoonideks ümber valgustatud ala keskpunkti, konstrueerime eespool kirjeldatud atmosfäärimudeli igas tsoo-

nis ning leiame vaadeldava süsteemi heleduse, integreerides väljuvat kiirgust üle nende tsoonide ning lisades sellele peatähe ja kaaslastähe varjutamata alade kiirguspanuse. Korrates seda protseduuri erinevate orbitaalsete faasinurkade korral, saamegi süsteemi heleduskõvera.

Mudelarvutustest selgus, et valgustatud atmosfääri ülemises kihis puudub soojuslik stabiilsus. Märgatav osa pealelangeva kiirguse energiast kulub elektrongaasi kuumenemiseks, samuti mittestatsionaarsete protsesside esilekutsumiseks (näiteks, pulsatsioonideks), mille ajaskaala on võrreldav süsteemi orbitaalperioodiga. Selles kihis võib ka esineda temperatuuri inversioon. Üheks selle efekti tagajärjeks on äärelehelenemine, mis asendab mittevalgustatud või nõrgalt valgustatud atmosfäärides esinevat ääreletumenemist.

Kirjeldatud mudelit kasutasime kolme lähiskaksisüsteemide heleduskõvera modelleerimiseks, nimelt UU Sge, V477 Lyr ja V664 Cas. Kahe esimese süsteemi puhul arvutasime heleduskõverad V -värvis, V664 Cas puhul aga UBV -heleduskõverad. Sellise modelleerimise tulemusena osutus võimalikuks kitsendada neid süsteeme iseloomustavate füüsikaliste parameetrite võimalikke arväärtuste vahemikku, sealhulgas peakomponendi temperatuuri ning kaaslaste raadiust.

Töö käigus on ka uuritud massi väljavoolu mõju algselt laia kaksiksüsteemi orbitaalevolutsioonile. Kui üks süsteemi komponentidest täidab oma kriitilise Roche'i õõnsuse, algab massi ülevool teisele komponendile, kusjuures osaliselt mass lahkub süsteemist tähetuulena, viies kaasa ka orbitaalset impulssmomenti. Kui orbitaalse impulssmomenti kadu on piisavalt efektiivne, siis selline protsess põhjustab orbiidi pooltelje ja orbitaalperioodi lühenemist. On uuritud kaksiktähe orbiidi pooltelje evolutsiooni juhul, kui doonortähe mass osaliselt lahkub süsteemist, läbides korotatsiooni staadiumi Alfvén'i raadiuse kaugusel. Doonortähe raadiuse muutus on arvestatud massikao tagasimõjuna sellele.

On leitud, et orbitaalevolutsioon ja selle lõpptulemus sõltuvad oluliselt pooltelje algsest pikkusest, ning massi ülekande ja orbitaalse impulssmomenti kao efektiivsusest. Soodsatel tingimustel võib doonortäht jõuda kaotada suure osa oma massist ning orbitaalsest impulssmomentist, mis viib lühiperioodilise süsteemi moodustumisele algselt pikaperioodilisest süsteemist. Sellise süsteemi lõppparameetrid võivad osutada sarnasteks EHB (Extreme Horizontal Branch) objektide parameetritele. Kui aga algse süsteemi parameetrite poolt määratud tingimused pole nii soodsad, võib doonortäht kokku tõmbuda alla oma Roche'i piiri enne kui märgatav osa tema massist ja orbitaalsest impulssmomentist on kaotatud, mistõttu orbiidi pooltelg ning periood muutuvad vaid vähe. Erinevates tingimustes massikadu võib viia väga erinevate perioodidega kaksiksüsteemide, kaasa arvatud lühiperioodiliste süsteemide, moodustumisele. See tulemus võib

selgitada, miks vaadeldavate kaksik-EHB süsteemide perioodid on vägagi erinevad.

Massiülekanega kaasnevate protsesside uurimine näitas, et need protsessid tavaliselt ei rahulda stabiilsuse tingimust, eriti juhul, kui nad viivad lühiperioodilise kaksiksüsteemi moodustumisele. Kuna aga nende protsesside ajaskaala on väga lühike, $\sim 10^4$ aastat, siis nad jõuavad põhjustada orbiidi olulist lühenemist.

Massikao tempo leidmiseks on pakutud ka empiiriline valem, mis esitab massikao doonortähe heleduse, massi ning raadiuse astmefunktsioonide korrutisena.

CURRICULUM VITAE

1. Curriculum Vitae

Name: Vladislav-Veniamin Pustynski

Date and place of birth: 18 March 1975

Citizenship: Estonian

Address: Tartu Observatory, Tõravere, 61602,
Estonia

Phone: (+372) 55 40 302

e-mail: vladislav@aai.ee

Position: Tartu Observatory, research associate;
Tallinn Technical University, research
associate

Education:

1998–2006	Tartu University, Ph.D. student
1996–1996	Tartu University, M.Sc. student
1992–1996	Tartu University, B.Sc. student

Languages:

Estonian	Upper Intermediate
Russian	Mother tongue
English	Upper Intermediate, technical translator certificate
Spanish	Advanced

Career:

2002–	Tallinn Technical University
1998–	Tartu Observatory

Research work:

Tartu University, B.Sc. degree *cum laude*
(astrophysics, 1996), scientific supervisor
Izold Pustynnik

Tartu University, M.Sc. degree
(astrophysics, 1998), scientific supervisor
Izold Pustynnik

Prizes:

1997, Ernst Öpik prize from Tartu Observatory
1996, Prize from Estonian Academy of Science
for B.Sc. thesis

Main research fields:

Astrophysics, close binary systems, reflection
effect

2. Curriculum Vitae in Estonian

Elulugu

Nimi: Vladislav-Veniamin Pustõnski

Sünniaeg ja koht: 18. märts 1975. a.

Kodakondsus: eesti

Aadress: Tartu Observatoorium, Tõravere, 61602, Eesti

Telefon: (+372) 55 40 302

e-mail: vladislav@aai.ee

Töökoht: Tartu Observatoorium, teadur;
Tallinna Tehnikaülikool, teadur

Hariduskäik:

1998–2006 Tartu Ülikool, Ph.D. üliõpilane

1996–1996 Tartu Ülikool, M.Sc. üliõpilane

1992–1996 Tartu Ülikool, B.Sc. üliõpilane

Keelteoskus:

Eesti kõrgem kesktase

Vene emakeel

Inglise kõrgem kesktase, tehnilise tõlgi kutsetunnistus

Hispaania madalam kõrgtase

Teenistuskäik:

2002– Tallinna Tehnikaülikool

1998– Tartu Observatoorium

Teadustegevus:

Tartu Ülikool, B.Sc. kraad *cum laude*
(astrofüüsika, 1996), teaduslik juhendaja
Izold Pustynnik

Tartu Ülikool, M.Sc. kraad
(astrofüüsika, 1998), teaduslik juhendaja
Izold Pustynnik

Preemiad:

1997, Ernst Öpiku preemia Tartu
Observatooriumist

1996, Preemia Eesti Teadusakadeemialt
B.Sc. diplomitöö eest

Põhilised uurimissuunad:

Astrofüüsika, lähiskaksiksüsteemid,
peegeldusefekt

ACKNOWLEDGEMENTS

I would like to express my gratitude to all those who gave me the possibility to complete this thesis.

First and foremost I would like to thank my supervisor Dr. Izold Pustyl'nik from Tartu Observatory who prompted me to this research and helped me in all its stages, and whose assistance contributed significantly to my formation as astrophysicist.

I express my deepest gratitude to many people who have helped to improve this research by their advices and discussions, especially Arved Sapar and Indrek Kolka (Tartu Observatory), Vladislav Shimansky (Kazan University) and many others.

I am thankful to Prof. Anatoli Cherepashchuk (GAISH, Moscow) for constructive criticism, fruitful scientific discussions and his kind consent to take the responsibilities of the official opponent of my Thesis.

I am deeply indebted to Dr. Jiří Kubát and his colleagues from Ondřejov Observatory, Czech Republic, for their hospitality. During my stay in Ondřejov an important part of this work was done.

I would also like to thank Dr. Don Pollacco and Dr. Katrina Exter from Queen's University, Belfast, as well as Dr. Sergei Shugarov, GAISH, Moscow for providing observational data.

I owe my deepest thanks to my family, whose countenance I have been feeling all these years.

I acknowledge the financial support from the Estonian Science Foundation (Grant 5760).

DISSERTATIONES ASTRONOMIAE UNIVERSITATIS TARTUENSIS

1. **Tõnu Viik.** Numerical realizations of analytical methods in theory of radiative transfer. Tartu, 1991.
2. **Enn Saar.** Geometry of the large scale structure of the Universe. Tartu, 1991.
3. **Maret Einasto.** Morphological and luminosity segregation of galaxies. Tartu, 1991.
4. **Urmas Haud.** Dark Matter in galaxies. Tartu, 1991.
5. **Eugene A. Ustinov.** Inverse problems of radiative transfer in sounding of planetary atmospheres. Tartu, 1992.
6. **Peeter Tenjes.** Models of regular galaxies. Tartu, 1993.
7. **Ivar Suisalu.** Simulation of the evolution of large scale structure elements with adaptive multigrid method. Tartu, 1995.
8. **Teimuraz Shvelidze.** Automated quantitative spectral classification of stars by means of objective prism spectra: the method and applications. Tartu, 1999.
9. **Jelena Gerškevič.** Formation and evolution of binary systems with compact objects. Tartu, 2002.
10. **Ivan Suhhonenko.** Large-scale motions in the universe. Tartu, 2003.
11. **Antti Tamm.** Structure of distant disk galaxies. Tartu, 2006.